UNIVERSITAT DE BARCELONA

Subsynoptic characterization of tropopause fold structures with global data analyses and mesoscale WRF simulations

Mireia Mateu i Santaeulària

Subsynoptic characterization of tropopause fold structures with global data analyses and mesoscale WRF simulations

Mireia Mateu i Santaeulària

Ph.D. program in Physics

Supervisors:

Dr. Ángel Redaño Xipell
Dr. Bernal Codina Sánchez

UNIVERSITAT DE BARCELONA
Departament d'Astronomia i Meteorologia
Universitat de Barcelona

November 2015

Resum

En aquesta tesi s'ha realitzat una anàlisi i una caracterització detallada sobre les estructures de plegament de la tropopausa (*Tropopause Foldings* en la literatura anglesa) utilitzant, per un costat, un any de dades globals de relativa alta resolució (0.3 graus) d'anàlisis del model GFS (*Global Forescating System*), i per l'altra, 10 anys de dades de simulacions numèriques diàries realitzades amb el model de mesoescala WRF (*Weather Research and Forecasting*) amb una resolució aproximada d'uns 30 km i inicialitzades amb les dades JRA-25 (*Japanese 25-year ReAnalysis*) que tenen una resolució grollera d'1.125 graus.

La tropopausa és una capa fina de l'atmosfera que separa la troposfera de l'estratosfera, dues capes molt diferents en la seva estructura tèrmica, condicions dinàmiques i composició química. A la troposfera, per exemple, la temperatura disminueix amb l'altitud, els moviments verticals i la barreja hi són relativament freqüents, i l'aire pot contenir grans quantitats de vapor d'aigua mentre que l'ozó n'és generalment escàs. En canvi, a l'estratosfera la temperatura augmenta amb l'altitud, els moviments són bàsicament horitzontals, i l'aire està estratificat per capes, pobres en vapor d'aigua i relativament riques en concentració d'ozó, provinent de la capa d'ozó que es troba precisament en els primers 25 km de l'estratosfera. Per tant, la tropopausa representa una zona de transició i canvis abruptes entre aquestes dues capes, cosa que fa que jugui un paper molt important en l'intercanvi de substàncies i que presenti una gran sensibilitat a possibles canvis atmosfèrics.

Tenint en compte les característiques dinàmiques, es pot definir la tropopausa com una superfície de valor constant de vorticitat potencial, típicament la superfície de 2 PVU (unitats de vorticitat potencial, on 1 PVU = $10^{-6} m^2 s^{-1} K kg^{-1}$). D'aquesta manera l'aire troposfèric queda definit per valors baixos de vorticitat potencial (PV < 2) i l'estratosfèric per valors alts (PV > 2). Sota condicions de conservació adiabàtiques i sense fricció, aquesta tropopausa dinàmica actua com a una barrera física entre les dues capes. Deformacions importants d'aquesta superfície, com per exemple els plegaments de tropopausa, poden tenir una gran influència en el desenvolupament de fenòmens meteorològics a la troposfera i poden ser un dels

mecanismes més importants d'intercanvi i transport de substàncies entre la troposfera i l'estratosfera als extratròpics. Aquests plegaments de tropopausa o intrusions estratosfèriques es caracteritzen per la presència de forts gradients de vorticitat potencial, especialment a les zones properes que limiten amb els seus contorns. Per aquest motiu és de suposar que per a una bona detecció i caracterització d'aquestes estructures, és necessària una bona resolució horitzontal i vertical de les dades.

S'ha creat un algoritme objectiu per a la detecció d'aquests plegaments basant-se només en una definició purament geomètrica d'aquestes estructures i, per tant, sense fer cap suposició d'entrada sobre el seu origen dinàmic. D'aquesta manera l'algoritme, aplicat sobre els camps tridimensionals de les principals variables meteorològiques, és capaç de detectar la presència d'una tropopausa dinàmica plegada, i d'enregistrar-ne les seves principals característiques geomètriques com són: les dimensions horitzontals, el gruix de la intrusió, la profunditat de penetració o l'amplitud de l'arc (distància vertical entre les dues tropopauses que defineixen la presència d'un plegament).

L'algoritme s'ha aplicat primerament sobre un any (desembre 2007 – novembre 2008) de dades d'anàlisi globals del model GFS amb el que s'ha pogut fer una caracterització geogràfica completa de plegaments de tropopausa per a l'hemisferi nord i sud. Els resultats, per una banda, es corresponent molt bé amb les climatologies existents, el que corrobora el bon funcionament de l'algoritme. Per una altra banda, la major resolució de la que consten les dades GFS utilitzades ofereix una descripció molt més fina en la que es pot observar amb més detall les diferents particularitats regionals.

Seguidament, l'algoritme també s'ha aplicat sobre els 10 anys de simulacions realitzades amb el model de mesoescala WRF i s'ha construït una climatologia de plegaments molt més robusta sobre una regió força extensa del sud-oest d'Europa, amb la Península Ibèrica al centre del domini. Aquesta climatologia mostra una bona concordança amb els resultats obtinguts durant un any d'estudi amb les dades GFS, tot i que les freqüències de plegaments observades són en general més petites. Aquesta disminució és deguda, per una banda, a la variabilitat interanual, i per l'altra, a una subestimació generalitzada de l'àrea total detectada en els diferents casos de plegaments de tropopausa simulats amb el model WRF respecte dels observats amb les dades GFS.

Tant l'anàlisi global com la climatologia regional corroboren les diferències entre els subtròpics i els extratròpics en la formació i característiques dels plegaments de tropopausa, i serveixen per a identificar els principals escenaris sinòptics que governen la intensificació d'aquests fenòmens.

També s'ha generat un producte que utilitza una combinació dels diferents parà-

metres geomètrics dels plegaments de tropopausa per a estimar les regions on és més probable que grans quantitats d'aire estratosfèric siguin transferides irreversiblement a la troposfera degut als casos més intensos de plegaments de tropopausa (STTFI: *Stratosphere-Troposphere Transport Folding Index*). Tot i la simplicitat del producte, l'STTFI reprodueix molt bé els trets més importants observats a les climatologies existents de transport estratosfera-troposfera basades en tècniques més complicades de trajectòries lagrangianes.

Finalment, s'ha efectuat una avaluació detallada sobre la capacitat del model WRF per a simular plegaments de tropopausa, i amb l'objectiu d'avaluar també la importància dels increments en la resolució de les dades a l'hora de millorar la representació dels plegaments de tropopausa. S'han realitzat comparacions durant un any sencer (desembre 2007 – novembre 2008), tant qualitatives com quantitatives, dels resultats del WRF amb, per una banda, les dades de baixa resolució JRA utilitzades com a inicialització de les simulacions, i per l'altra banda, amb les dades GFS que tenen una resolució semblant a la de les simulacions WRF. A part de comparar les freqüències de plegaments i les seves característiques estacionals, també s'ha analitzat un ampli ventall de diferents casos d'estudi individuals. Els resultats demostren que el model WRF és en general capaç de pronosticar els principals trets mesoescalars dels plegaments de tropopausa, millorant significativament la seva representació en comparació amb la descripció més grollera que ofereixen les dades d'inicialització JRA, especialment a les latituds mitjanes. Tot i aquesta millora significativa, s'ha observat que una definició pobra de les condicions inicials pot ser un obstacle important per a un complet desenvolupament de les intrusions estratosfèriques, especialment en algunes circumstàncies (p.e. pertorbacions ràpides entrant en el domini de simulació) i en algunes regions concretes (p.e. prop dels límits del domini).

Abstract

In this work, a subsynoptic characterization of tropopause fold structures is derived from one-year of global, high resolution GFS (Global Forecasting System, 0.3 degrees) data analyses and 10-years of daily WRF (Weather Reasearch and Forecasting) mesoscale simulations at 30 km resolution initialized with the Japanese 25-year Re-Analysis (JRA-25, 1.125 degrees). The dynamical tropopause, defined as a constant potential vorticity surface (2 PVU), is an important meteorological concept that under adiabatic and frictionless conditions acts as a material barrier between the troposphere and the stratosphere. Deformations of this layer such as foldings have a relevant influence on midlatitude weather systems and are a major mechanism of extratropical stratosphere-troposphere exchange. In the vicinity of these stratospheric intrusions, large vertical and horizontal gradients of Potential Vorticity (PV) are found, so that high resolution data is required for a direct characterization of these structures.

Based on a geometric definition of tropopause folds, a novel objective algorithm has been developed and applied over the 6-hours meteorological fields to unambiguously detect the presence of a folded dynamical tropopause. The methodology applied requires no assumptions on the dynamical origin of the folding, and it registers the main geometric features of each individual folded grid structure such as its horizontal dimensions, depth of penetration, thickness or the gap relative to the upper tropopause.

The application of the fold detection algorithm has served to characterize the geographical distribution of folding features on a global basis using one year of GFS data, and on a regional basis using a more robust 10-years WRF climatology over Southwest Europe. The analysis corroborates the differences between subtropics and extratropics in tropopause fold characteristics and formation, and serves to identify the main synoptic upper-level scenarios that drive the intensification of these structures. The geographical distribution and annual variability of stratospheric intrusions detected with the GFS analyses are in line with existing climatologies, supporting the competence of the fold searching algorithm, but providing a more

detailed portrait through the higher resolution of the GFS data. The 10-years WRF tropopause fold climatology shows a general good agreement with the one-year GFS observations, although WRF tropopause fold frequencies appear to be lower on average. This can be partly attributed to interannual variability, and partly to underestimation of the total folded area simulated by WRF relative to that observed by GFS, as revealed in individual tropopause fold case studies.

Additionally, a product that uses a combination of geometric tropopause fold parameters has been generated (Stratosphere-Troposphere Transport Folding Index, STTFI) to estimate the regions of the globe where the largest amounts of stratospheric air are most likely to be irreversibly transferred into the troposphere due to deep tropopause fold intrusions. Despite its simplicity, the STTFI reproduces the most important features captured in existing Stratosphere-Troposphere Transport (SST) climatologies based on Lagrangian trajectory techniques.

Finally, a detailed evaluation on the WRF model ability to simulate tropopause folds has been performed over an entire year (December 2007 - November 2008), with an eye at establishing the role of resolution enhancements at improving their simulation. Qualitative and quantitative comparisons between WRF results and both the initial JRA data and the GFS analyses have been performed over tropopause fold frequencies and individual tropopause fold events. The comparison demonstrates that the WRF forcing is in general able to forecast the main mesoscale features of the tropopause folds, significantly improving their representation with respect to the JRA coarse description of the initial state, particularly at midlatitudes. However, it has been observed that a poor definition of the initial conditions can be an important obstacle in tropopause fold performance, particularly under certain circumstances (e.g. rapidly traveling perturbations entering the domain) in some specific areas (e.g. close to the border of the simulation domain).

Contents

Acronyms and abbreviations

CHAMP Challenging Minisatellite Payload

DJF December, January and February

ERA European Re-Analyses

GFS Global Forecastig System

JJA June, July and August

JRA Japanese Re-Analyses

MAM March, April and May

PV Potential Vorticity

PVU Potential Vorticity Units

RWB Rossby Wave Breaking

SON Setember, October and November

STE Stratosphere-Troposphere Exchange

STT Stratosphere-Troposphere Transport

STTFI Stratosphere-Troposphere Transport Folding Index

TF Tropopause Folding

TST Troposphere-Stratosphere Transport

UTLS Upper-Troposphere Lower-Stratosphere region

WRF Weather Research and Forecasting model

Chapter 1

Motivation and Objectives

This thesis is framed within the TRODIM Project focused on the study of the extra-tropical tropopause and funded by the Spanish Government with the participation of eight research centres in Spain, Portugal and Cuba. In particular, the thesis is part of the subproject TROSAT undertaken at the University of Barcelona whose aim is to provide a subsynoptic characterization of the tropopause parameters using mesoscale simulation models and Meteosat images.

The tropopause represents the boundary between the troposphere and the stratosphere, two layers with marked differences on static stability, dynamical propierties and chemical composition (WMO 1986). It plays an important role at different temporal and spatial scales on chemical and dynamical interactions between both layers (Holton et al. 1995), and it can be extremely sensible to atmospheric changes (Hoinka 1998, Seidel et al. 2001, Santer et al. 2003). From the short to the several days scale, small tropopause potential vorticity anomalies can derive into strong stratospheric air intrusions, which can influence upper-level frontogenesis (Keyser and Shapiro 1986), rapid cyclogenesis (Uccellini 1990) and the evolution of severe weather mesoscale systems (Browning and Reynolds 1994, Thorpe 1997, Griffiths et al. 2000, Goering et al. 2001).

The main objective of the present work is the study and characterization of tropopause folds using relatively high resolution numerical model simulations, and contribute to the knowlegde of the properties of such structures.

The main scientific questions addressed in this thesis are:

1. To what extent is the resolution refinement of the atmospheric fields important to obtain an accurate picture of tropopause folds features? Tropopause folds typically occur on the vicinities of a sharp tropopause and strong temperature

and wind gradients. Under these conditions, it is reasonable to think that spatial resolution can play an important role in tropopause fold detection.

2. Is therefore a high-resolution tropopause fold characterization improving the existing tropopause fold climatologies? And how can the different geometrical features of foldings relate to conceptual models and hint at the dynamic mechanisms of tropopause fold formation and transport?

3. Is an operational forecasting model such as the WRF able to accurately represent the tropopause and in particular, to forecast tropopause fold structures? If so, a question that arises for future work, can the tropopause modelling be a useful tool for weather forecasting and analysis, and in particular, to predict severe weather mesoscale phenomena?

In order to meet the scientific questions outlined above, the following research plan is proposed:

1. Ten years of daily mesoscale numerical simulations will be obtained using the WRF model for a large midlatitude European area centered on the Iberian Peninsula with a spatial resolution of about 30 km and initialized with the 1.125° resolution Japanese ReAnalysis (JRA). Special attention will be paid to the extent and resolution of the vertical grid in order to achieve a good tropopause characterization: extension of the upper boundary model domain up to 10 hPa and an increment of the vertical refinement up to 51 levels within which 25 will cover the relevant region of folds between 600 and 100 hPa.

2. Previous work presented by Sprenger et al. (2003) proposed a methodology based on geometrical potential vorticity considerations to identify tropopause folds, which has widened the definition of such structures. Based on this work, a novel geometric algorithm will be developed to identify tropopause folds and their main characteristics: depth of intrusion, vertical dimension of the folded arch, thickness of the intrusion tongue and the horizontal dimensions.

3. The geometric fold searching algorithm will be applied to the high-resolution but limited area WRF output data in order to build a set of tropopause fold parameters and a detailed regional climatology with statistical features, geographical distribution and annual variability.

4. The results will be tested against the lower-resolution global JRA initial conditions and the high-resolution global GFS analyses (0.3° grid), which include observational and satellite assimilations, in order to improve the tropopause fold characterization and evaluate the capacity of the mesoscale WRF model to represent the tropopause and in particular the folding intrusion processes.

5. In addition, the tropopause fold characterization obtained from the high-resolution GFS data will be verified against the 1-year folding climatology presented by Sprenger et al. (2003), in order to validate the fold searching algorithm and enrich the global picture of tropopause fold formation.

6. Finally, tropopause maps of meteorological variables and vertical cross-sections of indentified tropopause fold cases will serve to evaluate and characterize individual tropopause fold processes.

Chapter 2

Introduction

2.1 The Tropopause

The tropopause represents the boundary between the tropospere and the stratosphere, two layers with marked differences on static stability, dynamical properties and chemical composition. The tropopause, then, is a transition zone of abrupt changes between the relatively well-mixed low-stable troposphere and the steady horizontally windy stable stratosphere (WMO 1986). Consequently, it can play an important role in the exchange of different substancies such as ozone or pollutants between both layers (Holton et al. 1995), and it can be extremely sensible to atmospheric changes (Hoinka 1998, Seidel et al. 2001). For exemple, Santer et al. (2003) found that the tropopause height has increased 200 m in the period 1979-1999 and that 80% of this increase can be explained by the stratospheric ozone depletion and the tropospheric greenhouse gas concentration raise.

The tropopause latitudinally decreases from the 16-18 km in the tropics to the 7-8 km in the poles. This altitude lowering is far from smooth with rapid drops in the subtropical and polar front jet regions (see Figure 2.1), where the tropopause can often show strong local discontinuities and even fold down to significant low levels. The tropical tropopause height can be explained in a first approximation by radiative-convection adjustment (Manabe and Strickler 1964, Highwood and Hoskins 1998) while in the extratropics, baroclinic eddies play a major role (Held 1982, Haynes et al. 2001). A complete representation of the mechanisms that help to maintain the extratropical tropopause remains uncertain. Recent findings from Haqq-Misra et al. (2011) suggest that stratospheric circulation can also be an important contributor.

Traditionally, the tropopause height is defined by its thermical properties as the lowest level at which the temperature lapse rate decreases to 2 K km^{-1} or less and

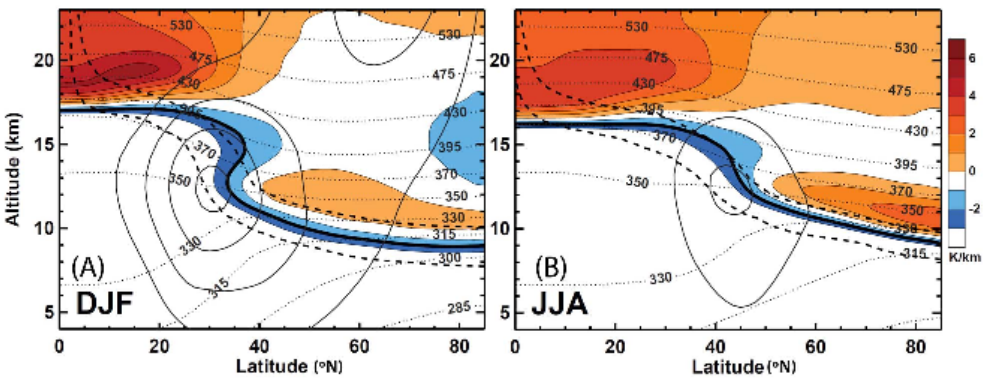

Figure 2.1: *Seasonal climatology of zonal mean Northern Hemisphere of static stability (dT/dz) in the UTLS (Upper Troposphere and Lower Estratosphere) region in altitude coordinates for (a) Desember-January-February and (b) June-July-August, from CHAMP GPS data for the period 2002-2008. The thick black lines represent the thermal tropopause (the -2 K km^{-1}. Dotted lines are isentropes. Black contours are zonal mean zonal winds with contours every 10 ms^{-1} (from ERA-interim for 2002-2008). Dashed lines are ±2 and 6 PVU isolines, also from ERA-interim. Figure from Gettelman et al. (2011).*

the lapse rate averaged between this level and any level within the next 2 km does not exceed 2 K km^{-1} according to the *World Meteorological Organization* (WMO 1957, Hoinka 1997). The thermal definition, therefore, denotes the vertical discontinuity in static stability, and it allows to define multiple tropopauses if the above mentioned criteria meets more than once in the vertical profile. Double tropopauses (DTs) are frequent in the subtropics and midlatitudes (Schmidt et al. 2006, Randel et al. 2007, Añel et al. 2008, Castanheira and Gimeno 2011, Peevey et al. 2012), where they form often in association with the subtropical jet and can extend for large areas towards the high latitudes. The physics and dynamics that maintain this double tropopause structure are not completely understood yet (Parracho et al. 2014). Randel et al. (2007), Pan et al. (2009), Olsen et al. (2008) and Parracho et al. (2014) have observed signatures of tropical upper-tropospheric air (air with relatively high concentrations of water vapor, low potential vorticity and low static stability) intruding between the two tropopauses and towards the lower extratropical stratophere (see Figure 2.2), suggesting the double tropopause occurs by a poleward extrusion of the upper tropical tropopause ovarlaying the extratropical tropopause. However, Wang and Polvani (2011) and Añel et al. (2012) suggest that extratropical phenomena associated with Stratosphere-Troposphere Exchange (STE), such as tropopause folds, can be responsibles in most cases of a double tropopause formation in midlatitudes, since they found signatures of tropospheric air between the two tropopauses coming from high latitudes.

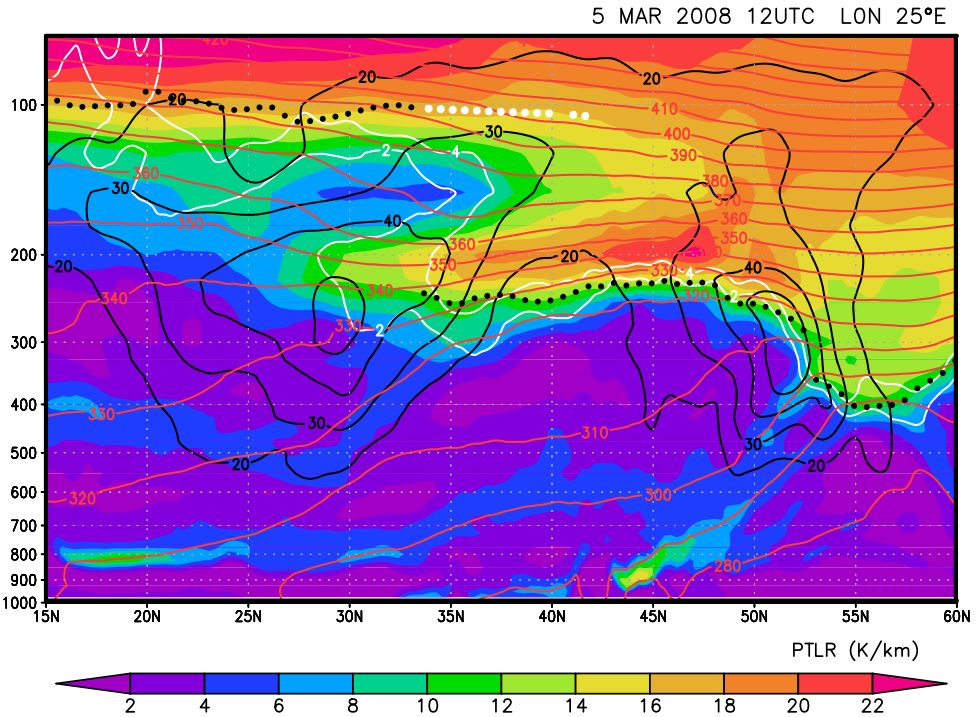

Figure 2.2: *Latitudinal cross-section of potential temperature lapse rate (static stability, $d\theta/dz$) in the Northern Hemisphere at 25° E longitude on March 5th, 2008 at 12 UTC derived from GFS analysis. Black contours are 20, 30, 40 and 50 ms^{-1} zonal wind. White contours are 2 and 4 PVU isolines. Red contours are isentropes with 10 K intervals. Dots represent the thermal tropopause, depicted in white the presence of a the second tropopause.*

The thermal definition is operationally useful as the height of the tropopause can be easily obtained from radiosonde vertical profiles, but has limited physical relevance. The ambiguities of the thermal definition in some locations and the availability of three-dimensional analysis motivated a new definition of the tropopause based on dynamical properties. Reed (1955) was the first to used the potential vorticity (PV) to defined the dynamical tropopause, precisely to study a tropopause fold phenomenon. This dynamical tropopause definition highlights the quasi-material character of the tropopause (Hoskins et al. 1985) since PV is conserved under adiabatic and frictionless conditions (Ertel 1942).

The tropopause can also be defined from a chemical point of view as the region that corresponds to the sharp transition in chemical species concentrations. After a large ozone-sounding analysis, Bethan et al. (1996) proposed the definition of

an ozone tropopause based in a set of ozone gradient and ozone values criteria. They adjusted these criteria to highly agree with the 1.6–2 PVU (potential vorticity units) dynamical tropopause, since strong correlations between ozone and PV exist in the lower stratosphere (Danielsen 1985, Beekmann et al. 1994). Compared to the thermal tropopause, they found that the ozone tropopause was on average 800 m below.

More recently, the chemical tropopause has been identified using ozone–carbone monoxide correlations (Zahn et al. 2004, Pan et al. 2004). In particular, Pan et al. (2004) found that the chemical extratropical tropopause defined that way should be considered as a transition layer (more than a surface) with mixing of stratrospheric and tropospheric air masses, and that its center is stastistically associated with the thermal tropopause. Additionally, they argue this transition layer indicate the effect of two-way exchange between the troposphere and the stratrosphere.

2.1.1 The dynamical tropopause

The PV-based dynamical tropopause definition allows to interpret the tropopause as a quasi-material surface, and the potential vorticity as a quasi-passive tracer. Besides, another relevant advantage is that given the PV distribution, the wind, pressure and temperature fields can be deduced under the thermal wind balance condition and a known initial state (the invertibility principle, see Hoskins et al. 1985).

Although the tropopause that way is identified as the transition region with strong enhancement of potential vorticity, a simple constant PV value is chosen instead of a gradient threshold. The PV definition was introduced by Rossby (1940) and Ertel (1942), and it can be calculated following the Ertel's Potential Vorticity equation

$$PV = -g\left(\zeta_\theta + f\right)\left(\frac{\partial\theta}{\partial p}\right), \tag{2.1}$$

where g is the gravity constant; f, the Coriolis parameter; θ, the Potential Temperature; p, the pressure and ζ_θ is the vertical component of the relative vorticity in isentropic surfaces

$$\zeta_\theta = \tilde{\mathbf{k}} \bullet \nabla \times \tilde{\mathbf{V}} = \left.\frac{\partial v}{\partial x}\right|_\theta - \left.\frac{\partial u}{\partial y}\right|_\theta, \tag{2.2}$$

where $\tilde{\mathbf{V}}$ is the wind vector and u and v are, respectively, the zonal and the meridional components.

The units of PV are $m^2 s^{-1} K kg^{-1}$, but for convenience is mesured in PVU where 1 PVU $= 10^{-6} m^2 s^{-1} K kg^{-1}$. The WMO (1986) defined the dynamical tropopause

by a value of 1.6 PVU, however, a wide range of values from 1 to 4 PVU can be found in the literature. In the endeavour to find the value that better agrees with the thermal tropopause, Hoerling et al. (1991) and Hoinka et al. (1996) suggested a threshold value of 3.5 PVU for the extratropics, though it was strong dependent on the region and the synoptic situation. In particular, they found that the PV-based definition fails in regions of small absolute vorticity such as the tropics, where it is then considered to correspond with the 380 K potential temperature surface (Holton et al. 1995, Highwood and Hoskins 1998, Seidel et al. 2001), and sometimes under strong anticyclonic conditions in the extratropics.

Other studies have argued the suitability of other PV values. Holton et al. (1995) used a value of 2 PVU to describe the dynamical tropopause in the extratropics, and since then many authors have chosen this value, which is become the more commonly used. The dynamical tropopause definition is particularly useful to separate air masses during tropopause folds events (Reed 1955, Reed and Danielsen 1959, Danielsen 1968, Shapiro 1980).

2.1.2 Tropopause Maps Analysis

A tropopause map consist of a 2-dimensional projection of the meteorological variables in the dynamical tropopause surface (a constant Ertel's potential vorticity surface, usually 2 PVU). Tropopause maps are particularly useful when the interpolated variables are the potential temperature accompanyied with the wind. They were first used by Hoskins and Berrisford (1988) to study, in conjunction with lower-troposphere analysis, a ciclogenesis event (storm 15-16 October 1987), and have been later applied to study a wide range of phenomena.

Earlier, Hoskins et al. (1985) presented an exhaustive analysis of how isentropic potential vorticity maps (potential vorticity represented in isentropics surfaces) along with a surface potential temperature distribution "lead to a very clear and complete picture" of the atmospheric dynamics. In adiabatic and fritionless conditions, these maps represent a conserved variable along the surface of another conserved variable, which means that with the wind field superposed one may deduce the conservative advection and tendecy of the field (PV). In that way, however, as the dynamical tropopause intersects different isentropic surfaces, one needs many different isentropic potential vorticity maps to understand the three-dymensional distribution and advection of PV. Alternatively, if the potential temperature is depicted on a constant surface of potential vorticity, the same previous advantatges from the two conservative variables is preserved, with the surplus that a single two-dimensional chart provides a fully description of atmospheric PV distribution (Morgan and Nielsen-Gammon 1998).

The distribution of potential temperature contours on the 2 PVU dynamical tropopause indicates the topography of that surface. Strong gradients represent a slope sharp tropopause and an upper-frontal zone which most likely will be associated with an upper-level jet stream. A cold region represents a cyclonic PV anomaly (positive) where the tropopause sinks into the troposphere, and a warm region highlights an anticyclonic anomaly (negative) and an exceptional high tropopause. This can be observed in Figure 2.3, which shows the vertical structure of potential temperature and the flow circulation induced by two isolated PV anomalies of either sign (positive in Figure 2.3a, negative in Figure 2.3b) calculated by Dr. A. J. Thorpe (Thorpe 1985, Thorpe 1986) from a simplified atmosphere, which its basic state consists of two layers with two different constant potential vorticity gradient representing the troposphere and the stratosphere (six times larger in the stratosphere) and a sharp tropopause boundary between them (bold line in Figure 2.3). There is a cold (warm) anomaly in the center of the tropopause for the positive (negative) PV anomaly which induces a cyclonic (anticyclonic) flow in the sourrounding atmosphere. Several crossing isentropes are present on the inclined tropopause regions, which can be identify by strong potential temperature gradient and wind maxima on a 2-dimensional tropopause map.

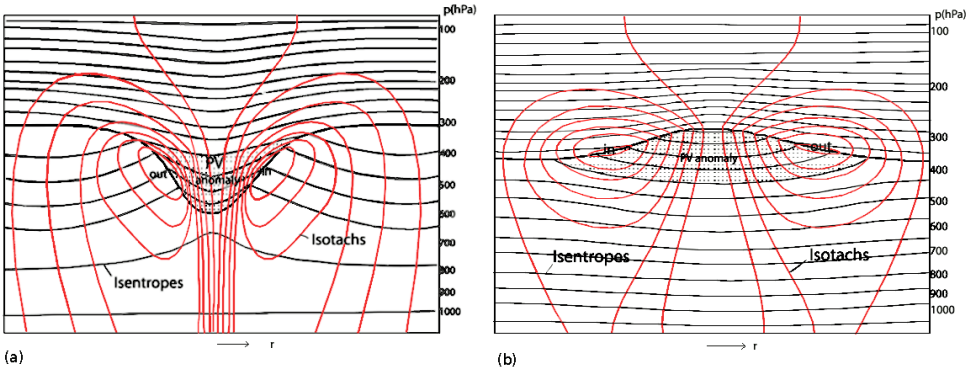

Figure 2.3: *Flow induced by isolated PV anomalies with circular symmetry for a) a positive anomaly and b) a negative anomaly. The bold line represents the dynamical tropopause. Black contours are isentropes. Black contours are isentropes and red countours are isotachs. In a) the sense of the wind is cyclonic and in b) it is anticyclonic. Calculations were made by Dr. A. J. Thorpe (Thorpe 1985, Thorpe 1986). Images from KNMI and ZAMG.*

An exemple of a real event that shows a positive potential vorticity anomaly in the upper troposphere occurring on January 13th, 2008 at 12 UTC and simulated with the mesoscale WRF model can be observed in Figure 2.4. The potential temperature tropopause map (left) shows a cold anomaly over Italy with cyclonic strong winds around its maximum. The vertical cross-section along the segment A-B (right) shows

a close correspondance with that in Figure 2.3a, though in this real case the anomaly is not perfectly symmetric, stronger gradients and a steeper tropopause are found on its west region.

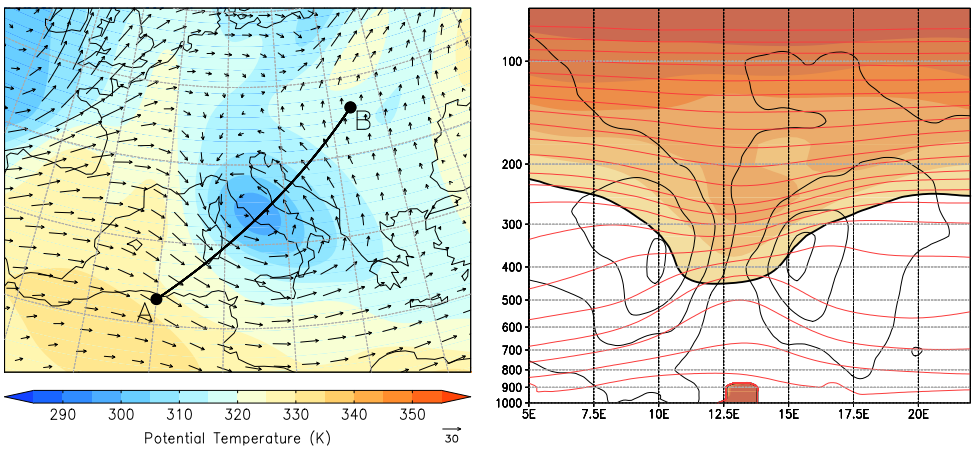

Figure 2.4: *Positive potential vorticity anomaly in the upper troposphere occurring on January 13th, 2008 at 12 UTC. Data from a 24 hours WRF simulation. Left: potential temperature tropopause map (2 PVU surface) and wind field superposed (vector legend in ms^{-1}). Right: Vertical cross-section along the segment A-B from the left. The bold line represents the dynamical tropopause (2 PVU contour). Countours of 2, 4, 6, 8, 10 and 14 PVU are shaded in colors. Red contours are isentropes in 5 K intervals till the 330 K isentrop (below the 200 hPa) and in 10 K intervals above it. Black countours are isotachs in 10 ms^{-1} intervals. The zero isotach is omitted, and as it can be observed in the left, the sense of the wind is cyclonic.*

As mentioned above, under adiabatic and frictionless conditions the potential temperature is advected over the dynamical tropopause surface (the tropopause map), thus, the evolution of the field can be deduced. Additionally, if the above mention conditions are not valid and the generation or destruction of potential temperature anomalies occur, it could be possible to isolate them from the conservative processes and conceptually estimate their effects (Morgan and Nielsen-Gammon 1998).

Pressure tropopause maps can be often preferred since the topography of the tropopause is better represented and it can be easier to interpret. However, the pressure is not a conserved variable and some of the previous analysis advantages may be are loss.

Morgan and Nielsen-Gammon (1998) present different techniques to represent such tropopause maps and a guide to interpret them in different situations. Lately, Nielsen-Gammon (2001) used this tropopause fold analysis technique to visualized the dynamic features of the tropopause from global data and for a long period of 20

years. He observes and describes in terms of potential vorticity a wide range of the most relevant atmospheric phenomena.

2.2 Tropopause Folds

The first to observe a tropopause fold was Reed (1955) in the study of an upper-level frontogenesis. He found, along with the intense portion of the frontal zone, a tongue of stratospheric air descending into the lowest levels of the troposphere (below the 3 km) accompanied with a folded tropopause in terms of potential vorticity. This main characteristics are summarized in figure 2.5, which shows an schematic picture of a typical tropopause fold shape and its associated atmospheric conditions.

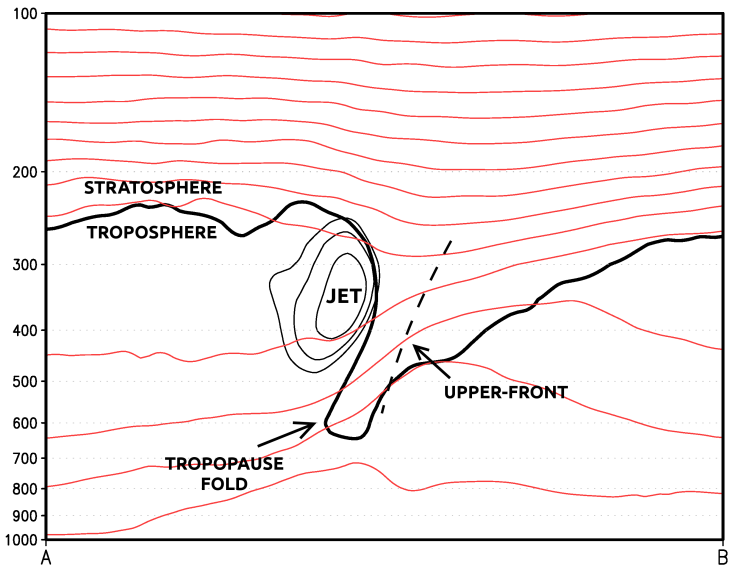

Figure 2.5: *Conceptual model of atmospheric conditions in a cross-section tropopause fold event.*

Thereafter and since nowadays, tropopause fold structures have been widely studied evidencing their importance in different atmospheric processes: they are close related to upper-level frontogenesis and jet-stream dynamics (Keyser and Shapiro 1986, Shapiro and Keyser 1990), they can influence rapid cyclogenesis (Uccellini 1990) and the evolution of severe weather mesoscale systems (e.g. Browning and Reynolds 1994, Thorpe 1997, Griffiths et al. 2000, Goering et al. 2001), and they are one of the major mechanisms of extratropical stratosphere-troposphere exchange (e.g. Shapiro 1980, Vaughan et al. 1994, Lamarque and Hess 1994, Holton et al. 1995, Stohl et al. 2003).

Chapter 3

Data and Methodology

The specific data and methodologies used to characterize fine-scale structures of the dynamical tropopause such as tropopause folds are presented in this chapter. First, the model configuration of the 10-years regional simulations performed and the additional sets of data used are described. Secondly, the methodology used to visualized and analyzed the tropopause characteristics and atmospheric conditions at spefic times and locations from the different model datasets is detailed. Then, an objective technique based on a pure geometric algorithm to unambiguously detect tropoause folds is applied over the long datasets and explained below in section 3.3. Finally, in the last section of this chapter, three different aspects of the mesoscale model configuration are discussed.

3.1 Model Setup and Data

In order to achieve a regional study and subsynoptic characterisation of tropopause fold structures, 10 years (1999 - 2008) of mesoscale simulations over Europe have been performed with the Weather Research and Forecasting (WRF) model. The Japanese 25-year Reanalysis (JRA-25) dataset has been used to initialized the model and to insert boundary conditions. So as to obtain a global picture of such structures and to compare and validate the WRF output data, a year (December 2007 - November 2008) of Global Forecast System (GFS) analyses with similar horizontal and vertical resolutions have been used. Besides, reanalysis from the European Center for Medium-Range Weather Forecasts (ECMWF) have been employed for an specific case study. In this section, a description of all the data mentioned will be given as well as detailed information about the model set-up and runs performed.

3.1.1 Japanese Reanalysis (JRA-25)

The Japanese 25-year Reanalysis dataset (hereafter referred to as JRA) is the first long term reanalysis undertaken in Asia by the Japanese Meteorological Agency (JMA) and Central Research Institute of Electric Power Industry (CRIEPI) (Onogi et al. 2007). It covers the period 1979-2004, extended to present by the product JCDAS (JMA Climate Data Assimilation System) that takes over the same observational assimilation system. This provides an homogeneous, consistent and high-quality data for climate diagnosis and operational work, being a suitable data for mesoscale regional models to perform numerical experiments for severe events in the past. The dataset consists of 6-hourly atmospheric reanalysis fields with an horizontal resolution of about 120 km and 40 hybrid-sigma levels in the vertical up to 0.4 hPa.

Many advantages have been found in the JRA-25 reanalysis (see Ohkawara 2006 and Onogi et al. 2007) but the main reasons in this study to choose this new data to initialize the WRF model can be summarized in three: i) they are at the moment the finest reanalysis freely available (see table 3.1) for the scientific community that cover up to nowadays, ii) the vertical resolution in the JRA-25 system is as dense around the tropopause and lower stratosphere as that in the ERA-40 system, and iii) it represents a good innovation to implement this new data to initialize the WRF model.

Table 3.1: *Summary list of available reanalysis. After Onogi et al. (2007).*

Name	Organization	Period	Resolution	Assimilation	Memorandum
JRA-25	JMA/CRIEPI	1979-present	T106 L40	3DVAR	continues as JCDAS since 2005
ERA-15	ECMWF	1979-1993	T106 L31	OI	completed in 1996
ERA-40	ECMWF	1957.9-2002.8	TL159 L60	3DVAR	completed in 2003
NCEP-NCAR (Reanalysis-1)	NCEP-NCAR	1948-present	T62 L28	3DVAR	continues as CDAS
NCEP-DOE AMIP-II (Reanalysis-2)	NCEP-DOE	1979-present	T62 L28	3DVAR	continues as CDAS
GEOS1	NASA/DAO	1980-1996	2x2.5 L20	OI+IAU	completed up to 1996

T: Triangular truncation, TL: Triangular with Linear reduced Gaussian grid, L:Vertical layers. T106 and TL159 are comparable to a lat-lon grid with intervals of about 110 km, while T62 is comparable to the same with intervals of about 180 km.

The above reanalysis summary table shows that JRA and NCEP (I and II)

reanalysis continue the product to present times but the grid resolution of the latter is too coarse to downscale the data to 30 km resolution with the mesoscale model in just one nesting step. Besides, ERA-40 presents slightly better horizontal and vertical resolution than the JRA but the product stops in 2002.

WRF runs have been initialized with the atmospheric fields of temperature, geopotential height, horizontal winds and specific humidity from a particular JRA product where the variables can be found interpolated in 24 vertical pressure levels. Surface products of moist and temperature, horizontal winds and pressure reduce to mean sea level have also been used. The JRA-25 atmospheric fields mentioned have also been employed as 6-hourly boundary conditions in the WRF simulations carried out.

3.1.2 WRF Model Configuration

The WRF (Weather Research and Forecasting) model is a mesoscale numerical weather prediction system developed by the University Corporation for Atmospheric Research (UCAR). This limited area model is in public domain and is freely available for the community research, for this reason it has more than 20 thousand users in more than 130 countries nowadays*. The dynamical cores are Eulerian, compressible and non-hydrostatic that use terrain-following vertical coordinates. The physics package offers multiple parameterization options in radiation, micro-physics, convection, diffusion, surface, planetary boundary layer, etc. that allows a broad spectrum of applications across scales ranging from meters to thousands of kilometers. Moreover, WRF supports both operational forecasting and atmospheric research, giving the possibility of simulate real and ideal cases, and last versions can also be used for regional climate simulations.

In this work, the model domain is centred at 45° N and 2° W and covers an area of about 7.400 x 5400 km^2 in an horizontal grid of 247 x 179 points, with a resolution of 30 km at the center of the domain. Figure 3.1 (left) shows the precise area set up for the simulations. In the vertical, some aspects have been taken carefully to well represent the dynamical tropopause: extension of the upper boundary model domain up to 10 hPa and refinement of the vertical resolution by an increment of the vertical levels (51), with special emphasis on the lower stratosphere and upper troposphere (see Figure 3.1, right). From the 50 levels, about 25 cover the relevant region for folds between 600 and 100 hPa.

The main physical options used were: WRF Single-Moment 5-class (WSM5) microphysical parameterization (Hong et al. 2004); the new Kain-Frintsch convective parameterization (Kain 2004); the 5-layer thermal diffusion scheme for the land-surface parameterization; the Yonsei University (YSU) planetary boundary layer

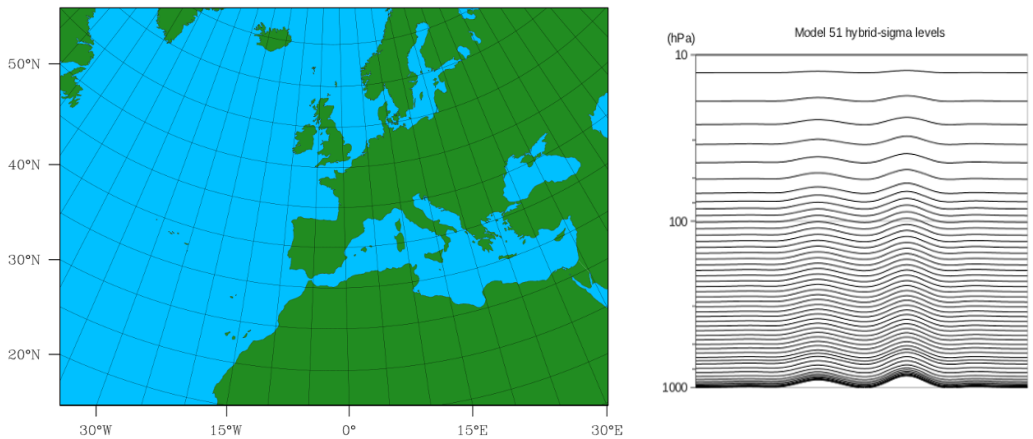

Figure 3.1: *Model domain (left) and model vertical levels (right)*

(PBL) scheme (Noh et al. 2003); Dudhia shortwave radiation (Dudhia 1989); and the Rapid Radiative Transfer Model (RRTM) longwave radiation (Mlawer et al. 1997). The WSM5 scheme explicitly resolves water vapor, cloud water/ice, rain and snow. The cumulus scheme chosen is the more convenient at midlatitudes with grid lengths near 25 km. It uses a simple cloud model with updrafts and downdrafts and considers the effects of entrainment and detrainment. The soil thermal diffusion scheme only takes into account the ground and soil temperatures and the thermal properties depending on land use. It provides heat and moistures fluxes for the PBL. The PBL parameterization used (YSU) in its turn is a first-order nonlocal scheme that includes counter-gradient terms to represent heat and moisture fluxes. The Dudhia shortwave radiation scheme is a simple downward integration that considers water vapor and cloud absorption, cloud albedo and clear-sky scattering. It does not consider the ozone effect although ozone can have some significant influence since the model top is above the 50 hPa (up to 10 hPa). An evaluation of that parameterization option is discussed later in section 3.4.3. Finally, the longwave radiation RRTM option uses tables for efficiency and accounts for multiple bands, trace gases and microphysics species.

As a limited area model, it needs known data for the initial state and the regularly injection of information around the domain boundaries. As seen in the previous section, JRA atmospheric fields of temperature, geopotential height, horizontal winds and specific humidity, as well as surface products of moist and temperature, horizontal winds and pressure reduce to mean sea level have been used for that purpose.

Since 10 years of mesoescale simulations wanted to be performed, the idea of

making long continuous model runs with the analysis nudging WRF option was considered both for saving computational resources and to avoid small leaps in the image sequences. However, analysis nudging has other disadvantages in comparison to normal reinitializations runs and these were also analyzed. After an evaluation of both options, discussed later in section 3.4.1, the reinitialization method was chosen.

Therefore, the model was reinitialized every day at 12 UTC until cover the 10 years (from 31 December 1998 to 31 December 2008) and each simulation run for 36 hours having an overlap of 12 hours with the previous simulation and a 12-hour overlap with the following one. In figure 3.2, an illustration diagram of this reinitialization process can be observed. Each line represents a new run that gives output fields every 6 hours (marked with vertical dashes) and the first output of each run corresponds to the initialization time, that is, the analysis fields. Notice here that the analysis can be compare with the 24h-simulation fields from the previous run.

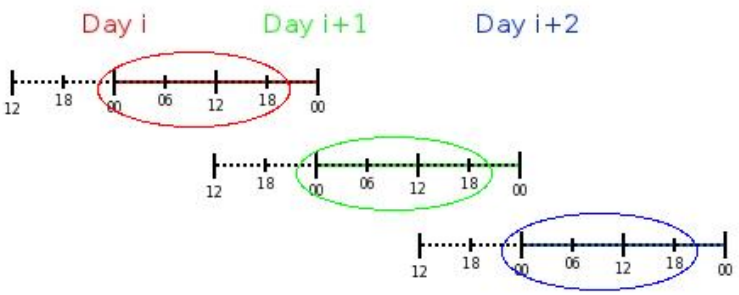

Figure 3.2: *Simulation reinitialization diagram*

When a long period analysis is required or a long sequence of images involving more than one day is displayed, it is desired to avoid the overlapping time outputs. As that overlap extends up to the first 12h forecast, the first output fields of each run (at 6h forecast) have not been considered, avoiding, thereby, possible "spin-up"[1] problems and offering more time forcing to the model. Therefore, a 10-year simulations database has been established with the data outputs of 4 different time steps for each run, corresponding to the 12, 18, 24 and 30 hours forecast. That way, the output fields of one day (at 00, 06, 12 and 18 UTC) belong to the same run. This is illustrated in figure 3.2 for clarification, with different colours for the data outputs chosen and belonging to different runs.

[1] When the model starts, it takes some time to gradually build up horizontal and vertical motions and to adjusts the model to the initial conditions not consistent with its numerics and physics.

3.1.3 GFS Analyses

One year (December 2007 to November 2008) of Global Forecast System (GFS) analyses have been used to investigate the global and seasonal distribution and preferred areas of Tropopause Fold formation and to validate the WRF simulations carried out. NCEP implemented major changes to its Global Forecast System on May 2005, remarkably increasing the horizontal resolution from approximately 50 km (the known GFS T254) to approximately 35 km (the new GFS T382). In the vertical, 64 hybrid-sigma layers cover the atmosphere up to 1 hPa, though the data package used contained the different variables interpolated in 47 pressure levels offering a good coverage of the tropopause region with a 25 hPa increment. The similarity in resolution with the WRF outputs (∼30 km in the horizontal) makes this data especially suitable for a comparison and evaluation of the simulations performed. In addition, two major advantages can be attributed to this data. On the one hand, as a global model, it does not suffer from boundary condition problems associated with limited area models (LAMs), and on the other hand, the analyses include a large set of observational assimilated data from rawinsondes, satellites, aircrafts, surface stations and others, giving a consistent and a good estimation of the real atmosphere state. Moreover, some aspects of the data assimilation system and the assimilated radiance were improved in these new analyses. More information can be found in Campana et al. (2005).

3.2 Tropopause Visualization and Characterization

Different types of visualization of the different meteorological fields can be used to analyze the tropopause region. Representations on different pressure levels of the upper-troposphere or representations of potential vorticiy (PV) on different isentropic surfaces are distinc useful examples that are used in various occasions during this work. However, a propitious approach to characterize and diagnose the dynamical tropopause and its evolution is with the so called "Tropopause Maps". They consist of the projection of the different variables on a constant PV surface (isertelic analysis) that represents the tropopause itself (e.g. the 2 PVU surface). Tropopause maps were first introduced by Hoskins and Berrisford (1988) and have since then been applied to a wide range of phenomena. They have the ability to convey a large amount of information in a sigle chart. For example, the representation of potential temperature in the 2 PVU surface preserve the advantages of isentropic PV maps of conservation under adiabatic and frictionless conditions and invertibility, and at the same time, the three-dimentional PV distribution is condense into a single two-dimensional map.

The technique used to display tropopause maps from the gridded datasets availables in this work is the "direct interpolation" method. This method has the advantage, in comparison to the "fill overlay" or "contour superposition" techniques proposed by Morgan and Nielsen-Gammon (1998), that all the meteorological variables can be vertically interpolated to the desired surface and a complete two-dimensional description of the tropopause is therefore possible. However, in regions of strong gradients and discontinuities such as the vicinities of tropopause folds, this method may lead to contouring difficulties (Morgan and Nielsen-Gammon 1998) that may be, in any case, strongly reduced with increased grid resolution. The refined mesoescale simulations performed and the high resolution of the GFS data used have enough horizontal and vertical resolution to well resolved the tropopause in such cases and the direct interpolation method becomes the best choice to derive tropopause maps. Moreover, in specific cases of tropopause folds where the tropopause can be bi-valued, apart from using vertical cross sections for a good vertical illustration, tropopause maps from both different levels (the upper tropopause and the lower tropopause) can be obtained (detailed below) and they can provide additional interesting information.

The direct interpolation method is based on a two step process to derive tropopause maps. The first step involves computing PV from common meteorological data fields at each point of the three dimensional grid. The second step focuses on the searching for the dynamical tropopause surface in the 3D PV space and the interpolation of any desired variable (potential temperature, pressure, winds, etc.) to this surface.

i) Potential Vorticity computation:

The derivation of PV is done following the definition of the Ertel's Potential Vorticity equation

$$PV = -g\left(\zeta_\theta + f\right)\left(\frac{\partial \theta}{\partial p}\right), \tag{3.1}$$

where g is the gravity constant; f, the Coriolis parameter; θ, the Potential Temperature; p, the pressure and ζ_θ is the vertical component of the relative vorticity in isentropic surfaces

$$\zeta_\theta = \tilde{\mathbf{k}} \bullet \nabla \times \tilde{\mathbf{V}} = \left.\frac{\partial v}{\partial x}\right|_\theta - \left.\frac{\partial u}{\partial y}\right|_\theta, \tag{3.2}$$

where $\tilde{\mathbf{V}}$ is the wind vector and u and v are, respectively, the zonal and the meridional components.

Hence, the meteorological fields needed are the zonal and the meridional winds, the potential temperature and the pressure. Notice, though, that WRF output fields (and GFS analyses) are in constant pressure levels and all partial derivatives in this equation may be done along constant potential temperature surfaces. The

equivalent equation in constant pressure surfaces becomes

$$PV = -g \left[\left(\frac{\partial v}{\partial x} - \frac{\partial u}{\partial y} + f \right) \left(\frac{\partial \theta}{\partial p} \right) - \frac{\partial v}{\partial p} \frac{\partial \theta}{\partial x} + \frac{\partial u}{\partial p} \frac{\partial \theta}{\partial y} \right] \tag{3.3}$$

The units of PV are $m^2 s^{-1} K kg^{-1}$, but for convenience is mesured in PVU where $1PVU = 10^{-6} m^2 s^{-1} K kg^{-1}$.

ii) Dynamical tropopause searching and interpolation:

Once the PV is derived at every single point of the 3D grid, the dynamical tropopause, define as a constant PV surface (2 PVU), can be searched at each horizontal grid column by starting at the top of the column where PV is always greater than 2 PVU and working down at successive vertical levels until the 2 PVU is crossed. Then, taking the PV values inmediatly above and below the 2 PVU, the exact point can be found, as well as any meteorological variable desired, with an easy interpolation.

This is the general way of searching for the 2 PVU surface. However, as abovementioned, during folding structures the dynamical tropopause can be often bivalued and, in a procedure like this, only the upper dynamical tropopause is represented. To look also for the lower tropopause surface, the search should start from below, where typically PV is lower than 2 PVU, and then proceed upward untill the 2 PVU surface is found. The difference between the two isertelic fields is then zero except where the tropopause is folded, and the magnitud of the difference gives information about the fold characteristics such as the vertical extend if the analyzed fields are, for example, the geopotential height or the pressure level.

However, starting the search from below can arise some problems. Occasionally, bubbles of high PV (greater than 2 PVU) can be found in the troposphere due to surface friction or diabatic moist processes. After checking a sample of cases, it has been observed that most of these high-PV patches remain closed to the surface and that starting the search at 700 hPa avoids the major part of the dilemma. Unfortunately, the question is not entirely solve that way and the lower tropopause visualization can contain some inaccuracies. Moreover, the 700 hPa constraint may also limit special deep tropopause fold intrusions and underestimate their real vertical extension. However, for a general dynamical tropopause visualization that criterion is working well for the majority of cases, and during specific case studies other kind of analyses such as vertical cross sections have been used additionally to unambiguously characterize tropopause folds events. The matter becomes relevant during the application of the geometric algorithm over the long sets of data to objectively discriminate real tropopause fold caese and it is solved through an air classification method detailed in the following section 3.3.2.

3.3 Tropopause Fold Detection

Over the last 15 years many algorithms have been used to detect the presence of tropopause folds from different kind of data: ozone, vertical radio-sounding profiles, meteorological analysis, satellite images, etc. All of them use a combination of some of the fold characteristics to identify a fold structure of the tropopause and distinguish it from a mere anomaly. In this section, first a brief description of the different algorithms found in the literature is given. Afterwards, a detailed explanation of the algorithm adopted in this work is presented.

3.3.1 Tropopause Fold Searching Algorithms

Van Haver et al. (1996) developed and algorithm using ozone/radio-sounding profiles to detect folds as ozone rich, stable and dry layers. They stipulated 5 conditions with their own threshold values to systematically identify folds: i) location of a region with an ozone mixing ratio enhance by at least 25% compared to the climatological mean and compared to adjacent minima in the ozone profile, ii) a vertical potential temperature gradient larger than $11,5K/100hPa$, iii) relative humidity below 25%, iv) a wind profile that goes beyond $20m/s$ in the vicinity of the layers found in conditions i), ii) and iii) that ensures the presence of an upper tropospheric jet stream and v) a vertical wind shear greater than $5ms^{-1}km^{-1}$ over at least $2km$ in the folding region observed to confirm the presence of an upper level front. The algorithm was verify for a test period of two years (1991-1992) by analyzing weather maps and cross sections of PV, potential temperature and winds from ECMWF assimilations.

Concurrently, Speth et al. (1996) and Blonsky and Speth (1998) developed a similar ozone-based algorithm working also with ozone/radio-sounding profiles. The main variation is that they used a PV criterion from ECMWF analysis instead of a combined stability/vertical wind shear. Beekmann et al. (1997) gives a comparison of both algorithms revealing that all cases detected by Speth et al. were also detected by Van Haver et al.. On the contrary, the latter found more than double cases for the same period. Thus, the PV criterion used by Speth et al. is more restrictive and one possible reason could be the grid coarseness - particularly the vertical resolution about 1.5 to 2 km - of the ECMWF data used (Beekmann et al., 1997).

In both cases, algorithms are based on vertical profiles captured in a small area of study and the intention of covering the whole globe with vertical soundings is always complex. Elbern et al. (1998) used ten years of global ECMWF analysis to derive regional and temporal tropopause folds statistics since no tropopause fold climatologies were still available. The main problem they were heading up was the

coarseness of the data grid (2.8 degrees on the horizontal) that had not enough resolution bearing in mind the typical lengths scales of these structures (∼100 km and ∼1000 km, transversal and longitudinal direction respectively). So, they proposed using secondary indicators with a patter matching algorithm to identify tropopause folds. First, they looked for i) relative potential vorticity maxima - with a minimal value of $2\Delta 10^{-6} KPa^{-1}s^{-1}$ to exclude small undulations - on the 400 hPa level to ensure low stratospheric potential vorticity values in the middle troposphere and then, they looked for ii) coincidence within a small distance of a Q-vector divergence maxima between the 400-500 hPa levels to discern between a mere PV anomaly and a tropopause fold with its frontogenetic forcing (characterized by high values of Q divergence) associated. A modified pattern matching algorithm, first design by König et al. (1993) for cyclone identification, was used to identify both occurrences with proper thresholds values accurately evaluated with mesoscale model runs (four episodes for each season) with an horizontal resolution of 40-50 km and 30 vertical levels.

That way, with model analysis data, the whole globe could be covered but it is still a big challenge to recover it with observational data. Wimmers and Moody (2004aa, 2004ab) developed and empirical model to detect tropopause folds from satellite water vapor spatial gradients. They based the algorithm on a robust relationship between tropopause folds and upper tropospheric specific humidity gradients that are resolved by the altered water vapor (AWV) GOES product. Unfortunately, they could not found a proportionality between tropopause fold size and AWV gradient magnitude, instead the model estimates the distribution of both actively developing and small residual tropopause folds.

Rao et al. (2008) described a method to identify tropopause folds from VHF wind-profiling radar measurements and used 11 years (1997-2007) of observations with ESRAD (a radar located at Esrange, northern Sweden) to study the seasonal cycle and interannual variability of tropopause fold over an Artic station. A similar algorithm is later used by Antonescu et al. (2013) to derive a five-year (2006-2010) tropopause fold climatology based on data from a VHF radar located at Capel Dewi, in mid Wales (see both references for a further description of the algorithm). The main advantage of this technique is that VHF radars offer extraordinary vertical (150/300 m) and temporal (1 min) resolution observational data. However, in the same way as sounding profiles, the radar can only detect tropopause folds at a certain location missing information about the fold horizontal extend and causing climatological results to be subject to the spatial distribution and variability of tropopause folds.

Croci-Maspoli (2002) and Sprenger et al. (2003) proposed a new methodology to identify folds from global analysis data based on a pure geometric definition of

a tropopause fold. Taking the 2 PVU value as the one that defines the "dynamical tropopause", they suggested to identify tropopause folds as multiple vertical crossings of that PV isosurface. In contrast to the work by Elbern et al., that method do not assumptions on the dynamical origin of the folding but it needs higher data resolution. Sprenger et al. had available ECMWF analysis with 60 vertical levels and less than 1° horizontal resolution, numbers comparatively higher than the data used by Elbern et al.. They tested the algorithm over 1-year period and found similar, although stronger, annual cycle and geographical distributions as Elbern et al.. The main discrepancies occur on the shallow and medium subtropical fold activity due to the difference on both fold definitions used. Elbern et al. criterion is based on PV at 400 hPa level and Q-vector divergence at 500-400 hPa layer, and the shallow and medium subtropical folds found by Sprenger et al. often happen to be in higher levels and deprived of this strong frontogenetic forcing.

As seen in previous sections (3.1.2 and 3.1.3), WRF simulation output data and GFS analysis used in this study have significant higher resolution than the ECMWF analysis used by Sprenger et al. (2003). Thus, a similar geometrical algorithm has been used in the present work and is described in detail in the following lines.

3.3.2 Geometric Algorithm

For the purpose of the work presented in this dissertation, an objective method to search folding structures of the dynamical tropopause mechanically over the 10 years of WRF output data is required. After a meticulous research over the literature, an algorithm based on a purely geometric fold definition, just as Croci-Maspoli (2002) and Sprenger et al. (2003) proposed, was consider to be the best option taking into account the good vertical and horizontal grid resolution of the data available. Thus, the dynamical tropopause (taken as the 2 PVU isosurface) will present a folded structure when multiple tropopause crossings in the vertical can be found, making no assumptions on its dynamical origin. This idea has been the focus to build up an objective algorithm to detect folding structures from a 3D data set.

The algorithm consists in two parts: i) "air classification" and, the strictly speaking, ii) "folding search and characterization". If each 3D-grid point can be correctly classified into tropospheric (low PV) or stratospheric (high PV) air, then the presence of a fold can be easily identified just by looking for multiple and consecutive changes between tropospheric and stratospheric air in a vertical column. However, PV can present at times a troposphere complex structure as can be seen in the work by Bithell et al. (1999) where, for instance, a high-pv tube-like structure found in low tropospheric levels merges with a subsiding tropopause folding. Thus, the difficult part is to sort correctly every grid point, designing an algorithm that unambiguously

discern between tropospheric and stratospheric air.

i) Air Classification:

First of all, each grid point must be classified into tropospheric or stratospheric air in a simply potential vorticity point of view. After computing potential vorticity at each 3D-grid point, the algorithm labels each point considering, as a first approach, tropospheric air parcels those with a potential vorticity value lower than 2 PVU (Label 1), and stratospheric air parcels otherwise (Label 2).

At this point, most likely some air parcels will be wrong classified due to high potential vorticity values present in tropospheric regions affected by friction or diabatic processes. Similarly, that can happen in the opposite way and it is possible to find bubbles of tropospheric air into the stratosphere. All these situations should be classified differently - and here is when arise the major difficulties - in order to avoid be confused as tropopause foldings when the second part of the algorithm ("folding search") is applied. See sketch in figure 3.3 for clarification.

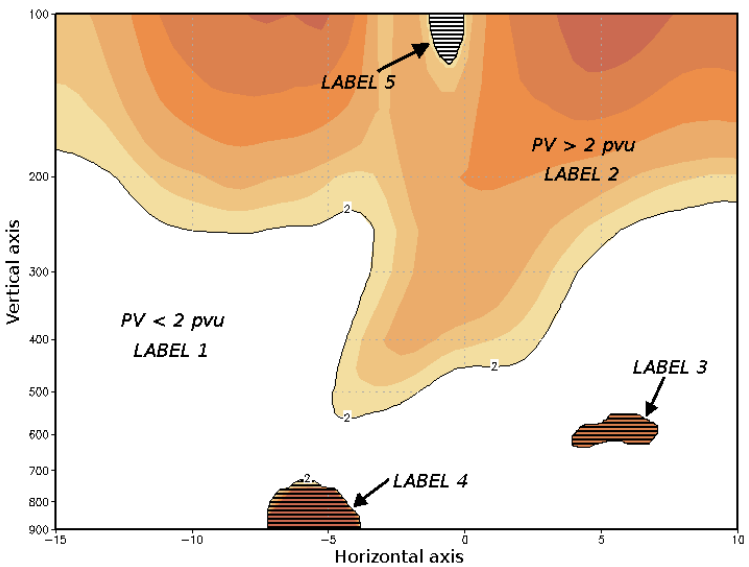

Figure 3.3: *Illustration of a tropopause fold PV cross section (longitud-pressure) showing the 5 different labels the algorithm sorts out.*

Let's focus first in changing the Label 1 coming from bubbles of tropospheric air into the stratosphere. To do that, the algorithm first looks for the bottom and the upper "tropopause" levels. That is, it creates a pair of 2D arrays, one with the first k-level where the first Label 2 is found searching from bottom to top in the vertical dimension and the other one, now starting the search from above and going down, the first k-level with Label 2 that has a Label 1 point just below. That way, all the

problems will focus there where the two arrays differ and additional searching out of those places can be avoid.

The algorithm then proceeds tagging with a cross mark (let's say Cross 1) all the points Label 1 located in between the two "tropopause" arrays. Afterwards, it tags with a Cross 2 all points Label 1 that have not been tagged as Cross 1 before (for being outside the two "tropopauses") and are neighbours[2] of a Cross 1. That means that these points first tagged with a Cross 1 have neighbours with Label 1 outside the two "tropopause" boundaries, then these points are not bubbles into the stratosphere but actually tropospheric air points. At this stage, a "neighbour searching algorithm" has been used to change, with a loop help, all Cross 1 tags next to any Cross 2 tag to also Cross 2 tags. In the end, the only Cross 1 tags still present will be the ones coming from a real tropospheric bubble into the stratosphere surrounded by Labels 2. Then, it is easy to change all Label 1 points tagged with a Cross 1 to Label 5.

The next step is changing Label 2 (stratospheric air) to Label 4 of all the points in contact with the surface, considering that these high PV values are caused by surface friction or moist diabatic processes. Unfortunately, seldom surface bubbles can mix with real tropopause foldings going deep inside the troposphere and it is necessary to find a way to unambiguously distinguish between surface-bubble PV anomalies and stratospheric intrusions. To do so, the specific humidity field is used discriminating both cases with a chosen threshold value of $q = 0.1 g kg^{-1}$. Low humidity values ensure the stratospheric air origin and the chosen threshold value is the same used by Croci-Maspoli and Sprenger et al. in their work. Then, the procedure taken here is changing directly the points Label 2 adjacent to the surface – first vertical level – to Label 4 and thereupon, changing every Label 2 in contiguous vertical levels neighbouring a Label 4 provided that it satisfies the specific humidity criterion.

So far, only the 2 PVU bubbles into the troposphere, not connected with the stratosphere, remain to identify. To change these Label 2 points the algorithm proceeds as previously. It computes again the new bottom and top "tropopause" arrays that now, will not be altered by the bubbles into the stratosphere (already converted to Label 5) nor the surface bubbles (converted to Label 4). So now, in between the two "tropopauses" one can only find folding structures connected to the stratosphere and isolated high-PV bubbles into the troposphere. These isolated bubbles can have a tropospheric origin generated by diabatic processes or an stratospheric origin coming from tropopause foldings or other stratospheric intrusion processes. The algorithm could easily made use of the specific humidity criterion to identify the bubbles origin but in that case, all of them will be removed from the tropopause fold

[2]Hereafter, "neighbour points" means "points next to" in the 3D grid considering all directions, also diagonally.

counting reasoning that if one of those bubbles is detached from an older tropopause fold it is not consider any more an active fold but just a remaining consequence. So, they are sorted out by tagging with crosses as done before (when distinguishing Label 5) and then using the "neighbour searching" technique to discriminate if the tagged areas are connected to the stratosphere or, otherwise, closed bubbles. Once identified, the latter previously marked as Label 2 can be easily changed to Label 3.

At this point, the labeling is almost completed and all grid points Label 2 in between the two "tropopause" arrays are connected to the stratosphere though one final point needs to be considered. One last application of the specific humidity criterion is necessary to discriminate possible tropospheric high-PV regions generated by diabatic processes merging with stratopheric intrusions, those that are not connected with the surface and already classified as Label 4. In such a case, these regions of high PV and high specific humidity are again detached from the labeled 2 stratosphere using Label 4. Finally, the total labeling is completed and each air PV class unambiguously identified, thus the algorithm can proceed with the second part based on tropopause fold searching and characterization.

ii) Fold Searching and Characterization:

This second part of the algorithm involves the detection and location of tropopause fold regions by looking point by point for multiple vertical crossings of the "dynamical tropopause", that is the 2 PVU surface. Since every 3D-grid point is already labeled depending on its PV nature, the algorithm simple searches in the vertical, from bottom to top, for multiple label changes. That way, a fold is counted in a 2D-grid point if it is found a change from Label 1 (or Label 4[3]) to Label 2, then another change from Label 2 to Label 1, and a last change from Label 1 to Label 2 (see figures 3.3 and 3.4).

When a fold is found, the algorithm also computes and registers different geometric fold features that are useful to its characterization and further classification. This parameters, shown schematically in figure 3.4, are:

- **Gap:** pressure difference (in hPa) in between points 2 and 3 in figure 3.4.
- **Depth:** maximum pressure achieved for the fold intrusion into the troposphere (point 1 in figure 3.4).
- **Thickness:** pressure difference (in hPa) in between points 1 and 2 in figure 3.4.
- **Zonal Width:** maximum distance (in km) on the zonal direction of the fold

[3]A reminder that Label 4 has been used to denote high-PV tropospheric air that can merge with stratopheric intrusions. Thus, it is possible to find a Label 4 just below a Label 2 related to a tropopause fold.

projection on the horizontal plane.

- **Meridional Width:** maximum distance (in km) on the meridional direction of the fold projection on the horizontal plane.

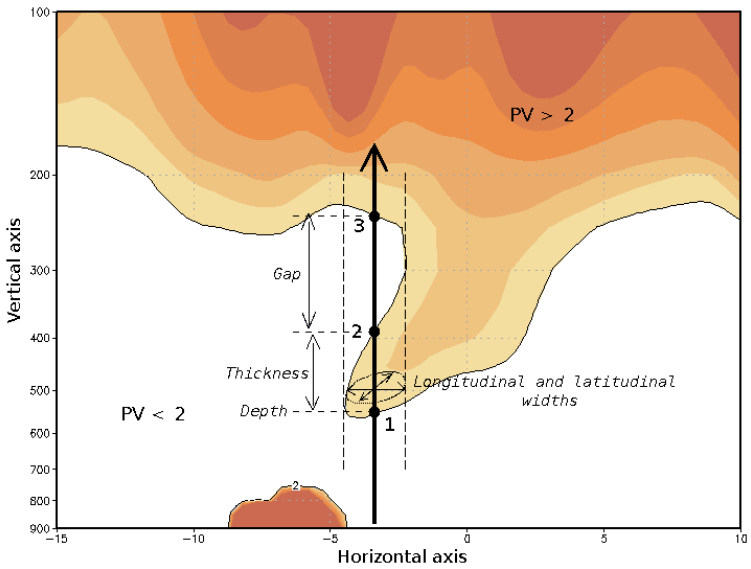

Figure 3.4: *Illustration of a tropopause fold PV cross section (longitud-pressure) showing the searching folding process and the different fold characterization parameters.*

The algorithm also classifies the fold depending on its pressure gap value in the same way as in the work presented by Sprenger et al.. So, if the pressure gap is greater than 350 hPa the fold is classified as a deep fold, if the gap is in between 200 hPa and 350 hPa the fold is named a medium fold, and a gap lower than 200 hPa but greater than 50 hPa yields folds called shallow folds. If the pressure gap is less than 50 hPa the structure is not regarded as a fold but as an small undulation and it is omitted and not counted.

3.4 Remarks on the Model Setup

Some concerns arised at the time of choosing for the more suitable WRF model configuration. This section will discuss the three different questions that generated more doubts and it will justify the options eventually chosen. Firstly, an evaluation of the analysis nudging method versus a daily reinitialization approach is presented. Secondly, some caveats concerning the model domain and related to boundary condition problems are given. Finally, the shorwave radiation parameterization option is discussed.

3.4.1 Analysis Nudging versus the Reinitialization Mode

As mentioned previously in section 3.1.2, the possibility of using analysis nudging to complete the 10-year WRF mesoescale simulations was examined. The Nudging is a technique that periodically relaxes the regional model intermediate solutions for the different atmospheric fields towards the global model solution (the mother data). This forcing takes place throughout the whole domain and at all vertical levels and avoids undesirable too much drift of the regional model making possible long continuous runs that would introduce two significant benefits: i) save computational resources avoiding overlapping time numerical simulations which are necessary between consecutive reinitializations because of the spin-up time requiered, and ii) produce constant and continuous long simulations without leaps within a sequence of images. However, nudging can force too much the solution toward the mother synoptic scale and that can be an inconvenient if the purpose is not only an scale refinement but also to generate regional tropopause details and to examine the capability of the WRF model to develope tropopause foldings. In such a case, the other option to limit the drift and to allow the model freely develop atmospheric mesoscale structures is to use periodic reinitializations, accepting both inconvenients in computational resources and continuity mentioned above.

To examine the most suitable option for the purposes of the present study, a whole month (December 2008) was tested with analysis nudging and compared with daily reinitializations. A couple of cases of tropopause fold events, one on the 2nd December 2008 and another on the 15th which develops in a cut-off low, are shown here. Besides, the first tropopause folding case was also analyzed with different simulations starting at different times in order to examine the tropopause folding development at different forecasting times (discussed later).

The fisrt case is analyzed in figure 3.5, which shows pressure tropopause maps of a 24-hour sequence (from 1st December 2008 at 18Z to 2nd December 2008 at 18Z) of a tropopause subsidence and its growth differences between the WRF analysis nudging option (2nd column) and the daily reinitialization option (3rd column). In addition, the mother reanalysis data (JRA) are plotted in the first column for comparison. Shaded in colours is plot the pressure field on the 2 PVU surface (searched from below) which depicts the topography of this layer. The contours belong to the 300 hPa winds (black) and the 300 hPa potential temperature (red), and the bold black contour highlights the 300 hPa on the 2 PVU surface. An anomaly of the dynamical tropopause topography (blue colours) growing and going below the 400 hPa is observed. Comparing the WRF analysis nudging case (2nd column) with the JRA fields (1st column), a similar evolution can be noticed with a higher refinement of the topography structures in the 2nd column. Also, an slightly higher anomaly is shown by the WRF analysis nudging images at the end of the sequence. On

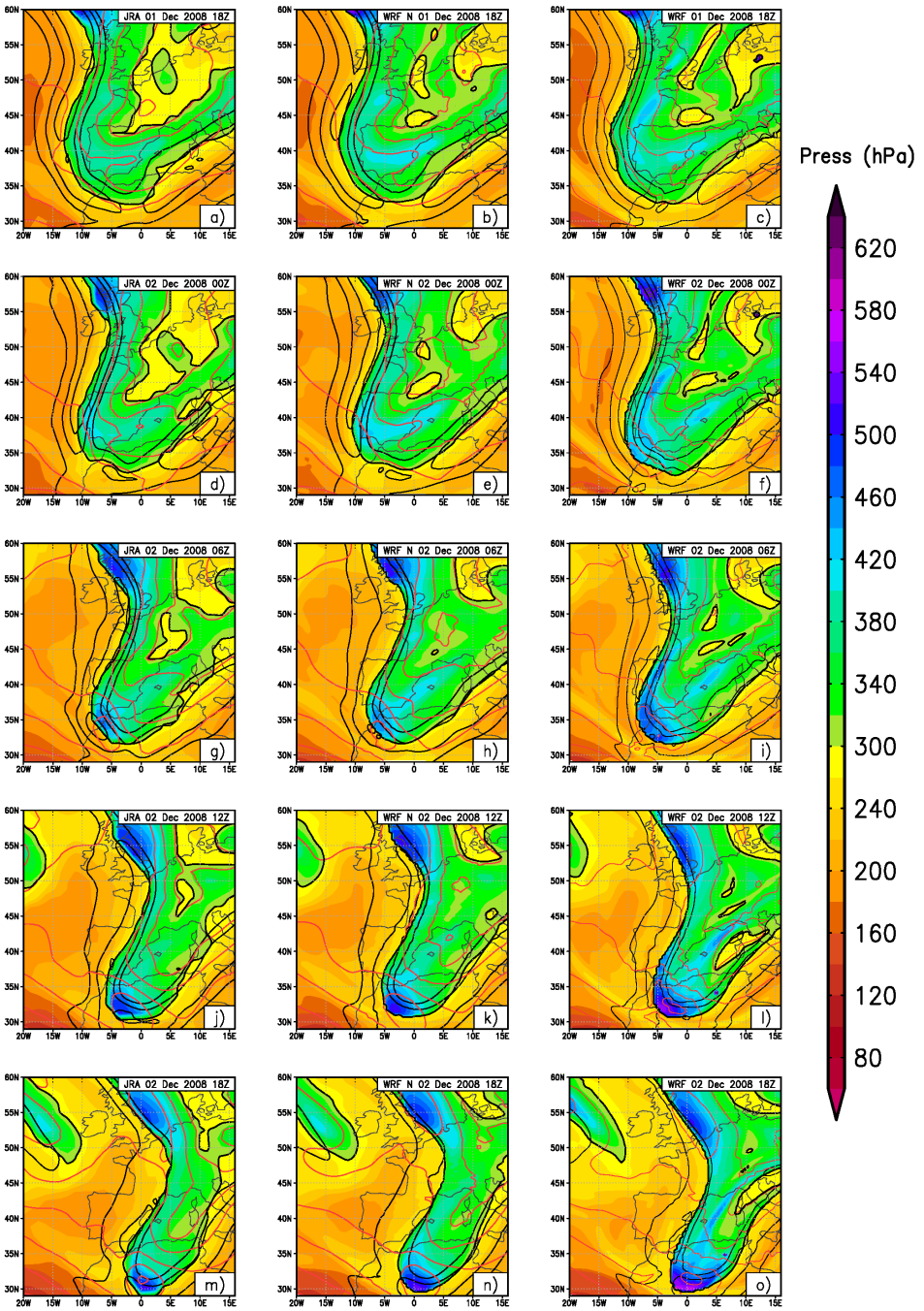

Figure 3.5: *Pressure field at the 2 PVU surface of a tropopause fold event. From top to bottom, 6-hourly images from the 1st December 2008 at 18 UTC to the 2nd December 2008 at 18 UTC for the JRA (1st column), WRF analysis nudging option (2nd column) and WRF reinitialization (initialized the 1st Decembre at 12 UTC) option (3rd column). Red contours: potential temperature at 300 hPa (5 K interval). Black contours: 40, 50 and 60 m/s horizontal wind field at 300 hPa. Bold black contour: 300 hPa intersection.*

the other hand, although images on the 3rd column (WRF reinitialization option) follow a similar evolution to that of the 2nd column, they show little differences and interesting features. Particularly, the anomaly located on the wave trough shows a significant subsidence increase reaching pressure values below the 550 hPa at 12 and 18 UTC on 2nd December, 2008 (last two images of the 3rd column). In addition, other small and interesting features develope along the trough axis under these conditions.

The second example is shown in figure 3.6. A complete 36-hour WRF run starting on the 14th December 2008 at 12 UTC (1st raw) and finishing on the 16th at 00 UTC (last raw) is shown in the 3rd column. As in figure 3.5, 1st and 2nd columns state for the JRA and the WRF analysis nudging case respectively. The sequence shows the tip of a tropopause trough on December 14th that cuts off by 15th December at 06 UTC. Again, the WRF analysis nudging case reflects no significant differences with the JRA fields, while the WRF simulation clearly develops higher intensity structures reaching the 600 hPa level just after 12 hours forecast on December 15th at 00 UTC, coinciding with the initial formation of the cut-off. Moreover, WRF forcing is also able to simulate the decay of the weather system. By the end of the simulation (15th at 18 UTC and 16th at 00 UTC, last two images), the dynamical tropopause maximum pressure values relax again to similar values of those on the JRA data and the WRF analysis nudging case.

Therefore, analysis nudging forcing clearly inhibits structure developments pushing the meteorological fields to resemble the global ones, in that case the JRA fields which have not enough vertical and horizontal resolutions to perceive the real extent of tropopause fold structures. Consequently, the standard WRF forecast mode seems to be the most appropiate way to perform the 10 year mesoescale simulations. However, to ensure these subsinoptic stronger anomalies shown by WRF simulations are more real than the synoptic scene the JRA depicts, the WRF reinitialization case from figure 3.5 is compared with the GFS analyses in figure 3.7, 2nd and 1st columns respectively. The GFS analyses (1st column) highlight strong tropopapuse pressure anomalies. In particular, the subsidence located on the wave trough, deepening below the 550 hPa, shows a good agreement whit that predicted by WRF (2nd column).

In addition, with the aim of answering the question of which is the most appropiated run length for each individual simulation, two other WRF runs, covering the same tropopause fold event but initialized at diferent times, are plotted in columns 3 and 4 in figure 3.7. Therefore, while the 2nd column displays the output fields of the simulation initialized on the 1st December at 12 UTC (just 6 hours before the first plot of the sequence), the plots in the 3rd column come from a simulation started 24 hours earlier (on the 30th November at 12 UTC) and the ones in the

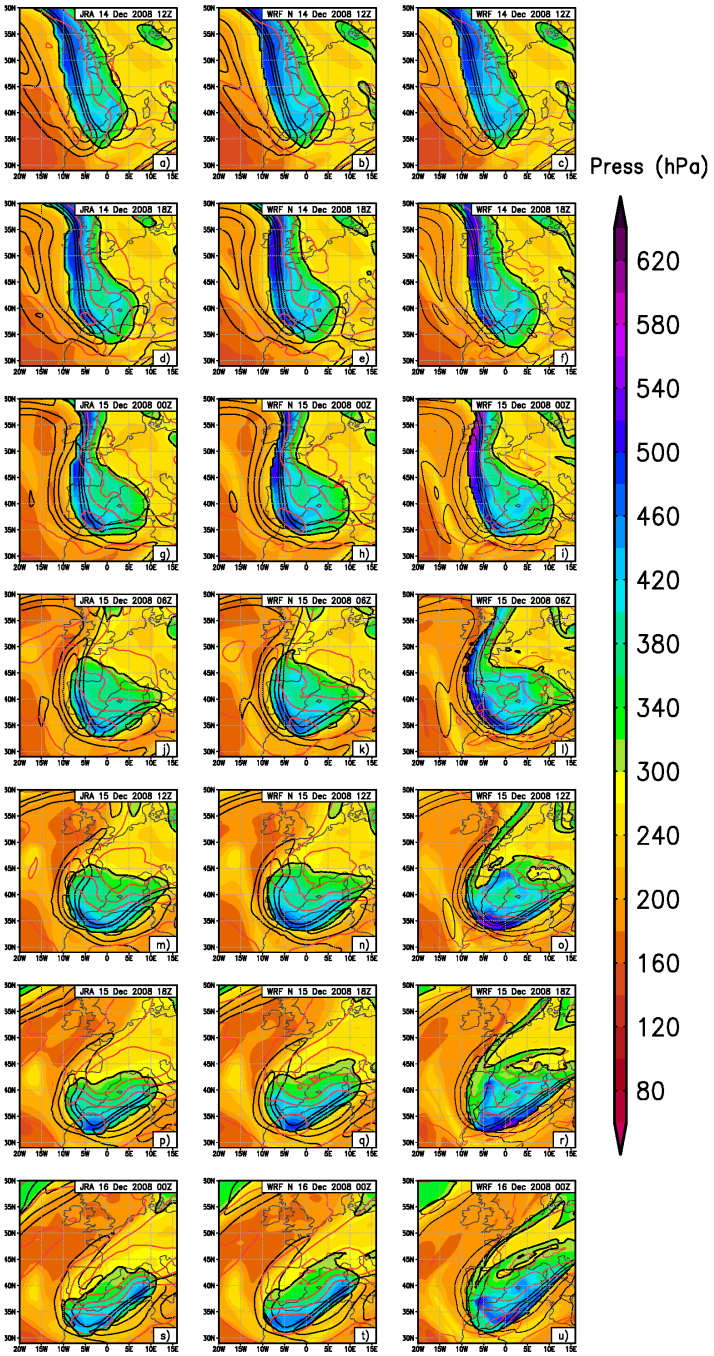

Figure 3.6: *Same as figure 3.5 for another event starting on the 14th December 2008 at 12 UTC to the 16th December 2008 at 00 UTC.*

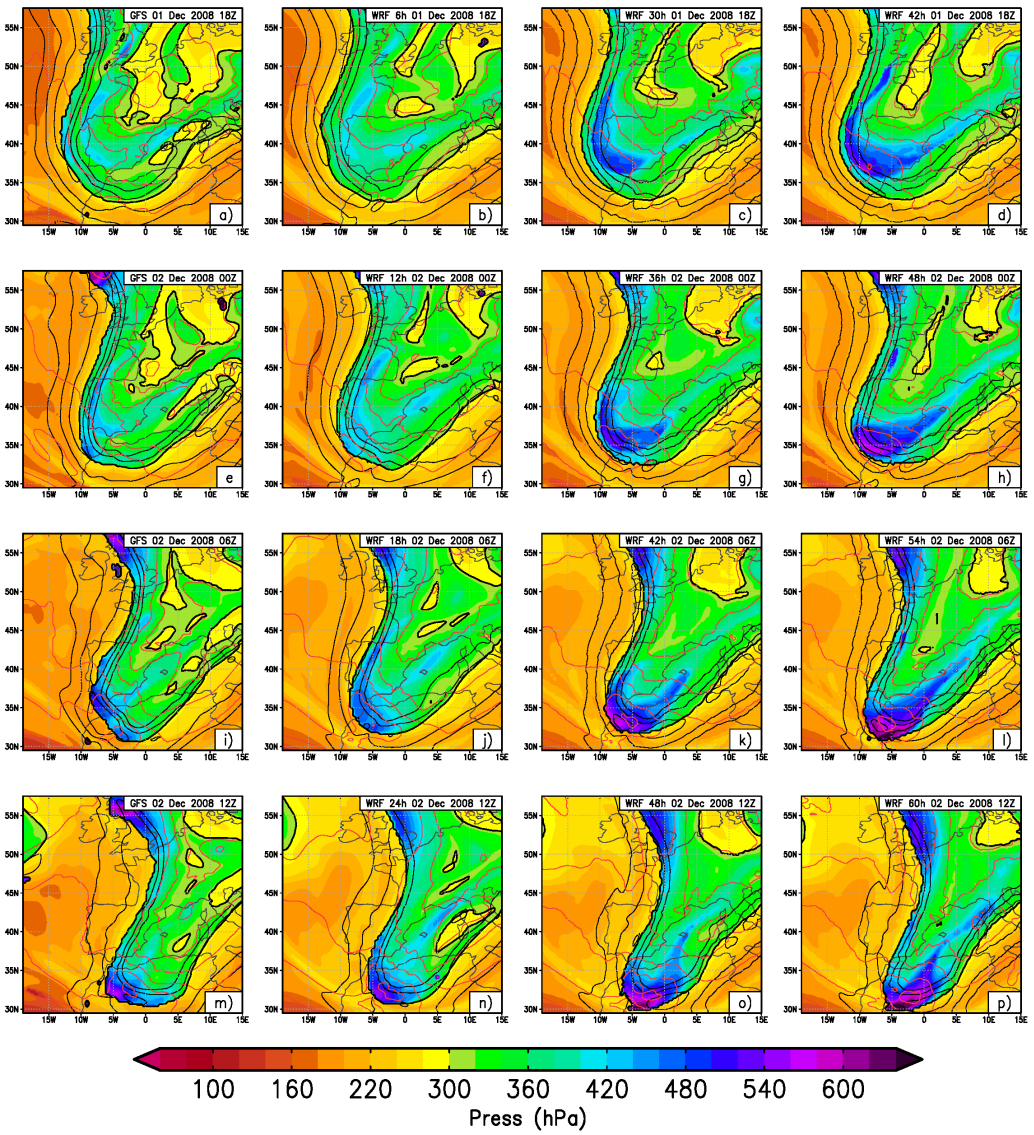

Figure 3.7: *Same as figure 3.5 for GFS analyses (1st column) and different WRF simulations initialized on the 1st December 2008 at 12 UTC (2nd column), on the 30th November 2008 at 12 UTC (3rd column) and on the 30th December 2008 at 00 UTC (4th column)*

4th column, from a simulation initialized 36 hours earlier (on the 30th November at 00 UTC). Examining the first raw, images c) and d) show, after 30 and 42 hours forecast respectively, more structure than the GFS analysis (a) or the 6-hour forecast WRF forcing (b). The same can be observed at the successive time instances and it points out that longer forecasting times allow WRF forcing to strengthen

tropopause structures. However, considering the last two raws and focusing on the southern anomaly, images on the 3rd and 4th columns (after more than 42 hours forecast) show a huge tropopause height anomaly, much greater than that shown by the GFS analisis and, additionally, remarkably misplaced. It appears, therefore, that after excessive time forecast WRF output fields can suffer from too much drift and some limit may be adopted. Accordingly, as detailed in section 3.1.2, the best option considered was to initialized the WRF model every day along the 10 years, running each simulation unconstrained (except for the domain boundaries) during 36 hours.

As a final remark, figure 3.7 shows as WRF (2nd column) is able to develop reasonably well the southern anomaly of the wave trough, reaching similar maximum pressure values as those shown by the GFS analysis (1st column). In contrast, GFS images display also an strong anomaly entering the domain from the North on the 2nd December at 00 UTC that grows up considerably along the subsequent times and that is not captured as intense by the WRF model, nor even after longer times forecast (columns 3 and 4). The simulations shown in these exemples were run with an smaller model domain configuration of that finally settled and detailed in section 3.1.2 (see figure 3.1). Most likely, the shallower subsidence on the northern anticyclonic flow displayed by the WRF outputs is a consequence of a too small model domain. By that reason, at the time of the model initialization the anomaly is outside of the boundaries of the model and it enters the domain at a later time through the boundary condition forcing. If the incoming is too rapid the model can suffer from a lack of information and it can be unable to capture the entire extent of the synoptic situation. This is known as one of the weaknesses of limited area models and it is further discussed in the next upcoming point.

3.4.2 Caveats of the Model Domain

Initially, the regional study was plan over an area which covered only the south-westernmost part of Europe and thus the WRF mesoscale simulations were started with an smaller domain model configuration such as that in figure 3.8 (left). One of the intentions of using an smaller domain was partly to save computational resources in order to hold the possibility of extending the simulations up to 30 years and to build a more robust regional climatology. However, the first results revealed that a larger domain was needed and that the computational expense had to be accepted.

On the one hand, as speculated in section above, the poor temporal resolution of the mother data compared to the timescales of strong weather systems entering the domain at a later initialization time have the potential of poorly resolving the evolving weather structures and thus degrading the quality of the solution (Warner et al.

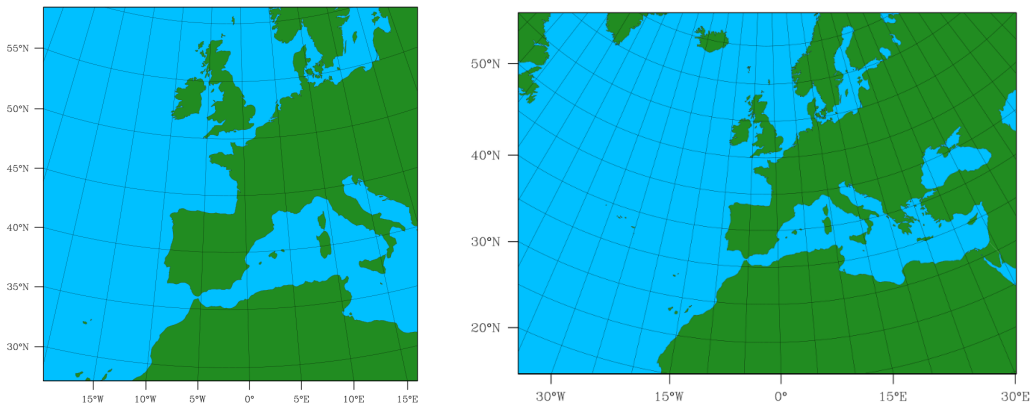

Figure 3.8: *Initial WRF model domain configuration (left) and definitive WRF model domain configuration (right)*

1997). The boundaries are forced to the mother data every 6-hours, enough time for too rapid anomalies to partially skip the boundary forcing. This deficiency on synoptic and mesoescale structures is especially important in the upper-troposphere and definitely observed on tropopause fold events. Figure 3.9 compares the tropopause fold frequency of ocurrence for the four season from one year of WRF simulations run with the big domain (3.9a) and the small domain (3.9b). The deficit on tropopause fold structures can be clearly recognized over the regions A, B, C and D on figure 3.9b, precisely next to the boundaries where meteorological features may be mainly entering the domain considering the typical extratropical westerly flow.

On the other hand, the differences and interactions between the limited area model solution and the coarser-resolution model providing the lateral boundary conditions (in this case the WRF solution and the JRA) can generate gravity-inertia waves and numerical artifacts at the lateral boundaries that can contaminate the domain interiors (Warner et al. 1997). These computational boundary errors are also well visible in figure 3.9b over the regions E, F, G and H where spurious strong tropopause fold frequencies are displayed, precisely coinciding and neighboring areas where significant tropopause fold activity is present at the boundaries which may amplify the numerical boundary errors.

The distancing of the lateral boundaries sufficiently far from the area of meteorological interest is the only possible solution to these problems (Warner et al. 1997). Consequently, even if the increase of the model domain entails an important increase in computational time, the expense is necessary.

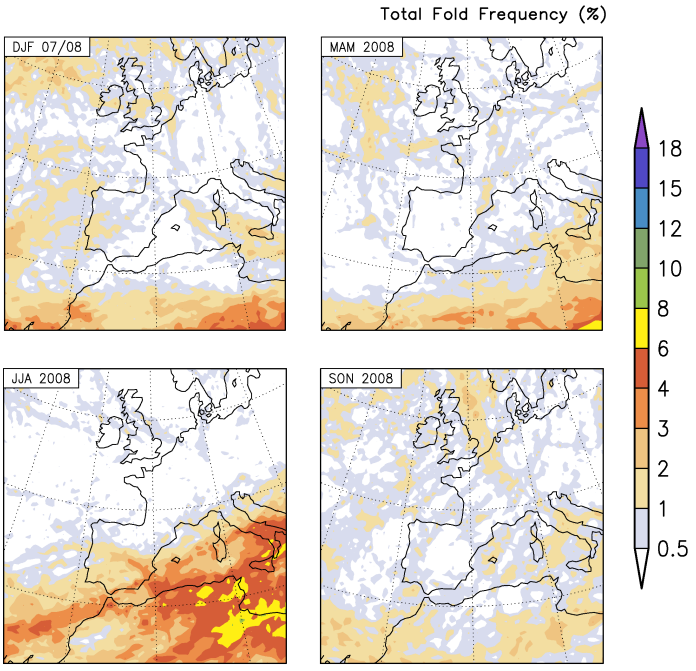

(a) From simulations with the big domain (fig.3.8, right)

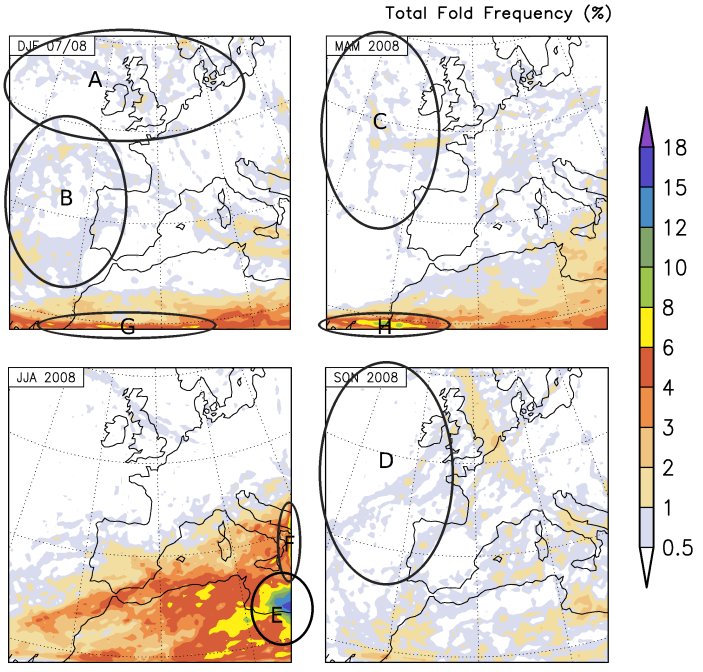

(b) From simulations with the small domain (fig.3.8, left)

Figure 3.9: *Tropopause fold frequency (in %) for winter (DJF), spring (MAM), summer (JJA) and autumn (SON) from one year (Dec 2007-Nov 2008) of WRF simulations performed with the big domain (a) and the small domain (b).*

3.4.3 Shortwave Radiation Parameterization

As previously noticed in section 3.1.2, the shortwave radiation parameterization used in the WRF simulations is the Dudhia scheme (Dudhia, 1989), which is the simplest option of the WRF model and does not take any consideration to the ozone absorption. However, ozone absorption may become important above 50 hPa. Thus, three months were tested with the New Goddard scheme and compared with the Dudhia parameterization option. The New Goddard shortwave parameterization (Chou and Suarez 1999; Chou et al. 2001), included in WRF version 3.3, discretizes the solar spectrum in eleven bands of absoption, seven of which are in the ultraviolet, and it uses available datasets to force simplified ozone distributions in the atmosphere. In particular, it uses five different ozone profiles: tropics, midlatitudes in summer, midlatitudes in winter, polar regions in summer and polar regions in winter.

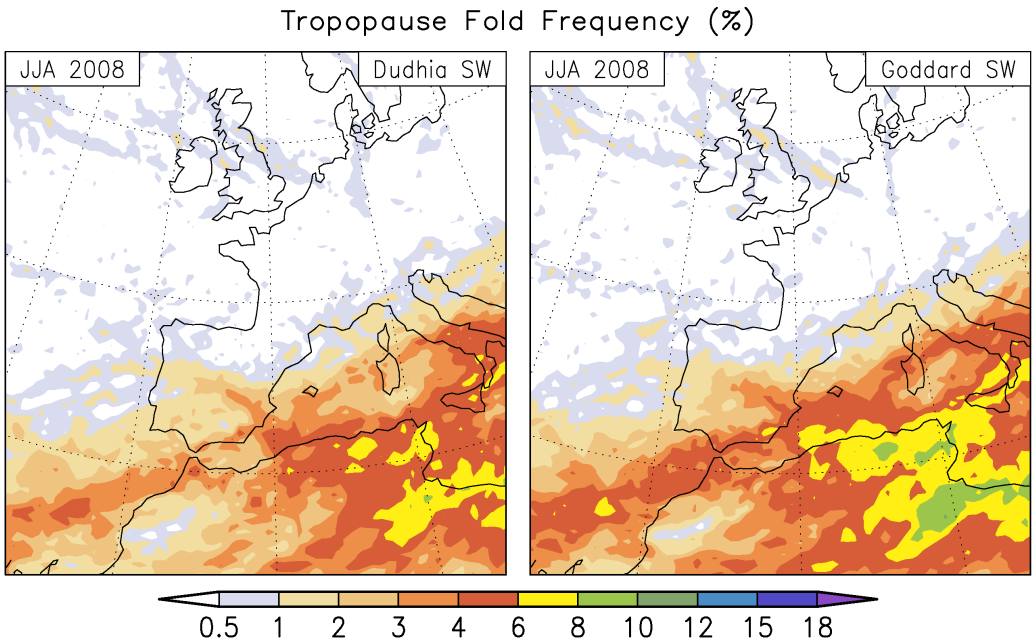

Figure 3.10: *Tropopause fold frequency (in %) for summer (JJA) 2008 from WRF simulations performed with the Dudhia shortwave radiation scheme (left) and the New Goddard radiation scheme (right).*

Figure 3.10 compares tropopause fold frequencies for the summer (JJA) 2008 between WRF simulations using the Dudhia (left) and the New Goddard (right) shortwave radiation schemes. It can be observed that these frequencies are slightly higher considering ozone absorption (right), with differences that range from 1% to 2% and with some peaks that reach a 3% of discrepancy around the coast of North Africa. Although the increase is interesting, this is not mainly due to an increment

of the number of individual tropopause fold events but rather to a bigger growth and extension in time of them, which can yield to more grid points being affected by a double tropoause structure and then counted in the final amount of tropopause fold ocurrencies. Moreover, the general tropopause fold frequency distribution is not change. Besides, the New Goddard scheme tends to slightly overestimate the total ozone column during summer (JJA) over the region of study (Montornès et al., 2014), which may also cause an slightly overestimation of its effect on tropopause fold development. Considering all these and the fact that the use of the New Goddard scheme, as well as the other more complex shortwave parameterizations, consumes more than double on computational resources, the final dicision was to employ the simple Dudhia parameterization although its limitations.

Chapter 4

Global 1-Year GFS Tropopause Fold Analysis

In this chapter, a global Tropopause Fold investigation using 1-year (December 2007 to November 2008) of GFS analysis data is presented. As it has been described earlier in chapter 3, the GFS T382 analyses cover the entire world with similar horizontal and vertical resolutions to that obtained with the WRF model, with two additional benefits: the avoidance of the boundary condition problems associated with limited area models (LAMs) and the incorporation of assimilated observational data. Therefore, this one-year of GFS results serves as a good WRF climatology validation and it offers a global picture of Tropopause Fold (TF) distribution and preferred regions of formation over the northern and southern hemispheres. First in this chapter, a worldwide analysis of one year TF frequency is presented. Afterwards, different TF characteristics and their geographic distributions are thoroughly examined.

4.1 Geographical Distribution and Seasonal Variability

An objective and geometric fold searching algorithm (detailed in chapter 3, section 3.3) has been applied at every 6-hour GFS analysis fields for an entire year of data. At every time and at each grid point that the algorithm recognizes a 2 PVU folded surface, it counts a TF ocurrence and it records other associated TF characteristics such as intensity of the fold, depth of the intrusion, thickness and horizontal extension. The percentage of time instances where a fold has been identified at a certain location during the considered season represents the fold frequency at that certain location. The result is shown in Figure 4.1, which displays the total tropopause fold frequency distribution for both hemispheres and for the 4 seasons: December 2007

to February 2008 (DJF, figure 4.1a), March-May 2008 (MAM, 4.1c), June-August 2008 (JJA, 4.1b) and September-November 2008 (SON, 4.1d). The preferred regions of tropopause fold formation are found over the subtropics in both hemispheres and in all 4 seasons, but the activity is higher and more extended in the winter hemispheres. In the extratropics, tropopause fold frequencies are lower and the major activity is aswell mainly detected in the winter hemispheres. In a thoroughly examination, however, there are significant zonal differences between hemispheres and seasons and some symmetries.

In general terms, the boreal winter (DJF) and boreal summer (JJA) climatologies agree really well with the work of Sprenger et al. (2003), who presented also a one-year TF study using a similar geometric TF identification algorithm based on 1° horizontal reslution ECMWF analyses for the time period March 2000 to February 2001. However, slightly higher frequencies and some zonal differences can be distinguished, likely due to, on the one hand, the higher resolution of the data used in this work and, on the other hand, the typical year to year variability.

4.1.1 The Subtropics

In the northern hemisphere winter (DJF season) tropopuase fold activity forms a more or less continuos subtropical belt only partially interrupted by relatively lower TF frequencies in the Middle and East Pacific and in the East Atlantic coast. High frequency values (15-25%) extend from West Africa to the West Pacific Ocean with maximum values over China (30%). These maximum values are precisely located along the jet axis with the maximum peaks positioned on the west side of the jet maximas, (that is over the areas where the mean winds are under maximum accerelation conditions). The marked discontinuities ranging from Middle Pacific to East Atlantic are found over a region of zonal breaks of the climatological jet and the most outlined feature is the relative TF frequency maxima found in the Middle Atlantic (15-25%) where a significant climatological jet break is located. This region is a distinguished RWB gerneration area which suggests that both phenomena can have a closed relationship.

In the southern hemisphere winter (JJA months), the subtropical TF activity follows a similar pattern as in the northern hemisphere thought, in general, with lower values and a more uniform zonal distribution, simultaneously with a lower climatological jet intensity and a higher zonal jet symmetry. The exception to that is the region over the southern Indian Ocean, from South-Africa east coast to west Australia. This region shows significant high TF frequencies (15-20%), mirroring a high TF frequency band over the subtropical northern hemisphere summer. In the northen hemisphere summer, indeed, TF activity decreases notably everywhere with

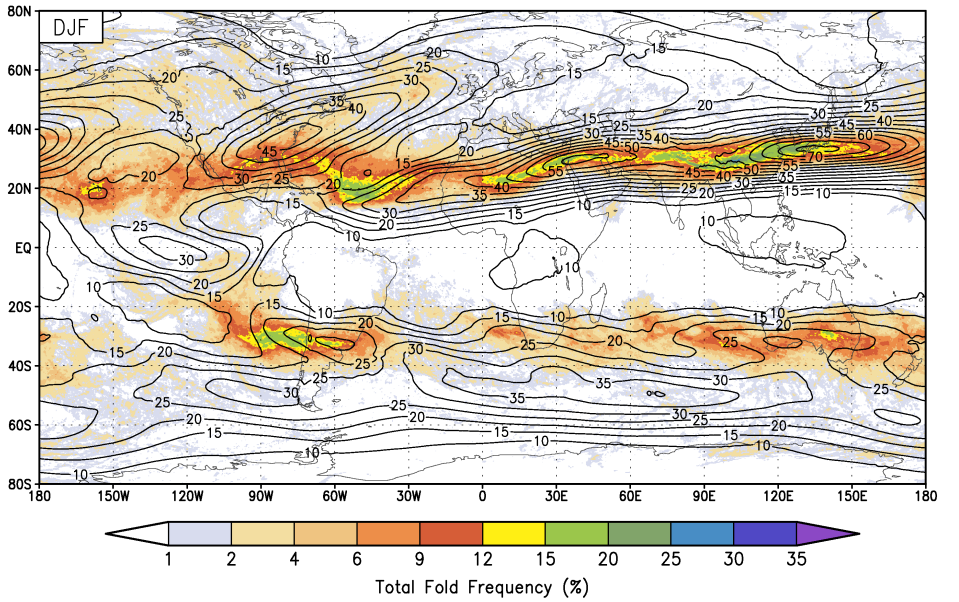

(a) DJF

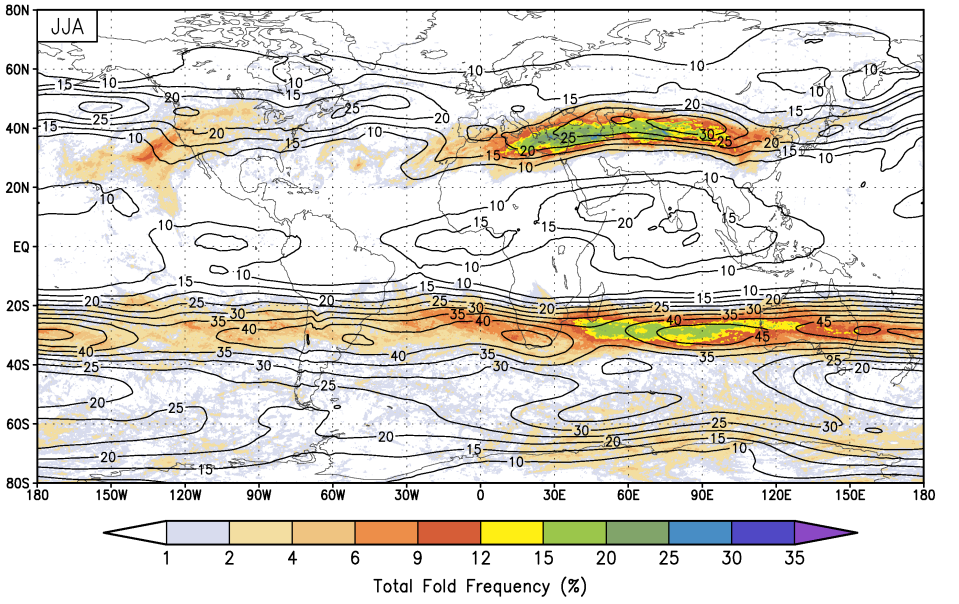

(b) JJA

Figure 4.1: *Seasonal mean spatial distribution of total fold frequency (in %) for a) winter (DJF), b) summer (JJA), c) spring (MAM) and d) autumn (SON), from one year of GFS analyisis data (Dec 2007 - Nov 2008). Contours of horizontal mean wind at 200 hPa are superimposed with a 5 ms^{-1} wind interval.*

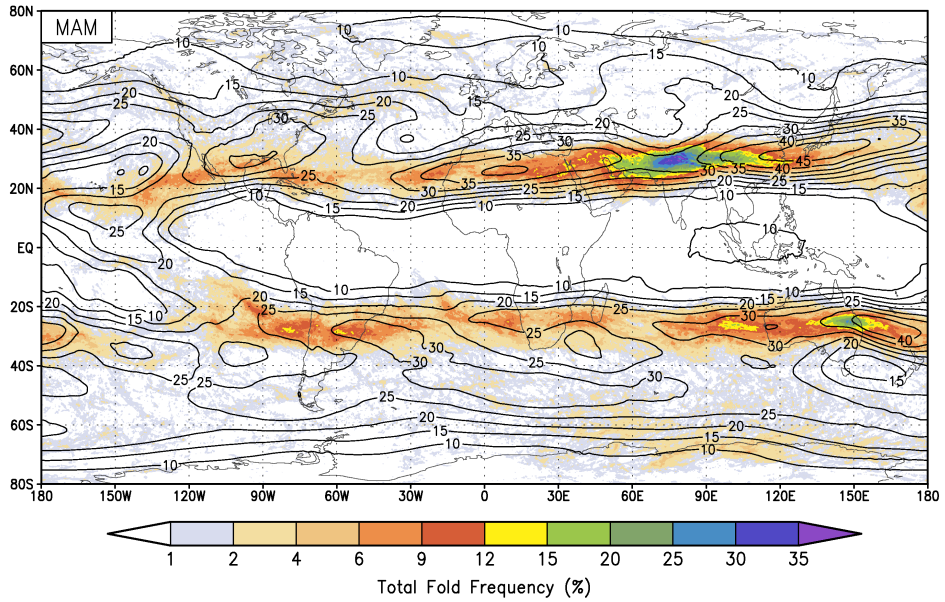

(c) MAM

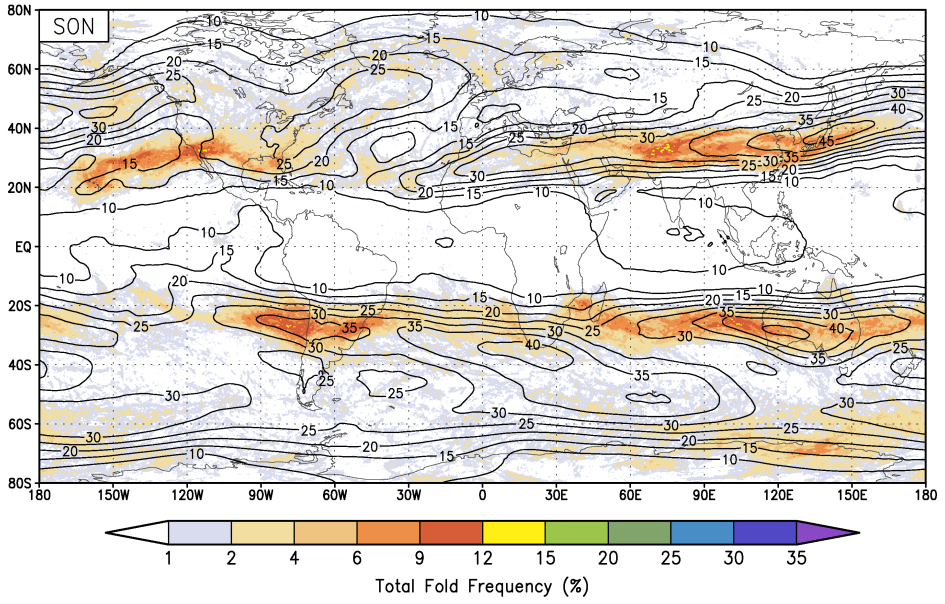

(d) SON

Figure 4.1: *Seasonal mean spatial distribution of total fold frequency (in %) for a) winter (DJF), b) summer (JJA), c) spring (MAM) and d) autumn (SON), from one year of GFS analyisis data (Dec 2007 - Nov 2008). Contours of horizontal mean wind at 200 hPa are superimposed with a 5 ms^{-1} wind interval.*

the exception of that band which extens from the Mediterranean along the northern edge of the Tibetan Plateau to the Yellow Sea and reach maximum frequency values up to 30%. That band coincides with the west and north flanks of the Asian Monsoon Anticyclone, an upper-level (∼200 hPa) closed circulation which helps to maintain the summer westerly jet at midlatitudes (Dunkerton 1995, Randel and Park 2006, Park et al. 2007). This anticyclonic upper-level circulation is established as a Gill-type Rossby-wave response which is due to convective heating forcing and it is also accompanied by a quasi-symmetrical, smaller amplitude anticyclone in the Southern Hemisphere [Gill 1980, Hoskins and Rodwell 1995, Highwood and Hoskins 1998, Park et al. 2007]. In the work of Highwood and Hoskins (1998) (fig. 9) an schematic diagram of the 3D structure of this circulation can be found. The southern flank of that mirror anticlyclone merges with the westerly winter jet of the Southern Hemisphere precisely where those high TF frequencies are found during austral winter. Another subtropical region with TF activity during boreal summer, though with less intensity and extension, is the North America West Coast where another monsoon circulation, though smaller, is found.

Looking at southern hemisphere summer patterns, the situation in the subtropics is quite similar to that of the northern summer. TF activity decreases significantly in respect to the winter situation, except on the regions with typical monsoon circulations. Noteworthy is the considerable increased observed over South America and the adjacent Pacific Ocean where the South America Monsoon System (SAMS) is taking place. High TF frequencies up to 15%-20% are observed over that region and a coupled response may also be responsible for a fraction of the enhanced TF activity observed in the Atlantic Ocean in the northern hemisphere subtropics.

Moving to figures of autumn and spring seasons (4.1c and 4.1d repectively), they show a sort of intermediate state between winter and summer patterns, a combination of large zonal distributions along the subtropical jet with located-intensified regions in the proximities of typical regional monsoon climates. During boreal spring TF activity is higher than during boreal autumn in both hemispheres, though in the Southern Hemisphere little difference is observed between both seasons. A prominent maximum up to 36% of TF frequency is located over north India during boreal spring. A monthly examination (not shown) reveals that TF activity during May is really high over the area, with frequency values up to 65% along the border between Pakistan and India, north India and extending to the westernmost part of China. These high values indicate that TF are almost permanent features in that area during May, when typically occurs the onset of the Asia Monsoon over the Bay of Bengal and the South China Sea (Wu and Zhang 1998, and references thereby). The promiment orography of the Tibetan Plateau could also play an important role on the generation of such permanent features.

Since Tropopause Fold formation in the subtropics is quite influenced by monsoon circulations, further discussion on that issue is given below.

4.1.2 TF and Monsoon Circulations

In paragraphs above, it has been seen that tropopause fold formation in the subtropics is mainly associated to subtropical jet streams. Accordingly, high frequencies are found in the winter hemispheres along with strong jets and in the summer hemispheres in connexion to summer subtropical jets mantained by monsoon circulations. However, although local summer jets are quite weak compare to winter jets, TF activity is locally comparable in magnitude in both seasons. This suggests that upper-level monsoon circulations increase TF formation besides their roll in maintaining the subtropical zonal flow and its associated TF activity.

Figure 4.2 shows the monthly average geopotential height and horizontal wind anomalies at 150 hPa for July 2008 together with the location of the highest TF frequencies (freq. $> 12\%$) shaded in a black-white scale over the Asian Monsoon region. Geopotential heigh and wind anomalies show a mature upper-level anticyclone situated over the Asian continent. Considerable TF formation occurs on the western and northern flanks of the anticyclone. In the Southern Hemisphere, a quasi-symmetric, less intense and split in two parts anticyclonic circulation can also be recognized, simultaneously with high TF frequencies between both identified anticyclones and along the westerly southern flank, deep entering into the Autralian continent.

An analogous, though with less extended influence situation is found in the Southern Hemisphere summer over South America, driven in that case by the South American Monsoon System (SAMS). Likewise, an upper tropospheric anticyclone circulation is stablished by convection and latent heating over the tropical and subtropical South America, southwest of the region of most intense precipitation and convection and again consistent with the Gill (1980) tropical forcing response (Silva and Kousky 2012). Analogous images as that in Figure 4.2 for the SAMS case have been analysed (not shown) and high TF frequencies up to 15%-20% are observed on the west and south flanks of the upper-level anticyclone during austral summer. The other regions of the globe that show distinc monsoon characteristics in their summer seasons (US, northern Australia and Sub-Saharan Africa), although with less intensity and extension, show also significant signs of large TF activity (frequencies around 10%) on their west and poleward sides vicinities.

Moreover, as shown above, an intensification of TF activity is also present around the proximities of typical monsoon circulations during MAM and SON seasons, when typically meet the beginning and ending phases of monsoons. An example is

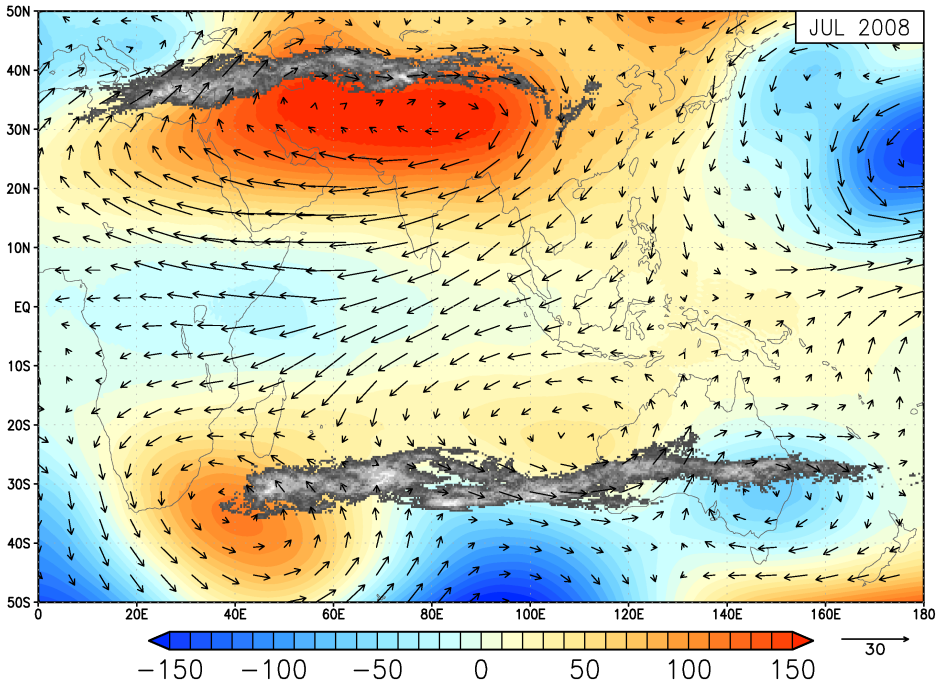

Figure 4.2: *Monthly mean (July 2008) geopotential height and horizontal wind anomalies (deviations from the zonal mean) at 150 hPa from GFS analysis data. Geopotential heigh aomalies are in meters and horizontal wind fields are shown as vectors (ms^{-1}). Large Tropopause Fold frequencies ($>$ 12%) are shaded in a black-white scale.*

the TF frequency maximum observed over India during boreal spring, particularly during May when typically occurs the onset of the Asia Monsoon. During early May, an upper-level anticyclone is stablished (Wu and Zhang 1998, fig. 9) with its poleward flow precisely located over that TF frequency maximum. In June and moving to the summer months, the anticyclone moves progressively to the west and to higher latitudes (as seen before in Figure 4.2) and in September, the monsoon starts its decaying phase and the anticyclone moves significantly eastwards agreeing well with the observed TF activity location during SON (Figure 4.1d). In October (not shown), the major TF frequencies (20%) are found in North China extending to the East China Sea and Japan. Another example can be found over the South America subtropics with TF frequencies around 10%-20% during SON and MAM when, respectively, beginning and ending phases of SAMS are taking place. Silva and Kousky (fig. 8) show as an upper-level anticyclone is already well-stablished on mid-October and still present on mid-April.

These high tropopause fold ocurrences in connexion with upper-level monsoon circulations are clear signatures of interaccions between the upper troposphere and

the lower stratosphere on those regions. Lately, most studies have been focused on the role of the Asian Monsoon in stratosphere-troposphere transport since it may account as a relevant mechanism of exchange between both layers and as an important source of water vapor for the stratosphere (Dunkerton 1995, Chen 1995, Dethof et al. 1999, Gettelman et al. 2004, Konopka et al. 2010, Randel et al. 2010, Bian et al. 2012). The proximity of the northern flank of the anticylcone to the tropopause break opens the possibility of irreversible mixing by quasi-horizontal adiabatic motion along isentropes. A monthly mean latitudinal-vertical cross section average through the latitudes of the asian monsoon anticyclone (10°E - 110°E) for July 2008 (figure 4.3) shows a monsoon anticyclonic circulation with a deep vertical structure and extension into the lower stratosphere, similarly as that shown in the work of Dunkerton (1995). In the upper troposphere, strong easterlies over the northern tropics - extending into the southern tropics - dominate the southern flank, and a subtropical westerly jet pushed well poleward of its winter position characterizes the northern flank. Its maximum coincides with the tropopause break in this sector which presents strong climatological PV gradients on the poleward side of the jet core corresponding to the transition zone from tropospheric to stratospheric air where sloping insentropes intersect the tropopause.

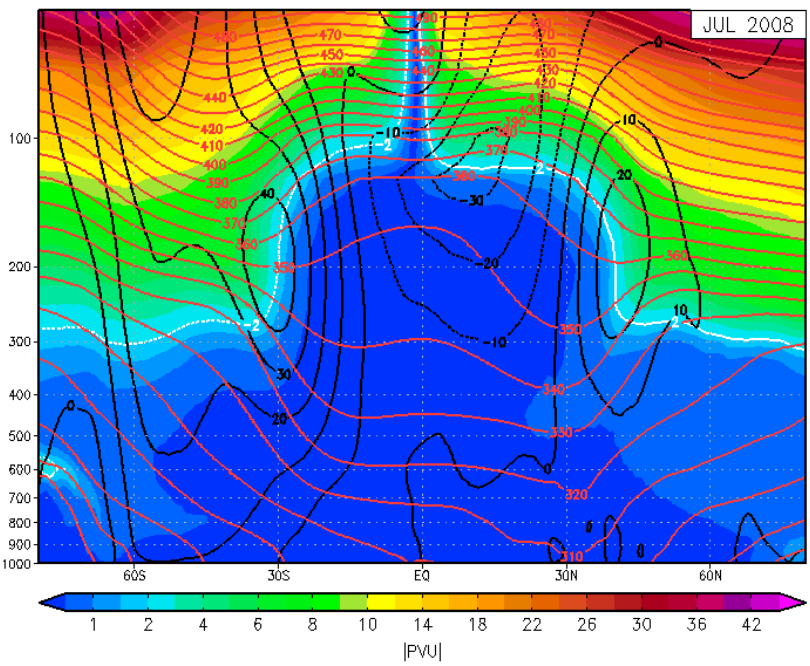

Figure 4.3: *Climatological vertical cross section of potential vorticity (PVU) for July 2008, average through the asian monsoon anticyclone latitudes* $(10° - 110°E)$*, from GFS analysis data. Mean zonal winds (black contours) and potential temperature (red contours) are superimposed.*

The strong PV gradients act as a dynamical barrier to meridional movements (Juckes and McIntyre 1987). However, Dunkerton suggested that local changes in the jet dynamics such as changes in their intensity or interactions with tropical or midlatitude synoptic disturbances, can lead to stratosphere-troposphere exchange, especially in northern summer when there is a relatively weak jet and PV gradients are smaller. Dethof et al. (1999) showed that adiabatic exchange along insetropic surfaces that intersect the tropopause can occur if the PV barrier is sufficiently distorted allowing more meridional displacement of air parcels. They found that two-way S/T exchange occurs when the dynamical tropopause is distorted by interactions of midlatitude synoptic-scale tropospheric cyclones with the northern branch of the upper-level monsoon anticyclone and they proposed these interactions as a regular mechanism for moistering the lower stratosphere. An scheme of that mechanism is illustrated in Dethof et al., figure 15.

In tropopause fold events, the 2 PVU surface misshapes and elongates beneath the horizontal wind maxima deforming the PV barrier, specially below and above the jet core which are typical regions of clear-air turbulence (Shapiro 1976 and Shapiro 1978). An example can be viewed in figure 4.4 (right) which shows a cross section during a tropopause fold event on the 19th July 2008 at 18 UTC over the eastern Mediterranean region. At the level of maximum wind (∼200 hPa) large horizontal PV gradients are observed, however, above and in particular below the jet core where wind shear is maximized and isentropes tild down along the tropopause intru-

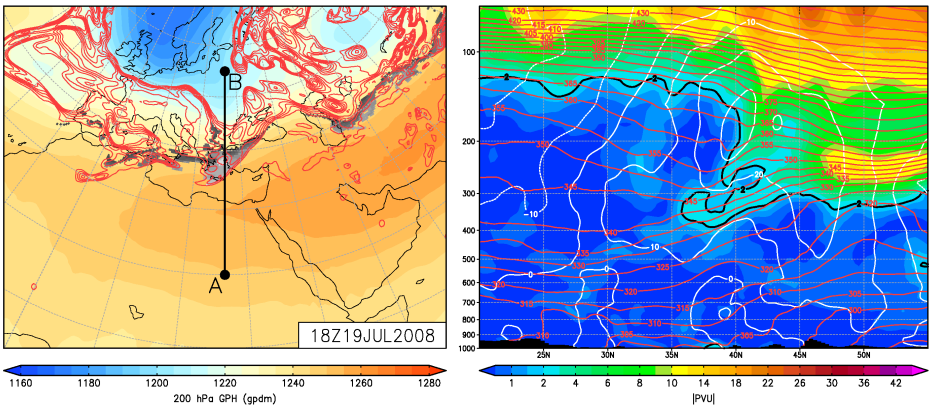

Figure 4.4: *Tropopause fold event on 19 July 2008 at 18 UTC over the eastern Mediterranean region. Left: geopotential height at 200 hPa and tropopause folded regions (white-black shaded regions). Red contours of 1.5, 2, 2.5, 3, 3.5 and 4 PVU on the 340 K isentropic surface are superimposed. Right: vertical cross section of potential vorticity (PVU) across the segment A-B (26.5°ircE) from left. Zonal winds (black contours) and potential temperature (red contours) are superimposed. From GFS analysis data.*

sion, isentropic PV gradient decreases and deformes (see PV contours on the 340 K surface shown in figure 4.4, left) and the barrier withers. The 200 hPa geopotential height field in figure 4.4 (left) displays a midlatitude synoptic disturbance propagating eastward that interacts with the westernmost part of the anticyclone northern branch near the 26°E. On the 340 K isentropic surface, the red PV contours show a baroclinic wave and a tongue of relatively high PV that extends equatorward to lower latitudes. Besides, grey shades indicate that a dynamical tropopause folded region accompanies the tip of the tongue. An examination during the subsequent days (not shown) reveals that 12 hours later (20th July at 6 UTC) the wave begins to break and the tip of the tongue elongates until forming a filament. The folded region also follows the tongue elongation and cross sections reveal that the 340 K surface tilts down along the folding intrusion, so it does the tongue. At the same time, it is interesting to notice that the low PV values on the east ridge lengthen poleward. One day after, on the 21st July at 6 UTC, the filament of relatively high PV is completely detached from the 2 PVU boundary and enterely sourrounded by tropospheric PV values. In addition, the filament of low PV is also detached and advected far poleward evidencing the two-way nature of the interaccion. This specific case serves as an illustration of how isentropic and irreversible mixing may occur locally in the vicinities of tropopause folds below the level of wind maximum, where vertical distortions of the PV field come accompanied by isentropic horizontal PV distortions.

Examinations of 6-hourly images during the month of July show that the almost permanent zonally aligned tropopause folds associated with the zonal jet deforme and increase their folded area when the zonal flow is disturbed and mislays its west-east alignment. That happens, basically, when the summer jet interacts with extratropical weather systems (as in the above example), which induce some cyclonic curvature to the jet flow, and at the entrance of the jet where it gets anticyclonic curvature from the poleward west branch of the upper-level anticlyclone. The latter is precisely where the major frequency of folds is found during this month (see figure 4.2) and where, as it will be shown below, a considerable amount of them exhibit intense fold characteristics (see figure 4.5b).

4.1.3 The Extratropics

In the northern winter extratropics (35°N-80°N), TF activity (Figure 4.1a) shows a widespread geographical distribution with frequency values around 2-5%, with the exception of the north Eurasian continent where TF formation occurs less frequently. Particularly, the highest frequencies extend all over the North Pacific Ocean and along the North America East Coast towards the southern tip of Greenland and Iceland. This latter tongue track follows a climatological jet that breaks over the

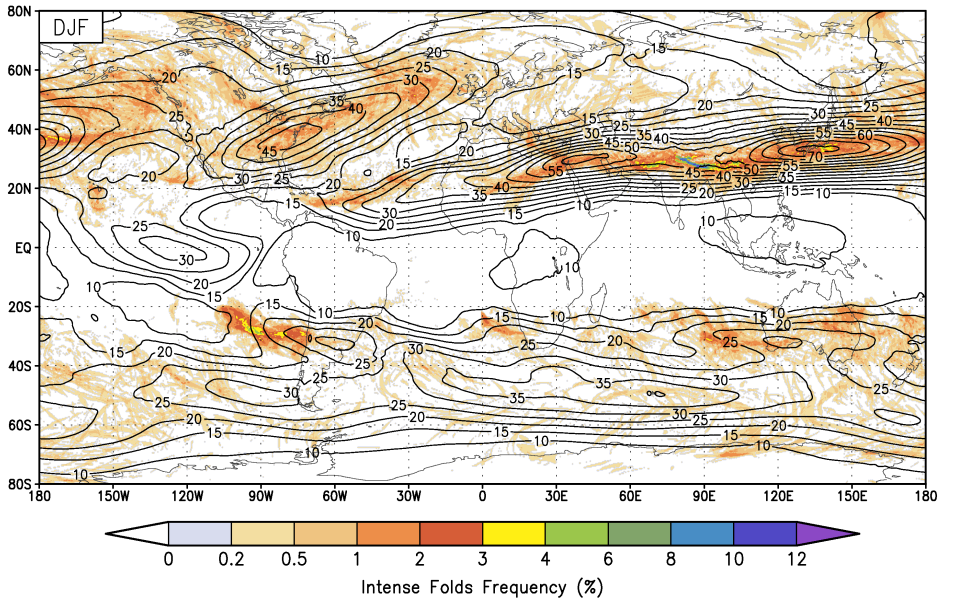

(a) DJF

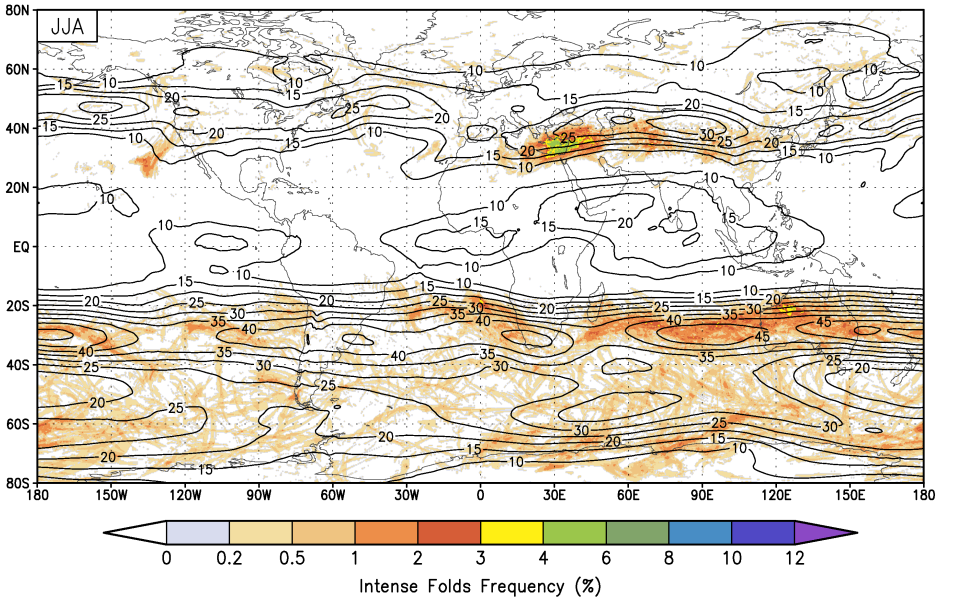

(b) JJA

Figure 4.5: *Seasonal mean spatial distribution of intense fold (gap $\geq$ 200 hPa) frequency (in %) for a) winter (DJF), b) summer (JJA), c) spring (MAM) and d) autumn (SON), from one year of GFS analysis data (Dec 2007 - Nov 2008). Contours of horizontal mean wind at 200 hPa are superimposed with a 5 ms^{-1} wind interval.*

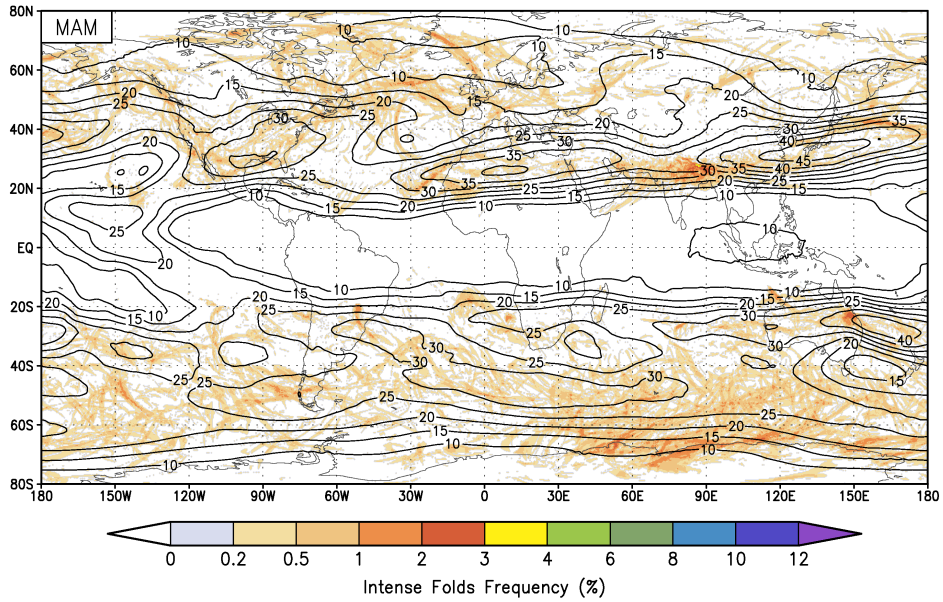

(c) MAM

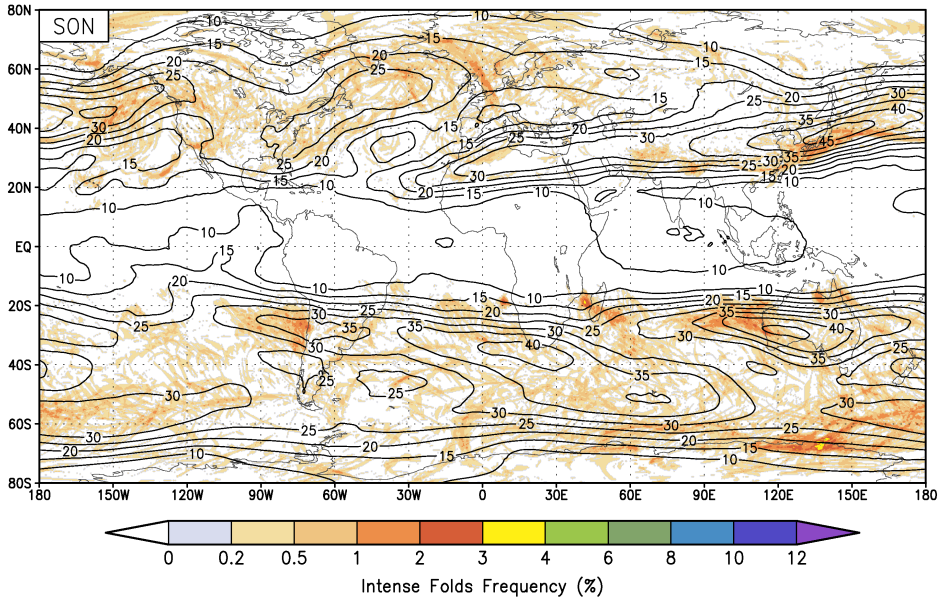

(d) SON

Figure 4.5: *Seasonal mean spatial distribution of intense fold (gap $\geq$ 200 hPa) frequency (in %) for a) winter (DJF), b) summer (JJA), c) spring (MAM) and d) autumn (SON), from one year of GFS analysis data (Dec 2007 - Nov 2008). Contours of horizontal mean wind at 200 hPa are superimposed with a 5 ms^{-1} wind interval.*

subtropical west Atlantic region and elongates northeast towards higher latitudes. Spring and autumn (Figures 4.1c and 4.1d) show a weaker activity compare to that of the winter with slightly higher fequencies during autumn than spring. In both seasons, the highest extratropical activity is also found over the storm track regions of the North Pacific and North Atlantic Oceans. In the northern summer (Figure 4.1b), extratopical TF activity decreases everywhere nearly vanishing. This strong annual cycle is linked to the midlatitude synoptic-scale cyclone activity. In the southern hemisphere, extratropical TF behaviour is similar to that of the northern hemisphere though it has smaller seasonal differences. Activity is found spread along the storm track over the Southern Ocean with major values over the eastern part between longitudes 30°E-150°E. Austral winter shows an slightly weaker and more homogeneous TF ditribution than boreal winter and the reduction experimented in boreal spring and autumn are hardly recognized in both autral seasons. In summer, although TF activity decreases noticeable, still some sights can be appreciated over the South Indian Ocean and the South Pacific Ocean. The weaker annual cycle of TF activity and the higher homogeneity in TF distribution are consistent with the weaker and more uniform extratropic synoptic circulation and the smaller differences between season dynamics of the Southern Hemisphere.

Although frequencies are much lower in the extratropics than in the subtropics, TF formation in the extratropics is of great relevance since the larger part of those fold events are much intense and go deeper into the troposphere. Following the work of Sprenger et al. (2003), who proposed a TF classification depending on the vertical distance (ΔP) between the upper and the middle tropopause crossing (gap magnitude), an analysis of TF frequencies for intense folds (gap $\geq$ 200 hPa) is shown in Figure 4.5. Although Sprenger et al. presented three different categories: deep folds (gap $\geq$ 350 hPa), medium folds (350 $>$ gap $\geq$ 200 hPa) and shallow folds (200 $>$ gap $\geq$ 50 hPa), only two have been considered in this work: intense (gap $\geq$ 200 hPa) and weak (200 $>$ gap $\geq$ 50 hPa) folds. The medium and deep folds have been examined together into the intense fold classification in this study since in the work of Sprenger et al., deep folds were found to be rare features with poor frequency values and without offering an special contribution to the geographic distribution of that offered by medium folds. The geographical distributions of intens TF (Figures 4.5a to 4.5d) reveal the same pattern and seasonal variability in the extratropics as that shown by the totality of folds. Maximum values are still found on specific located spots of the winter subtropics (north India and China and west Australia) and the westernmost regions of influence of the most active summer monsoon circulations (East Mediterranean Coast and Turky and South America Pacific Coast), precisely coinciding with subtropical TF frequency maxima. However, outside of these maxima, subtropical intense fold activity deacreases noticeable. Contrasting frequency values of intense folds with total fold frequency values, the majority of TF

events in the extratropics correspond to intense fold cases whereas only a portion of them occur in the subtropics. The geographical distribution of these ratios (in %) averaged for the entire year (Dec 2007 to Nov 2008) is shown in Figure 4.6.

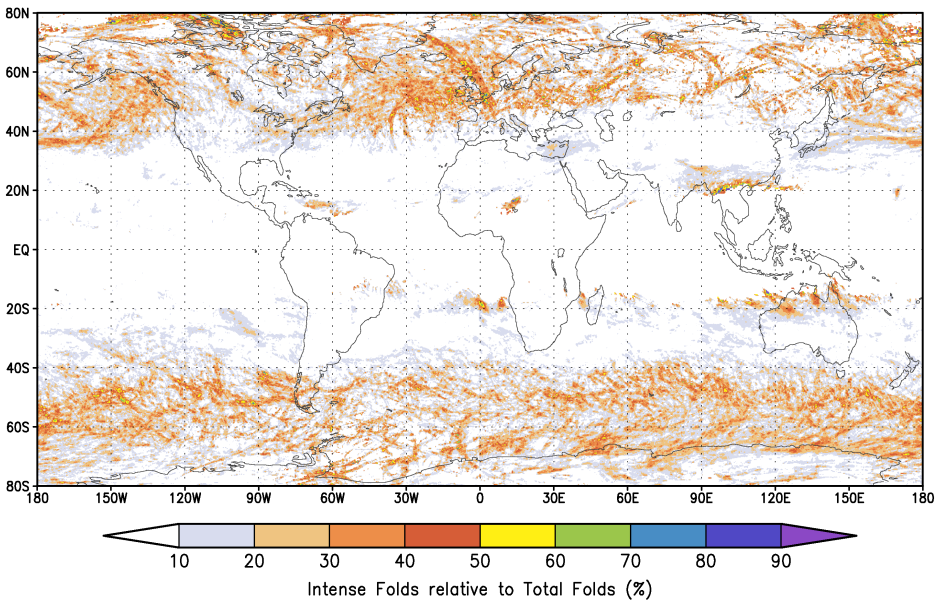

Figure 4.6: *One year mean (Dec 2007 - Nov 2008) spatial distribution of intense fold (gap ≥ 200 hPa) occurrences relative to total fold occurrences (in %), from GFS analysis data.*

In both hemispheres, values closed to 50% are well spread over the entire extratropics while mostly values lower than 20%, excluding only isolated areas, cover the subtropics. Besides, one detail to consider when examaning these fractions is the fold indentification by itself. As explained previously in chapter 3.3.2 the presence of a fold and its characteristics (i.e. gap, depth, etc.) are calculated for every grid point affected by a double crossing of the 2 PVU surface, including each indivial fold case many of these grid points. Consequently, if one intense fold event is considered, it may include a certain number of grid points not recognized as intense but shallow (gap $<$ 200 hPa), at least the folded grid points adjacent to the joining free stratosphere. This is illustrated more clearly in the vertical cross section of Figure 4.7 (right) which shows a typical intense fold that goes down to the 650 hPa level and reaches the 400 hPa gap value. Even so, the algorithm will record typical shallow fold characteristics (small gaps) on the grid points closed to the non-folded tropopause (i.e. grid points in peach color in Figure 4.7, left). Therefore, many intense fold events provide significant intense fold frequencies as well as shallow fold frequencies, and extratropical ratios of intense to total fold occurrencies around 50% are big enough to suggest that almost all extratropical fold events have intense and

deep characteristics. A simple examination is performed to confirm this idea. It consist in evaluating over different extratopical fold events the "intense fold area ratio", which is defined as, for an individual fold case, the ratio of the area covered by gap values greater than 200 hPa to the total area covered by the fold. An exemple can be viewed in Figure 4.7 (left). All the extratropical cases examined show ratio values within the expected range, varying from 0.41 to 0.64.

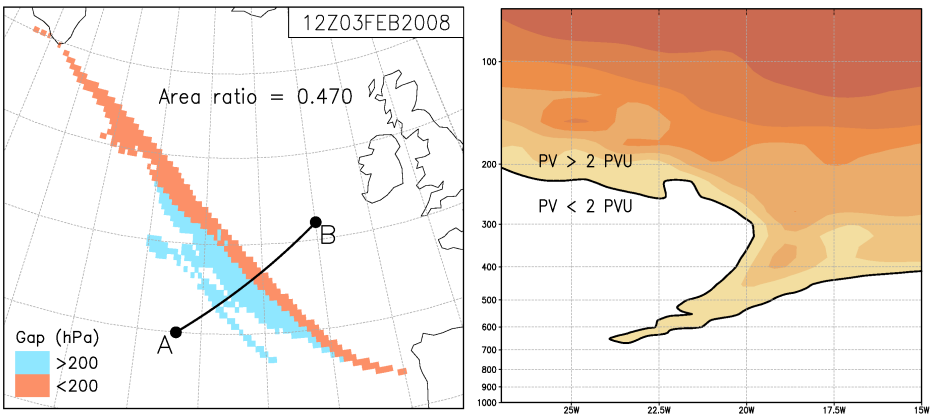

Figure 4.7: *Intense tropopause fold event on the 3rd February 2008 at 12 UTC over the North Atlantic Ocean. Left: gap magnitude of the folded 2 PVU surface area and ratio of gap ≥ 200 hPa area to total folded area. Right: vertical cross section of potential vorticity (PVU) across the segment A-B from left. From GFS analysis data.*

Another way of examining intense fold structures is to consider the penetration level of the intrusion (depth magnitud) instead of the gap distance. Hence, a new division is made between intense (named Deep hereafter) and shallow folds depending on weather the depth magnidtude is greater or lower than 450 hPa, respectively. Figures 4.8a to 4.8d show again the seasonal global distributions of Deep TF frequencies following this criterion. They highlight, for both hemispheres and for the 4 seasons (DJF, MAM, JJA and SON), visible higher values in the extratopics and lower values in the subtropics than thoses found in figures 4.5a to 4.5d where the gap classification has been used. The increment experimented in the extratropics is easily explained looking at typical TF shapes in cross sections such as that in Figure 4.7 (right), where the entire folded dynamical tropopause is below the 450 hPa level although a significant portion has gap values lower than 200 hPa. Analogous area ratios as in Figure 4.7 (left), though for deep to total areas in that case, have been examined for the same previous sample of cases and all of them show notably greater values, varing from 0.75 to 1. The situation in the subtropics is completely different. The frequencies found are significantly lower compared to those in figures 4.5a to 4.5d, what emphasize the fact that subtropical TF are shallower structures that do not go deep into the troposphere, however still considerable cases show large gap

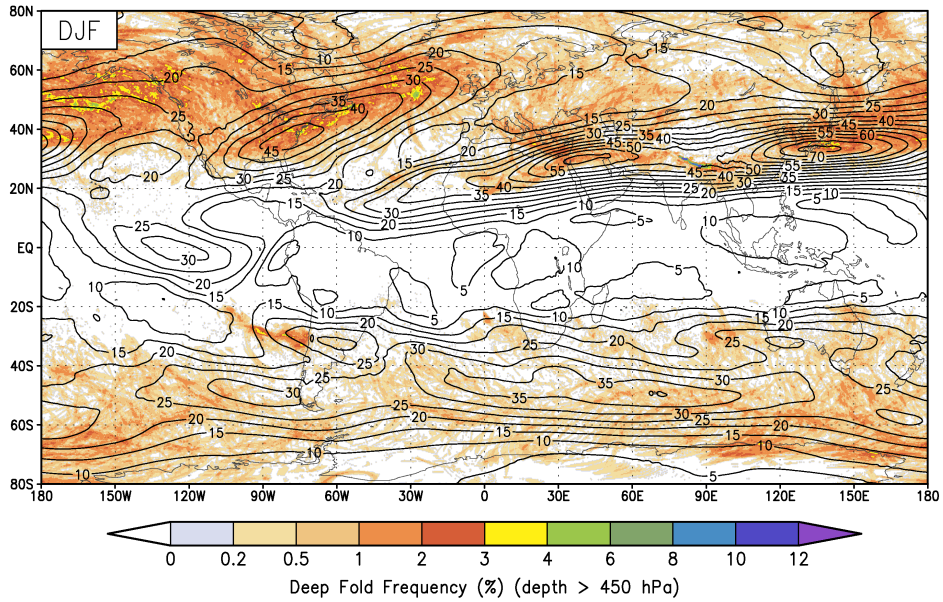

(a) DJF

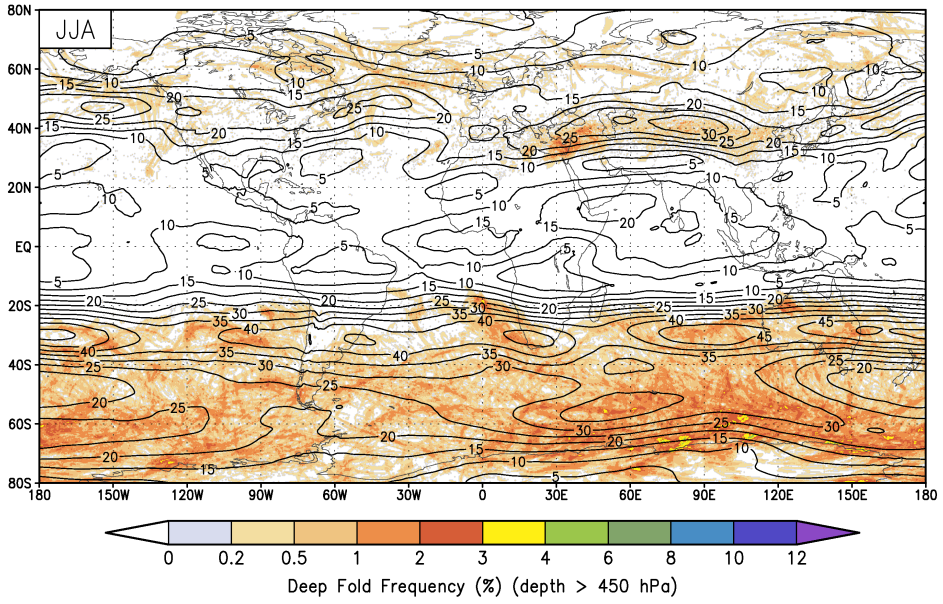

(b) JJA

Figure 4.8: *Seasonal mean spatial distribution of deep fold (depth ≥ 450 hPa) frequency (in %) for a) winter (DJF), b) summer (JJA), c) spring (MAM) and d) autumn (SON), from one year of GFS analysis data (Dec 2007 - Nov 2008). Contours of horizontal mean wind at 200 hPa are superimposed with a 5 ms^{-1} wind interval.*

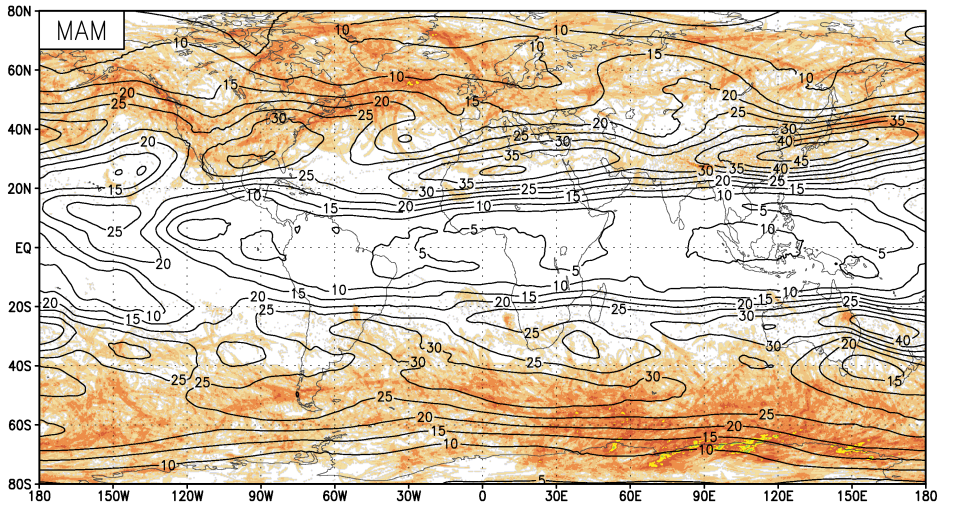

(c) MAM

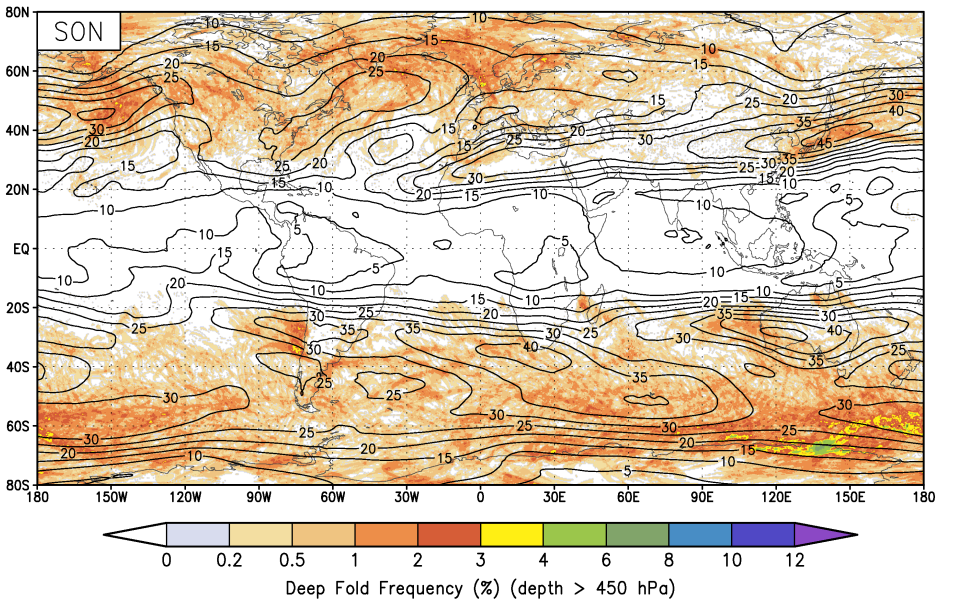

(d) SON

Figure 4.8: *Seasonal mean spatial distribution of deep fold (depth ≥ 450 hPa) frequency (in %) for a) winter (DJF), b) summer (JJA), c) spring (MAM) and d) autumn (SON), from one year of GFS analysis data (Dec 2007 - Nov 2008). Contours of horizontal mean wind at 200 hPa are superimposed with a 5 ms^{-1} wind interval.*

structures. This will be further discussed in the following section where the different TF geometric characteristics and their mean global distributions are wider analysed.

4.1.4 The Annual Cycle

Figure 4.9 shows the annual variation of the total amount of subtropical (solid line) and extratropical (dashed line) fold ocurrences for the South and North Hemispheres (NH and SH). The subtropical samples of NH and SH comprise, respectively, the latitudes between 5° and 40° during the boreal/austral winter, spring and autumn seasons and the latitudes between 5° and 45° during the boreal/austral summer season. On the other hand, the extratropical samples cover on each season the complementary latitudes up to 80°. These 5 degrees latitude increase on the subtropical samples during the summer months is performed in order to consider the summer jet displacement with the aim of roughly separate the folds associated with the subtropical jet from those mainly associated with the extratropic atmospheric circulation. Notice that the number of folds in the extratropics is about half an

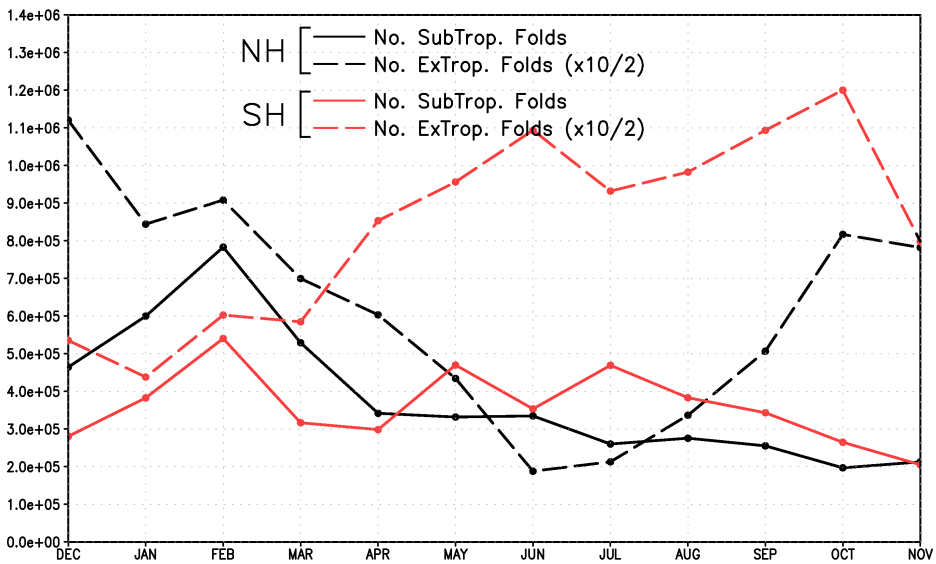

Figure 4.9: *Annual variation of the total number of subtropical (solid line) and extratropical (dashed line) fold occurrences for the Northern Hemisphere (black) and the Southern Hemisphere (red) from GFS analysis data. The subtropical sample of the NH (SH) englobes the latitudes between 5° and 40° in the boreal (austral) winter, spring and autumn months, and the latitudes between 5° and 45° in the boreal (austral) summer months. The extratropical samples comprise the remaining latitudes to 80° for each month. The values for extratropical folds have been multiplied by 10 and divided by 2.*

order of magnitud smaller than the number of folds in the subtropics. As anticipated from the seasonal geographical TF distribution, fold activity in the Northern Hemisphere reveals a pronounced seasonal variability with clear maxima in winter (February in the subtropics and December in the extratropics). The northern subtropical activity displays quite uniform smaller values from April to November with a minimum in autumn, while in the extratropics a clear minimum is found during summer (June/July). In contrast, the seasonal cycle in the Souther Hemisphere is weaker, almost absent in the subtropics. In the southern extratropics, significant activity is found from middle autumn (April) to late spring (November) with a peak in October and a second maximum in June (austral winter).

The subtropical and extratropical annual cycle separated by the amount of Deep (depth $\geq$ 450 hPa) and Shallow (depth $<$ 450 hPa) folds can be observed in figure 4.10. In both hemispheres in the subtropics (solid lines), the number of Deep folds is an order of magnitud smaller then the amount of subtropical Shallow folds and both, Shallow and Deep, follow a similar annual behaviour as that observed in figure 4.9: a remarkable peak in February in the Northern Hemisphere and little annual variability in the Southern Hemisphere, although slightly higher Deep subtropical fold cases can be observed during autral winter and early austral spring. In the extratropics (dashed lines) the picture is quite different. The number of Shallow and Deep folds are about the same order of magnitud but the amount of Deep folds is about 2-3 times bigger during the cold seasons. Besides, Shallow folds show a weak

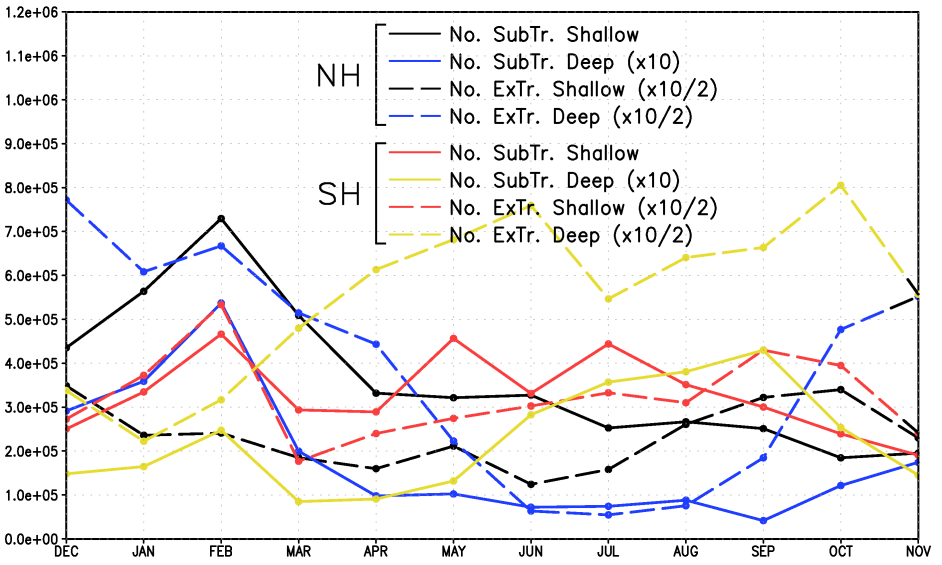

Figure 4.10: *Same as figure 4.9 for Shallow (depth $<$ 450 hPa) and Deep (depth $\geq$ 450 hPa) fold cases.*

seasonal cycle while Deep folds reveal a pronounced variability. Notice also that, in the Northern Hemisphere, extratropical Deep cases during summer are almost nonexistent as well as subtropical Deep cases from middle spring to early autumn.

The same re-counting has been made discriminating between Intense (gap $\geq$ 200 hPa) and Weak (gap $<$ 200 hPa) folds (not shown) and some interesting differences can be identified. On the one hand in the subtropics, a few more Intense cases are detected during the summer seasons compared to the subtropical summer Deep cases (almost nonexistent) and the peak in February of Deep folds is more pronounced for the Intense folds. On the other hand in the extratropics, although Intense cases follow a similar annual variability as Deep cases, the total amount of Intense folds is about the half of the Deep cases. Instead, the number of extratropical Weak ocurrences is bigger and acquires the characteristic extratropical fold seasonality observed aboved. These foundings further support the differences observed in the previous subsection (4.1.3) between the seasonal distributions of Intense and Deep fold frequencies (figures 4.5 and 4.8).

Although just one year of data is evaluated in this work and it may exist large interannual variations (specially for localized areas), the main features observed in the TF seasonal cycle agree rather well with previous TF climatologies in the extratropics (Elbern et al. 1998, Rao et al. 2008, Antonescu et al. 2013) and for Weak and Intense folds (Sprenger et al. 2003).

4.2 Vertical and Horizontal TF Characterization

Vertical and horizontal tropopause fold geometric features are analysed in this section. The fold-searching algorithm computes and registers 5 different geometric tropopause fold parameters at each grid point where a folded structure of the 2 PVU surface is found. Theses quantities, which provide information about the magnitude and expanse of the intrusions, are: the gap, the depth, the thickness and the zonal and latitudinal widths. Figure 4.11 shows an sketch of how these variables are evaluated, for further details see subsection 3.3.2 in chapter 3.

4.2.1 Vertical structure

Both gap and depth give a measure of the scope and intensity of penetration of the fold intrusion into the troposphere, in particular the depth registers the lowest height (maximum pressure value) reached by the intrusion. The next two figures (4.12, 4.13) show respectively the global distributions of the mean depth and the mean gap fold characteristics averaged for the entire year (Dec 2007 to Nov 2008).

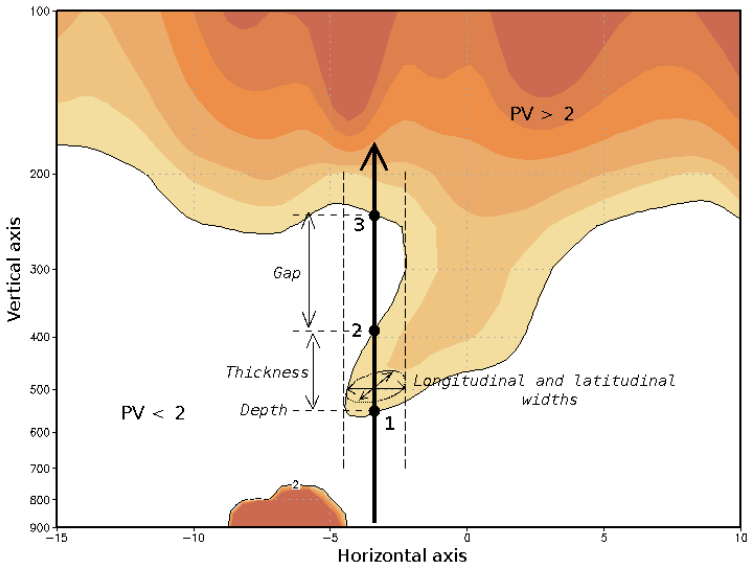

Figure 4.11: *Illustration of a tropopause fold PV cross section (longitud-pressure) showing the searching folding process and the different fold characterization parameters.*

Both highlight, especially the mean depth distribution, the disctinction between the subtropics and the extratropics regarding the vertical structure and intensity of tropopause folds. In both hemispheres, tropopause folds in the subtropics are in general shallow structures that occur at high levels and sink little into the troposphere while in the extratopics they present a more vertical extend. Moreover, higher depths of penetration are found during winter seasons (see e.g. figure 4.15). Bush and Peltier (1994) demonstrated the important role played by the basic-state baroclinicity in determining the depth to which the fold penetrates into the troposphere. They found that the vertical depth of penetration increased with an enhanced of the main state baroclinicity, which is consistent with the pattern and seasonal distributions of the mean gap and depth magnitudes found in this work.

Figure 4.12 shows small mean depth values (about 300 hPa) between latitudes 15° and 30°, North and South. Only between longitudes 60°E-120°E in the northern hemisphere and 90°E-150°E in the sourthern hemisphere are found slightly higher mean depth values in such lower latitudes. Between latitudes 30° and 45°, there is a transition zone with a poleward increasing mean depth, result of averaging the typical latitude seasonal displacement of the subtropics (and the related tropopause break) over the entire year. Poleward of 45 degrees, high mean depth values are spread around the entire extratropics, with peaks greater than 600 hPa in many places. A peculiarity though, is observed over the Antarctica continent interiors where mean depth values are lower than the surroudings and the similar northern

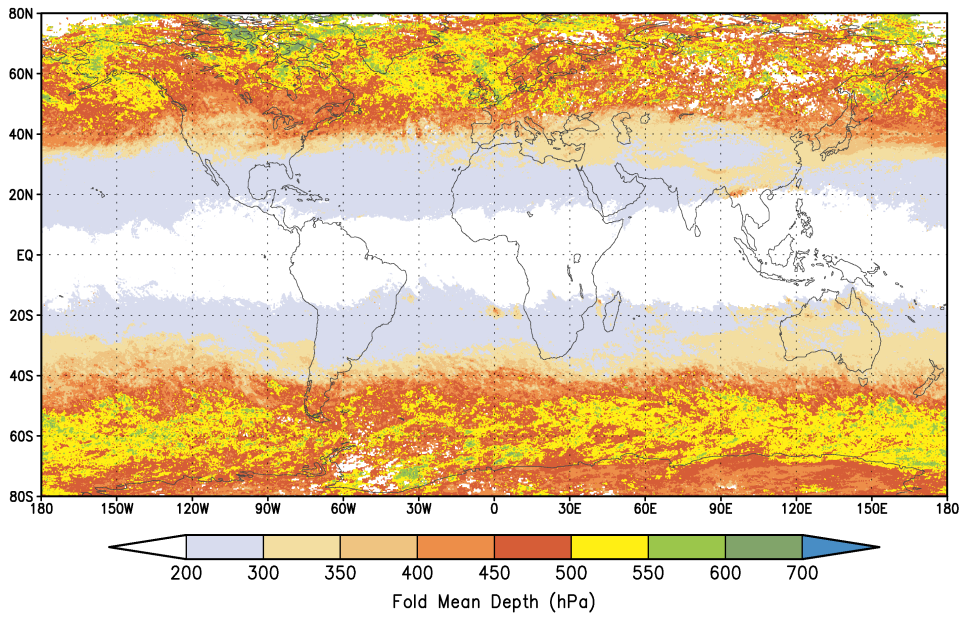

Figure 4.12: *Year mean spatial distribution of TF depth value (hPa), from one year of GFS analysis data (Dec 2007 - Nov 2008).*

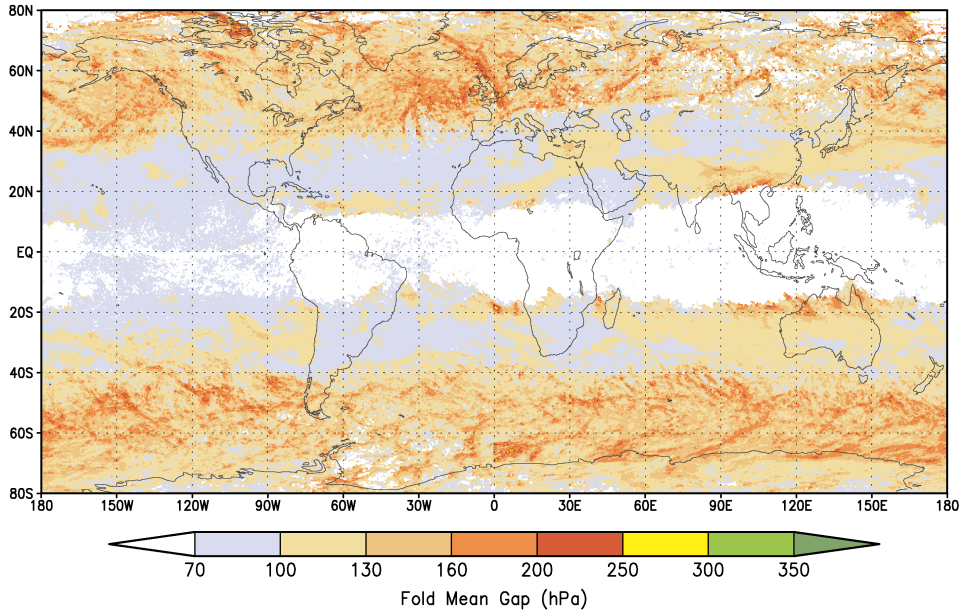

Figure 4.13: *Year mean spatial distribution of TF gap value (hPa), from one year of GFS analysis data (Dec 2007 - Nov 2008).*

hemisphere latitudes. A seasonal examination (not shown) reveals that this singularity is basically coming from the Antarctica winter months (from Juny to October). Cross sections during these months show large areas covered by persistent and strong surface stable layers that generate large zones of high $|PV|$, mostly over the Antarctica Plateau and surrondings, and generally within the 700 hPa and the 550 hPa. First, this strong stability inhibits vertical movements and prevents the possible subsiding tropopause to go deeper. Second, if a tropopause fold merges with that large surface high $|PV|$ bubble the tropopause fold searching algorithm cuts the considered folding depth at the highest level (minimum pressure) of the bubble, making it impossible to register higher tropopause fold depth magnitudes. This is necessary in order to prevent the algorithm considering mistakenly the Antarctic winter tropopause as an almost permanent folding tropopause, and it has been adjusted on purpose in the algorithm along the Antarctica latitudes.

The mean gap distribution (figure 4.13) follows a similar pattern, but the distinction between subtropical and extratropical fold gap properties is less clear. In general, mean gap values in the subtropics are small but they show less zonal homogeneity and some subtropicals regions display comparable values in magnitude as those found in extratropical regions, precisely where the highest intense fold frequencies are found (see figures 4.5a to 4.5d). The formation of tropopause folds in the vicinities of the tropopause break can easily record significant gap values together with relatively small depths. On the cyclonic side of an upper jet, the isentropes tilt downward forming an upper-front and generating a tropopause fold that penetrates downward and folds under the jet core following the tilted isentropes (see figure 4.14). Therefore, alongside the subtropical westerly jet, tropopause folds roll down equatorward from the low-level extratropical tropopause to beneath the high-level tropical tropopause. Even if tropopause folds do not go deep into the troposphere, and they usually do not in the subtropics, significant gap values can be found if the local tropical tropopause is anomaly high.

The fold geometric features examined so far have been focused on a one year mean evaluation. This type of analysis, although it is interesting from a climatological point of view and it provides a good insight into the different regional characteristics, it can smooth out the individual behaviour of stratospheric intrusions. Scatter plots offer good detail of individual fold features and they can show veritable depth magnitudes attained by the intrusions. In Figure 4.15 can be observed the gap-depth relationship discriminated by 5 degrees latitude colours for January and July, in the North (top row) and South (bottom row) Hemispheres. Two black lines separate each phase space in four quadrants depending on gap values lower of bigger than 200 hPa and depth values lower of bigger than 450 hPa. In the first place, these plots underline the seasonal and hemispherical differences observed in section above: higher and more extended activity during winter than in summer months,

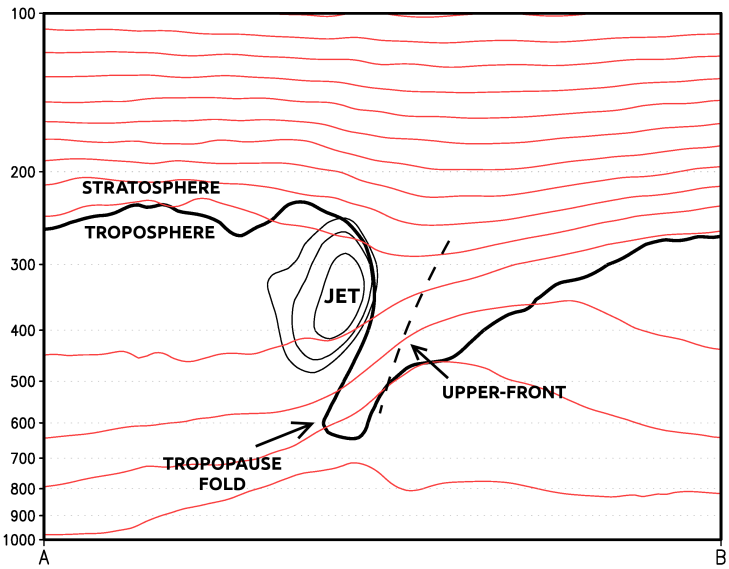

Figure 4.14: *Conceptual model of atmospheric conditions in a cross-section tropopause fold event.*

especially on extratropical latitudes, and weaker differences between both seasons in the southern Hemisphere compared to the northern Hemisphere cycle. Secondly, regarding the gap and the depth fold properties, they also highlight strong seasonal and subtropical-extratropical contrasts. Strongly marked is aswell the summer displacement of subtropical conditions to higher latitudes, especially in the northern hemisphere.

On tropical latitudes, red points enclosed on the lowermost part of the phase space, are merely found small undulations of the 2 PVU surface generated at high levels that can not be even considered real fold structures. Moreover, examinations on the thickness magnitude (not shown) point out that all of this small fluctuations consist of really thin formations. The high density of points on the bottom-left quadrants coloured by subtropical latitudes stress the idea that subtropical TF are in general shallow structures that occur at high levels and sink little into the troposphere. However, as described above, a significant amount of subtropical points show considerable gap values with relatively small depths (bottom-right quadrants), mainly associated with the generation of folds near the tropopause break with an adjacent anomaly high tropical tropopause.

As observed and discussed in section above 4.1.3, the majority of extratropical cases are found above the 450 hPa line although quite a few of them show small gap propierties ($<$ 200 hPa). Particularly, on the topmost region of these top-left quadrants, especially in January in the northern Hemisphere, are found quite a few

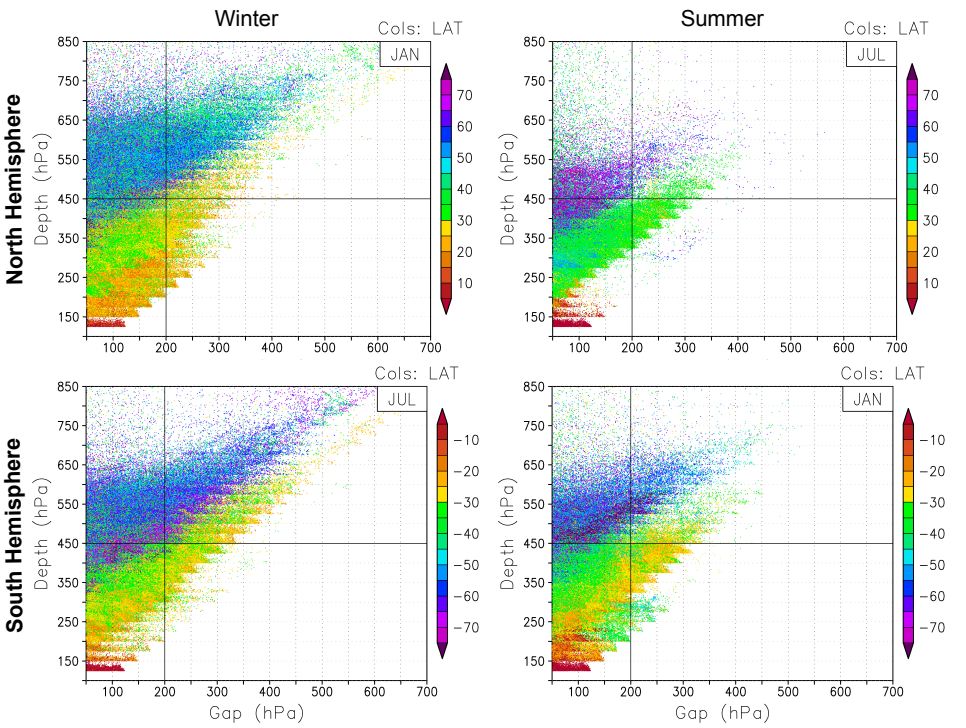

Figure 4.15: *Scatter plots of the Gap and Depth tropopause fold geometric characteristics for the North (top row) and South (bottom row) Hemisphere for an entire month in winter (left column) and in summer (right column). Coulored by 5° latitude intervals. From GFS data.*

of cases with unusual big depths (e.g. depth $>$ 700 hPa) together with relatively small gaps (e.g. gap $<$ 100 hPa). As expected, the majority of those cases exhibit considerable big thicknesses, which explains that peculiar combination. Only singular cases are beyond that scenario and they can be considered spurious fold conditions, basically originated by double undulations of the 2PVU surface. When that happens, quite rarely, the fold searching algorithm registers mistakenly the lowest depth from the second undulation and only the gap distance between the first and the second undulation.

The biggest gaps and depths (top-right quadrants) are found in the winter hemispheres, but also during spring and autumn (not shown). Therein, a significant amount of cases with depth values beyond the 700 hPa and gap distances greater than 350 hPa are observed. Although these big structures are mainly found among extratopical latitudes, significant activity is also shown in the southern subtropics during winter (JUN, JUL, AUG) and early spring (SEP, OCT). In summer, the intense and deep activity is strongly reduced, especially in the northern hemisphere where rare cases can be found among depths higher than 600 hPa and gaps greater

than 300 hPa.

The third variable in relation to the fold vertical structure that has been examined is the thickness, that is the vertical "width" of the stratopheric tongue (measured in hPa). This magnitude offers a qualitative notion of the amount of stratospheric air mass involved in a TF process. Its year mean geographical distribution (figure 4.16) shows in general thinner values in the subtropical areas than in the extratropical ones, which is in agreement with the foundings of Sprenger et al. (2003) that detected much less fold cases associated with very large exchange fluxes in the subtropics than in the extratropics. However, scatter plots show that although large thick tongues are more commond in extratropical latitudes, relatively thick structures can also be found on subtropical regions (not shown). Figure 4.16 highlights two subtropical regions with significant big mean thicknesses: west Bangladesh and Burma, directly equatorward of the Himalaya Mountains, and around the Cape York Peninsula in Australia. Besides, with the exception of the small and thin tropical undulations, scatter plots show no relationship between the intensity of the fold (gap or depth) and its thickness.

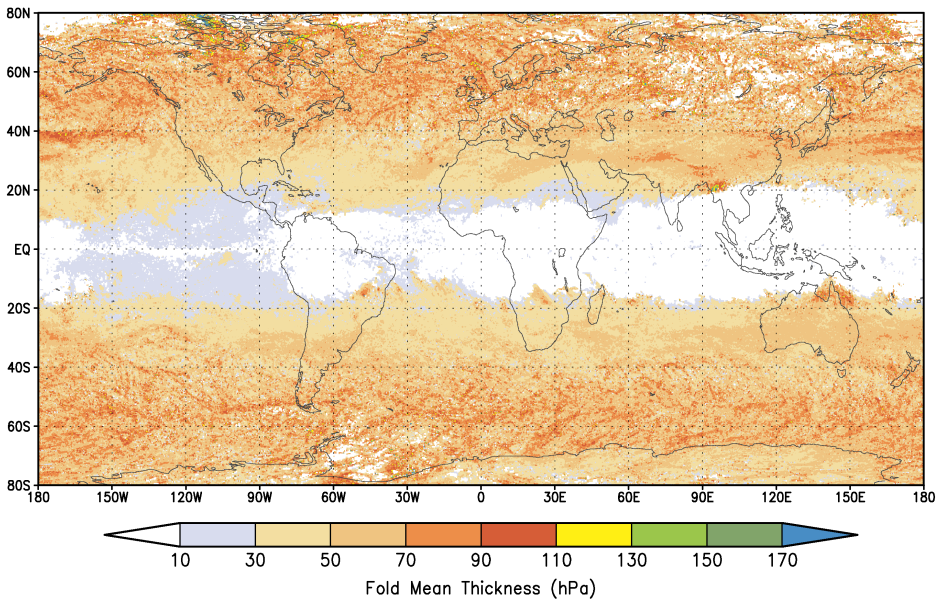

Figure 4.16: *Year mean spatial distribution of TF thickness (hPa), from one year of GFS analysis data (Dec 2007 - Nov 2008).*

Wimmers and Moody (2004b) tested the relationship between the air mass contained in a fold and its dimensions. They found an square proportionality between a two-dimensional integrated air mass and a one-dimensional width distance measured on the transverse direction of the lengthwise fold orientation. Although their results

are not entirely robust because they used a reduce collection of samples, the square relationship makes sense. Unfortunately, knowing the amount of stratospheric air mass involved in a TF process by itself does not directly solve what is presumably the most important aspect of tropopause folding, that is the associated mass flux between the stratophere and the troposphere. Despite the fact that the thickness of the tongue intrusion can give an estimation of the stratospheric air mass intruding into the troposphere, the portion that will be irreversibly staying in the lower atmospheric layer is unknown and strong related to diabatic processes and small-scale turbulences. However, if the stratospheric air is carried down to altitudes low enough the irreversibility is more probable and the stratophere-troposphere transport more effective, not only by active turbulent mixing but also by the extrusion of residual tube-like structures in the mid- and low-level troposphere (Bithell et al. 1999), which slowly and irreversibly will mix and disperse with tropospheric air. Thus the depth or the gap fold magnitudes may also play here an important role.

Figure 4.17 shows a product that combines thickness, depth and frequency of occurrence to portray a broad picture of the regions of the globe where the biggest amounts of mass are likely to be affected by "almost irreversible" stratosphere-troposphere transport due to deep tropopause fold processes. In particular, it displays the product of the average thickness for deep TF cases (Depth $>$ 450 hPa) by their frequency of occurrence, for both hemispheres and for the four season DJF (4.17a), JJA (4.17b), MAM (4.17c) and SON (4.17d). Despite its simplicity the major peaks match well with the existent cross-tropopause mass exchange climatologies. The more relevant regions in the northern winter coincide with the Pacific and Atlantic storm track regions, where e.g. Wernli and Bourqui (2002) found maxima deep STE (stratospheric air that penetrates below the 700 hPa) during the winter 1995-1996 using a trajectory-based Lagrangian technique. These two dominant regions of Stratosphere-Troposphere Transport (STT) have also been reported by other studies (Sprenger et al. 2003, James et al. 2003, Sprenger and Wernli 2003, Olsen et al. 2004, Škerlak et al. 2014) together with remarkable activity during spring and autumn, and the linkage observed in figures 4.17a, 4.17c and 4.17d confirms the important role played by extratropical tropopause folds associated with baroclinic wave activity. The other significant peaks in figure 4.17a over the Himalaya Mountains, North America continent and eastern Mediterranean and Middle East countries have also analogous distinc maxima in the northern winter cross-tropopause exchange analysis of Wernli and Bourqui (2002) (although less pronounced) and Sprenger et al. (2003), as well as in the more robust 15-year climatology of Sprenger and Wernli (2003) and the most recently 33-year climatology of Škerlak et al. (2014). The latter found intense STT flux over the Himalaya Mountains (on the upwind side or directly over the high-altitud areas) during DJF and MAM, coinciding with prominent peaks in figures 4.17a and 4.17c which are precisely located on the southern

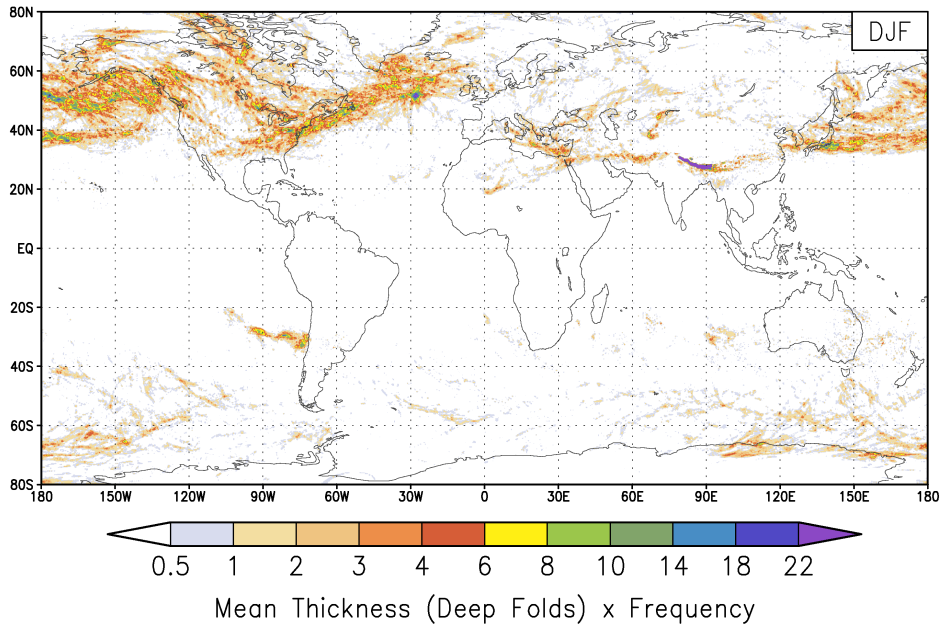

(a) DJF

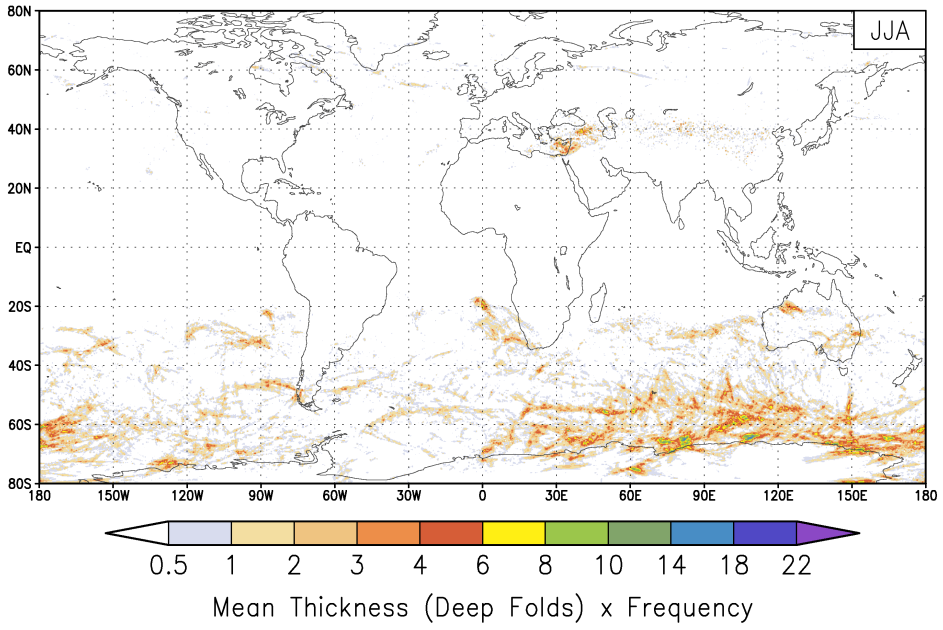

(b) JJA

Figure 4.17: *Deep Tropopause Fold Stratosphere-Troposphere Mass Transport Index for the four seasons a) DJF, b) JJA, c) MAM and d) SON, from one year of GFS analysis data (Dec 2007 - Nov 2008).*

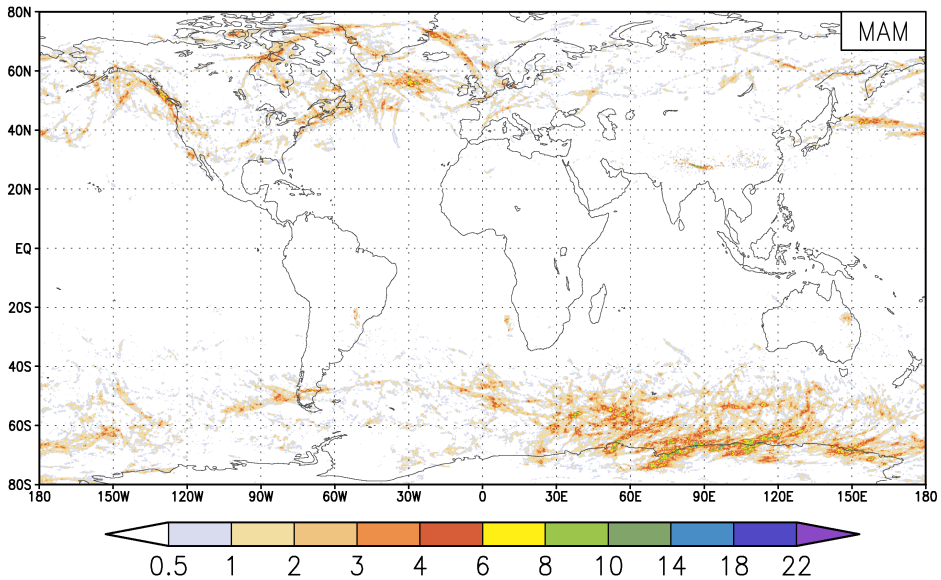

(c) MAM

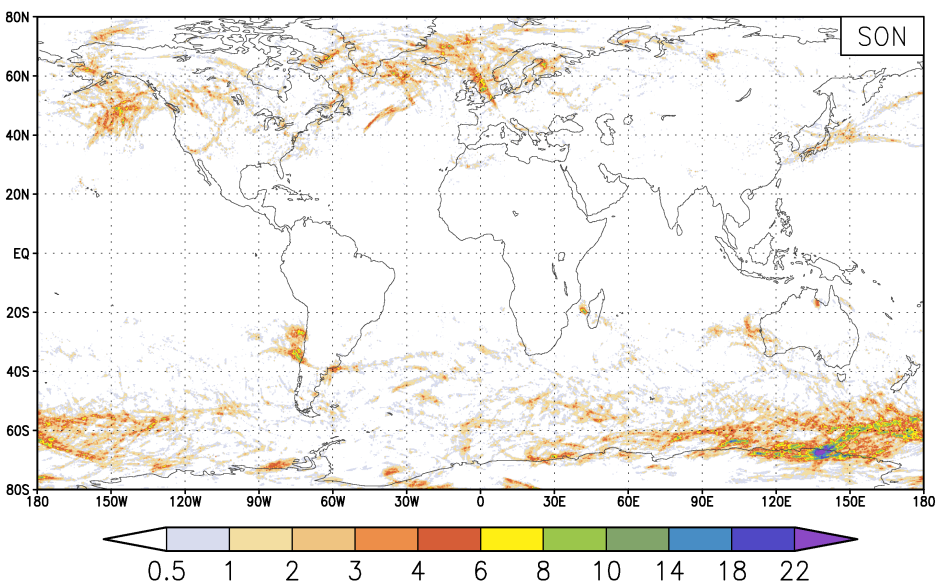

(d) SON

Figure 4.17: *Deep Tropopause Fold Stratosphere-Troposphere Mass Transport Index for the four seasons a) DJF, b) JJA, c) MAM and d) SON, from one year of GFS analysis data (Dec 2007 - Nov 2008).*

part of the Tibetan Plateau where a high orography raises up from the southern low lands. In a previous study, Chen et al. (2013) showed that TF occuring over the Tibetan Plateau can reach the exceptional winter high Atmospheric Boundary Layer (ABL) and that could favour deep STT. Indeed, they proposed that a close surface-troposphere-stratosphere coupled system may exist over the Plateau. The tilted (quasi-vertical) potential temperature surfaces associated with the folded tropopause, which create an unstable intrusion area, can easily reach the high elevated Plateau surface and facilitate the growth of the ABL to high levels. At the same time, that interaction between the intrusion and the ABL may possible increase the depth of the tropopause fold itself and that would provide a potential interpretation for the high deep fold frequency values observed in figure 4.8a.

Škerlak et al. (2014) found also prominent maxima over the eastern Mediterranean and Turky and along a band extending over the northern flank of the Asian monsoon anticyclone during summer (JJA), precisely where relevant traces are present on figure 4.17b in the northern Hemisphere and where tropopause folds occur preferentially. Likewise in the southern Hemisphere, the main features visible in figures from 4.17a to 4.17d in the vicinities of the coast of Chile around the 30°S during DJF and SON, over the east and west coast of Australia during JJA and over the zonal band around 60°S present in all four seasons with a minimum during austral summer (DJF), match well with the locations of enhance cross-tropopause mass flux observed in the Škerlak et al. climatology. Hence, this product reproduces the most important regional features of STE climatologies and may probably be an assessment of the main contributions of stratrosphere-troposphere exchange due to deep TF.

4.2.2 Horizontal structure

Regarding the horizontal characteristics of tropopause folds, their zonal and meridional width distances have been analysed. They measure, respectively, the distance (in km) along the longitudinal and the latitudinal directions of the projection of the tongue intrusion on the horizontal plane, calculated at each grid point where a folded tropopause is detected, and they offer information about the extension and horizontal structure of TF. Figures 4.18 and 4.19 show respectively the global distributions of the year mean zonal and meridional width distances.

In the subtropics, large zonal distances are found with maximum values around 1000 km coinciding with the position of the winter subtropical jet. In contrast, relatively smaller meridional distances are observed on those regions. The quasi-permanent folded tropopause co-existing with the westerly jet, which penetrates equatorward from the cyclonic side to under the jet-core, has a fold transvers-jet

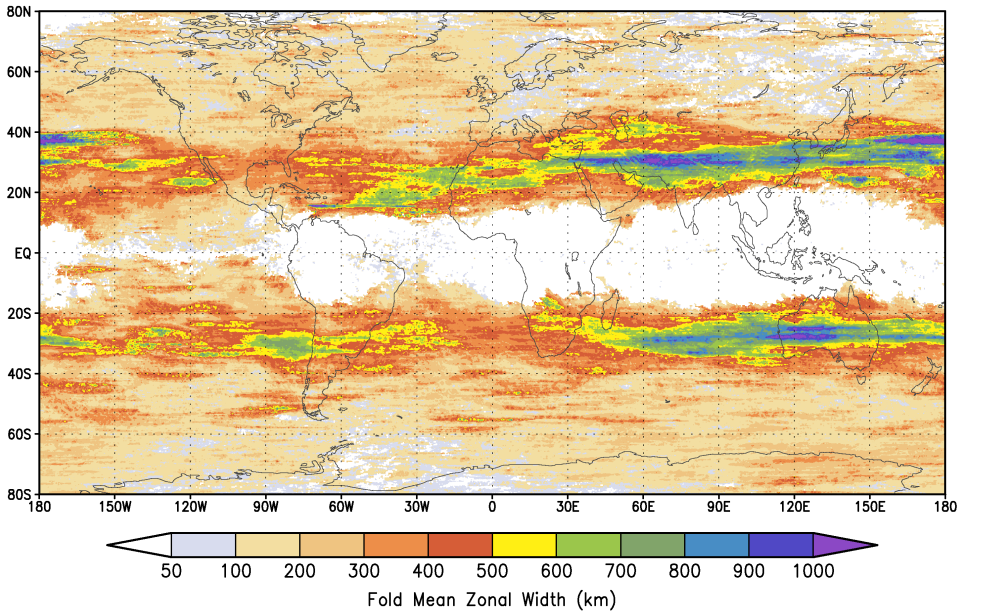

Figure 4.18: *Year mean spatial distribution of TF zonal distance (km), from one year of GFS analysis data (Dec 2007 - Nov 2008).*

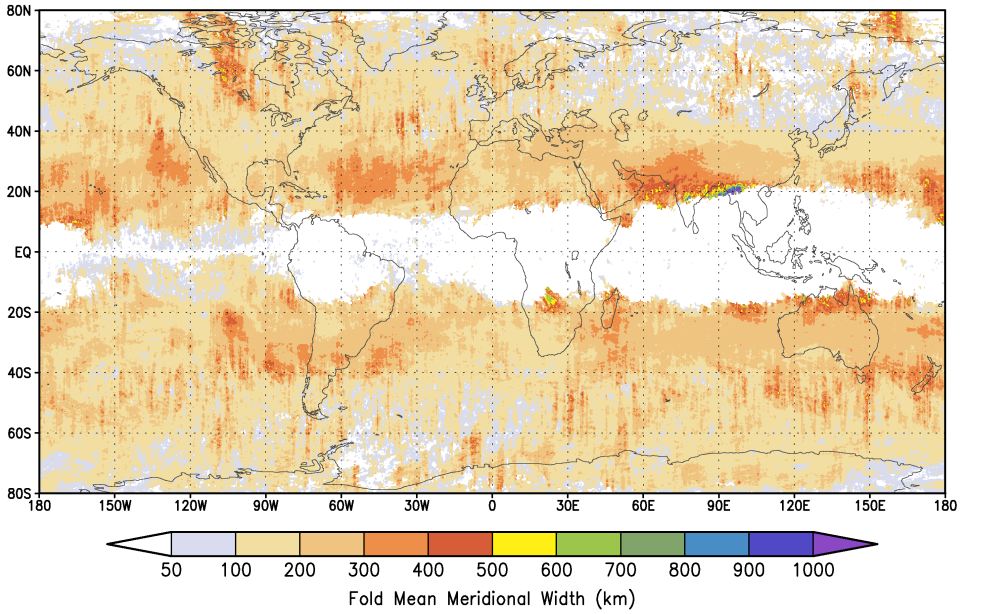

Figure 4.19: *Year mean spatial distribution of TF meridional distance (km), from one year of GFS analysis data (Dec 2007 - Nov 2008).*

extent about the same order of magnitud than the jet width distance (see scheme in figure 4.14) typically ranging around 100-400 km, and it is in the jet-traveling direction that the tropopause can fold for big distances all along the jet extension, easily reaching values of more than 2000 km long. However, some subtropical regions show relatively higher mean meridional distances. For instance in the Northern Hemisphere, it can be observed two relative maxima over Central Pacific and Atlantic oceans and a prominent maximum in South Asia around 20°N, from the Arabian Sea to Burma where a peak value of more than 900 km can be found. The three regions coincide, although sligthly equatorward, with the zonal discontinuities of the westerly jet (see e.g. figures 4.1a and 4.1c), precisely where the zonal flow is more likely to have some meridional component and abandon the zonal symmetry and that is, therefore, where folds are more likely to extend on the meridional direction. Indeed, the Pacific and Atlantic areas are typical Rossby-wave breaking regions. Besides, a daily examination revealed that over the region in South Asia few tropopause fold cases during winter and spring covered large meridional areas. Specifically, the huge values in figure 4.19 over the Bay of Bengal and Burma (far equatorward of the Tibetan Plateau) derive from an strong and single (very little tropopause fold frequencies can be found here) tropopause fold episode that crossed that area from north India to south China during four days, from February 19 to February 22. The upper-level synoptic situation and the horizontal and vertical structure of the associated tropopause fold on the 20th February at 12 UTC can be

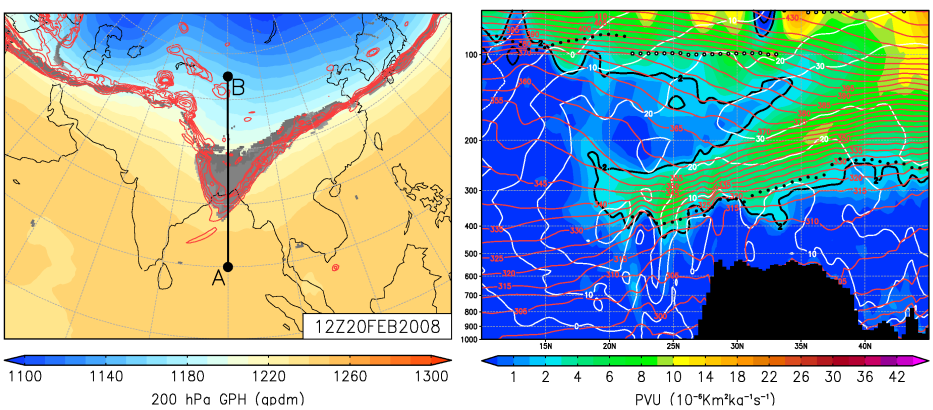

Figure 4.20: *Tropopause fold event on 20 February 2008 at 12 UTC over South Asia. Left: geopotential height at 200 hPa, folded tropopause regions (grey shades) and PV contours (1.5, 2, 2.5, 3, 3.5 and 4 PVU) on the 340 K surface. Right: vertical cross section of potential vorticity (PVU) across the line A-B (90°E) in left. Zonal winds (black contours) and potential temperature (red contours) are superimposed. Bold black contour indicates the dynamical tropopause and black dots the lapse rate tropopause. Unfilled dots indicate the presence and position of a second lapse rate tropopause. From GFS analysis data.*

viewed in figure 4.20. The geopotontial height field at 200 hPa (4.20, left) shows a trough moving eastwards accompanied by a Rossby wave well visible on the 340 K surface (red PV contours) and a folded dynamical tropopause that covers a huge area. The cross section along the line A-B (4.20, right) shows the vertical structure of the fold at 90°E which lengthens far equatorward of the Tibetan Plateau. At this specific lontigud, the meridonal width of the fold measures more than 1600 km. Besides, the lapse rate tropical tropopause overlaps for an extended area the lapse rate extratropical tropopause (filled and unfilled black dots), pointing out a simultaneously large double tropopause event.

In the extratropics, the mean zonal and meridional distances are about the same order of magnitud, reflecting the more synoptic complexity of the flow at those latitudes. The extratropical tropopause folds, mainly associated with baroclinic cyclone activity, can also extend for few thousand kilometers along the local jet-traveling direction but, on the one hand, this flow is often not aligned with the zonal or meridional directions and therefore not measured as long in figures 4.18 and 4.19, and on the other hand, the jet-traveling directions can adopt many diferent orientations that absolutely can smooth out the mean values. Besides, the more wavy nature of the extratropical upper-level flow associated with tropopause folds limits the elongated folded areas along straight distances.

Finally, a global distribution of an estimation of the year mean area covered by

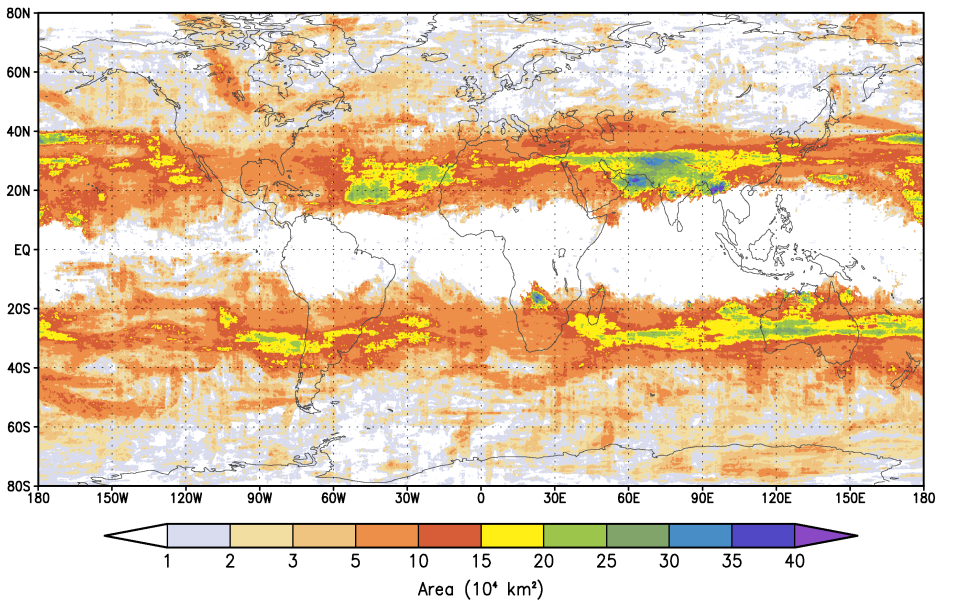

Figure 4.21: *Year mean spatial distribution of TF horizontal area (10^4 km^2), from one year of GFS analysis data (Dec 2007 - Nov 2008).*

tropopause fold structures, calculated from the zonal and meridional distances, is shown in figure 4.21. Although Bithell et al. (1999) showed that tropopause fold structures can be quite complex, an approximation is made assuming that the area projected by the fold on the horizontal plane forms an ellipse which its major and minor diameters are the zonal and the meridional distances. As expected, figure 4.21 highlights the mean features of figures 4.18 and 4.19, with mean area values ranging from about 70 thousend to more than 300 thousend square kilometers in the subtropics and from less than 10 thousend to short more than 100 thousend square kilometers in the extratropics. However, values in the extratropics may likely be quite conservative estimates for the above-mentioned reasons. They would probably be more ajusted if the distances along the jet-traveling and the jet-transvers directions had been used.

Chapter 5

10-year WRF Tropopause Fold Climatology

A regional tropopause fold climatology over Europe and derived from 10-year of WRF simulations is introduced in this chapter. First, seasonal and annual variability analyses with TF spatial distribution and preferred areas of tropopause fold formation are given and compared with other existent tropopause fold climatologies. It follows a climatological vertical and horizontal fold structure characterization with an analysis of the different geometric fold parameters. Finally, this section will end with a tropopause fold interannual variability examination.

5.1 Geographical Distribution and Seasonal Variability

Figure 5.1 displays the seasonal mean spatial distribution of tropopause fold frequency (in %) derived from the 10 years (1999-2008) of WRF simulations. It highlights seasonal variations of tropopause fold and favoured areas of TF formation within the model domain. The area of study comprises the East North Atlantic Ocean, the northernmost part of Africa, Europe and the Mediterranean Sea and Turkey, being the Iberian Peninsula nearly in the middle of the domain. To build up that regional tropopause fold climatology, in the same way as for the 1-year GFS analysis from the previous chapter, the geometric folding searching algorithm (detailed in section 3.3) has been applied at every 6-hour WRF output data over the 10 years. The result is a counting tropopause fold occurrence obtained at each grid point, along with other associated parameters recorded such as the intensity of the fold, its thickness, the horizontal extension, and the pressure gap between both 2PVU surfaces. The tropopause folding frequency is then computed by dividing the

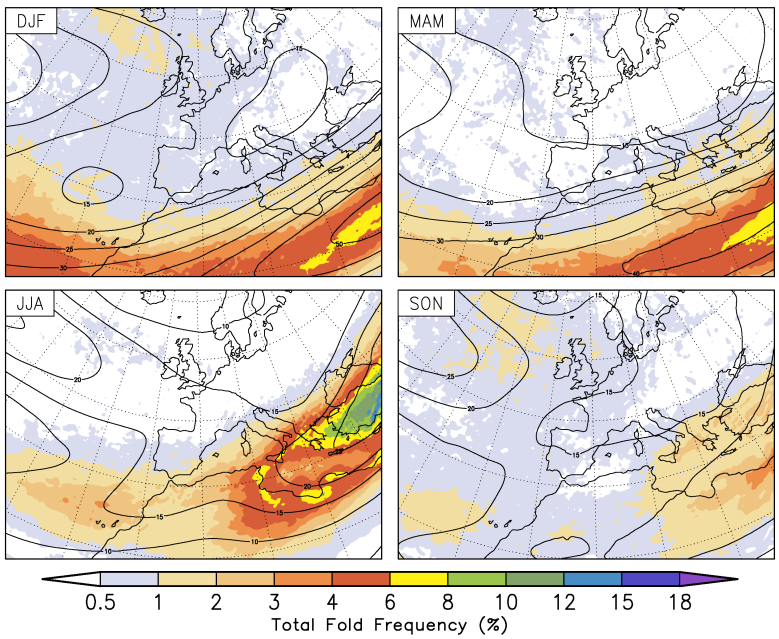

Figure 5.1: *Spatial fold frequency distribution (in %). Seasonal mean from 10 year (1999-2008) of WRF simulations. All four seasons are represented: DJF (top left), MAM (top right), JJA (bottom left) and SON (bottom right). Contours of the seasonal mean horizontal wind at 200 hPa from WRF analyses are superimposed with a 5 m/s wind interval (black contours).*

total amount of folds by the total amount of 6-hour time instances at each grid point. The seasonal mean horizontal wind structure at 200 hPa, obtained using horizontal wind WRF analyses (JRA data interpolated to the WRF grid configuration), is superimposed (black contours) and it agrees well with the climatological mean wind shown in other studies (Koch et al. 2005, Kunz et al. 2011, Schmidt et al. 2006) and the 1-year seasonal mean wind from GFS analysis observed in the previous chapter 4. The four seasons are shown in this figure and labeled accordingly: DJF (December, January, February), MAM (March, April, May), JJA (June, July, August) and SON (September, October, November).

During the winter months (left-top panel), the major activity of tropopause folds is centered in the southernmost part of the domain where a portion of the winter subtropical jet can be recognized. Maxima mean frequency values up to 6-8% are found along the subtropical jet axis core. Poleward of the jet, these frequencies decrease rapidly although still few tropopause fold activity can be found spread all over the higher latitudes. Maximum values (up to 2%) are located at the North Atlantic region, south of Iceland, coinciding with the end of the North Atlantic storm track region.

Moving into summer (left-bottom panel), the subtropical folding activity is displaced poleward following the seasonal displacement of the subtropical jet (Koch et al. 2005) and its higher values are mainly positioned over the eastern Mediterranean and Turkey, coinciding with the western edge of the high folding activity band associated with the asian monsoon anticyclone circulation that has observed within the GFS global analysis in chapter 4 (see figure 4.1b and discussion thereby). Maximum mean frequency values on that region range from about 8 to 15%, significantly higher values than during the winter season although the mean subtropical jet winds at 200 hPa are significantly lower. Noteworthy, an odd TF frequency depression can be observed over the eastern Mediterranean Sea with its minimum poleward of the Gulf of Sidra. This particular signature seems unrealistic and clearly disagrees with the continous TF frequency distribution depicted by the 1-year GFS analysis over that region. A deeper examination concerning this discrepancy will be address later in the next chapter 6. Besides, the extratropical activity decreases drastically nearly vanishing during that season, which is consistent with the summer depreciation of upper-level frontal systems at midlatitudes and the GFS distributions.

In spring, figure 5.1 (MAM) depicts a transition state from the winter to the summer situation: an important frequency decrease in the extratropical latitudes and an slightly east displacement from the winter subtropical structure. Especially interesting is the SON (right-bottom panel) situation. Extratropical folding activity in autoumn over the northern Atlantic area is comparable and even more extended than that of the winter, while the number of subtropical tropopause folds is considerably reduced in conjunction with a dissipation of the subtropical jet. Nevertheless, some summer remaining activity is still found over the eastern Mediterranean and Turkey, basically in September (shown later).

In general, these results derived from 10 years of WRF simulations are in line with other previous studies (Baray et al. 2000; Sprenger et al. 2003) and with the findings in chapter 4 undertaken with one year of global GFS analyses. However, although the seasonal geographical distributions and patterns are in really good agreement, some discrepancies in the maximum values can be observed. A more detailed 1-year TF frequency comparison between the GFS and the WRF simulation results is performed in the next chapter, section 6.1.

5.1.1 Intense and Deep Folds

As discussed previously in chapter 4, although extratropical tropopause folds are substantially less frequent than the subtropical ones, TF formation in the extratropics can have an important role in the atmosphere since the majority of these intrusions are intense and go deep into the troposphere. In the same way as for the

GFS analysis dataset, TF ocurrences have been classified according to their intensity and depth. Hence, the intensity is measured by the vertical distance (in hPa) between the upper and the middel tropopause crossing (the so called gap magnitude), and an "Intense Fold" is considered if that value is greater than 200 hPa. The depth, instead, is measured by the maximum penetration level of the intrusion (in hPa), and a TF occurrence in a grid point is classified as a "Deep Fold" if this depth magnitude is greater than 450 hPa. Next figure 5.2 shows the seasonal mean spatial distributions of Intense (5.2(a)) and Deep (5.2(b)) tropopause fold frequencies (in %) computed with the 10-years of WRF output data. The results are similar as those obtained with the GFS data (see section 4.1.3) over the considered region.

Although with significant lower values, the frequency ditribution for Intense folds (5.2(a)) shows the same pattern and seasonal variability as that shown by the totality of folds, except that in winter, spring and autumn, extratropical and subtropical frequencies are about the same order. In summer, Intense TF activity is reduced to the eastern Mediterranean area, where the highest frequencies can be found. Concerning Deep folds (5.2(b)), TF frequencies are substantially higher. In the extratropics, the seasonality and the geographical distribution is about the same as that observed for Intense cases, with a maximum in winter and a minimum in summer, while in the subtropics, Deep folds are more frequent in winter and strongly reduced during the rest of the year.

Compared to the total amount of fold frequencies, Intense and Deep folds in the subtropics show relatively low frequencies, while frequencies in the extratropics are about the same order of magnitude. To highlight this particularity, the ratios of Intense and Deep folds to the total amount of folds (in %) are displayed in figure 5.3 for two extended winter and summer seasons: from November to March and from May to September respectively. The ratios for Intense folds (5.3(a)), similarly as the results obtained with the GFS data (i.e. figure 4.6), range from 20 to 50% over the extratropics, while clearly lower ratios are found in the subtropics. Only the eastern Mediterranean area in summer, where maximum TF activity can be found, shows some subtropical Insense fold activity, with ratio values about 10-20%. Deep to total fold ratios (figure 5.3(b)) are even more clear. Percentages ranging from 50 to 90% can be observed in the entire extratropics, particularly in winter. Instead, the fraction of Deep TFs in the summer subtropics is even lower than that of Intense TFs. These ratios, obtained from 10 years of WRF simulations, further support the idea that the majority of extratropical TFs are stronger intrusions that go deeper into the troposphere, while subtropical TFs are in general shallower structures. However, few subtropical cases in summer may exhibit considerable large gap values (Intense cases), though the majority of them may present shallow depths of penetration.

Examining the area ratios of Intense and Deep TF areas to the total fold areas

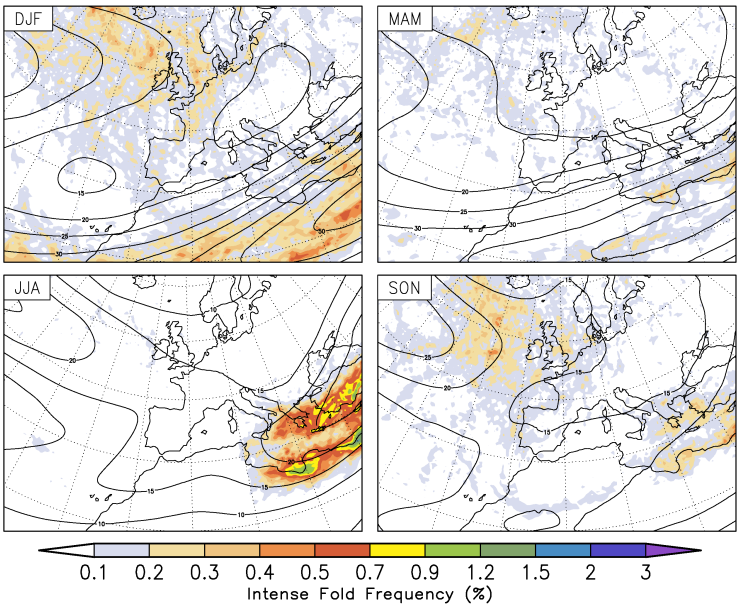

(a)

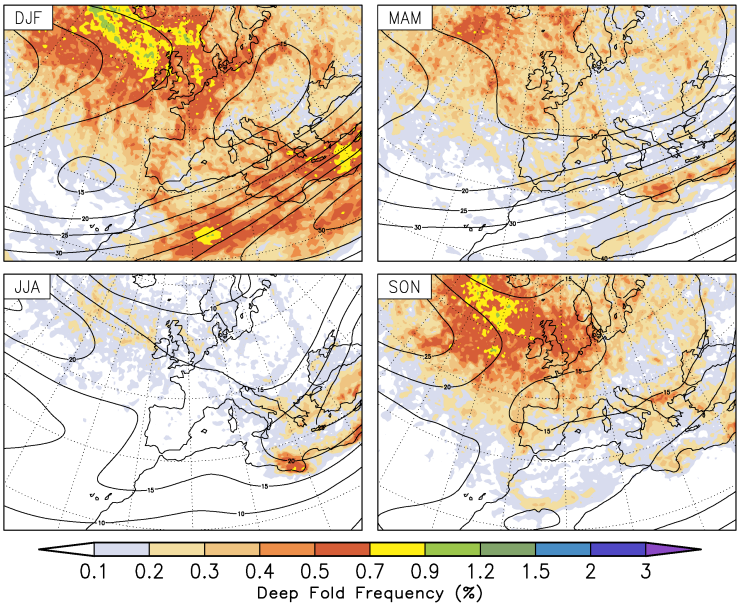

(b)

Figure 5.2: *Same as in figure 5.1 but for a) Intense Folds (gap ≥ 200 hPa) and b) Deep Folds (depth ≥ 450 hPa).*

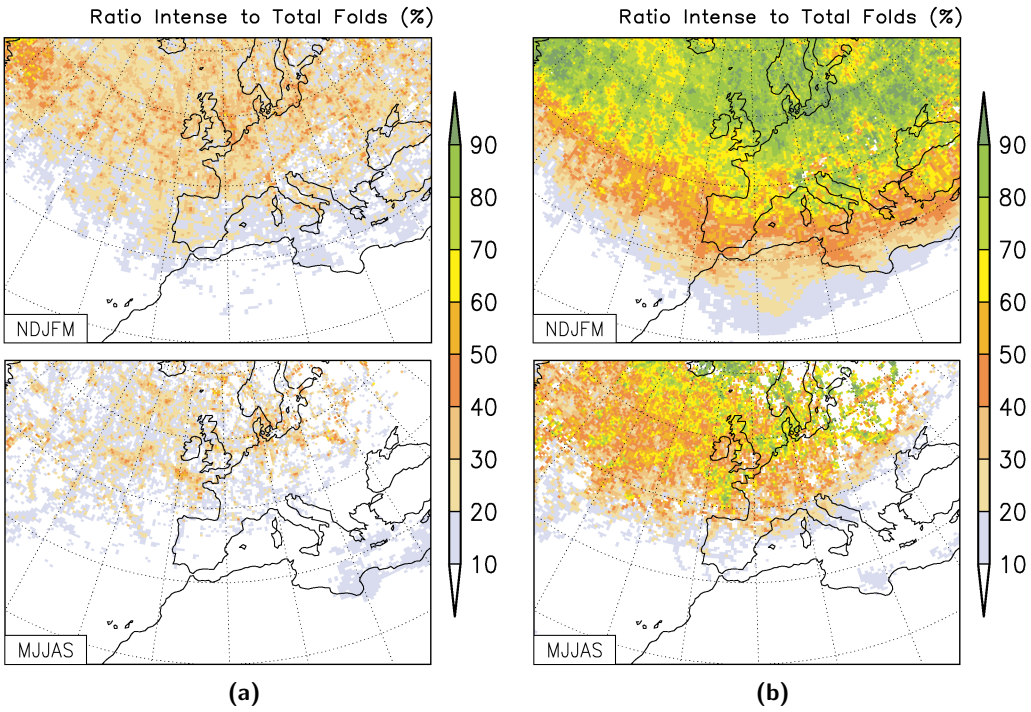

Figure 5.3: *Seasonal mean spatial distributions for the ratios of a) Intense folds (gap ≥ 200 hPa) to total fold occurrencies and b) Deep folds (depth ≥ 450 hPa) to total fold occurrencies (in %). Two extended winter and summer seasons are presented: from November to March (NDJFM) and from May to September (MJJAS).*

for few individual extratropical TF cases, as done within the GFS data in section 4.1.3, the results obtained are in line with the ratio percentages in figure 5.3. For example, considering a single extratropical Deep case, which covers a certain number of grid points, only a portion of these grid points will be counted and considered as deep while the rest will be counted as shallow or weak. A representative case taking place on February 3rd is displayed in figure 5.4, which shows the area covered by the tropopause fold. The blue region within the entire fold area portrays in (a) the area detected as Intense (gap ≥ 200 hPa) and in (b) the area detected as Deep (depth ≥ 450 hPa). Both area ratios obtained of 0.22 and 0.49 respectively are found within the ranges of their respective ratio percentages in the DJF plots from figure 5.3.

That particular event is the same that has been analyzed in section 4.1.3 (see figure 4.7, left). A simple comparison reveals that the area shaded by the fold presence is significantly lower for the WRF simulation data than for the GFS analysis. The same applies to the Intense and Deep area ratios and the ratio percentages to total fold occurrences. Likewise, figure 5.5 shows the vertical profile along the segment AB in figure 5.4 and, compared to the same GFS vertical profile (4.7, right),

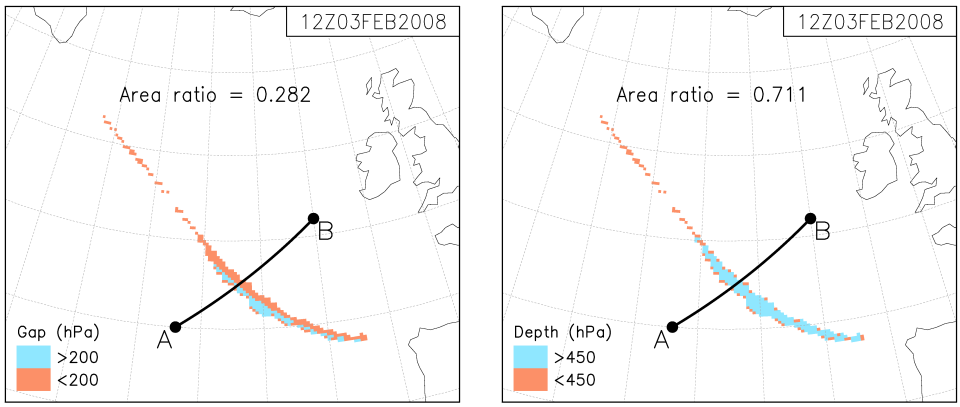

Figure 5.4: *Intense tropopause fold event on 3 February 2008 at 12 UTC over the North Atlantic Ocean. Left: gap magnitude of the folded 2 PVU surface area and ratio of gap ≥ 200 hPa area to total folded area. Rigth: depth magnitude of the folded 2 PVU surface area and ratio of depth ≥ 450 hPa area to total folded area. WRF simulations*

it can be noted that the fold generated by the WRF model has a significant shorter zonal width extension and, in general, smaller dimension characteristics. This will be further examined later in chapter 6, where a more detailed investigation about how well the WRF is able to generate tropopause folds and an assessment of its strengths and weaknesses will be done.

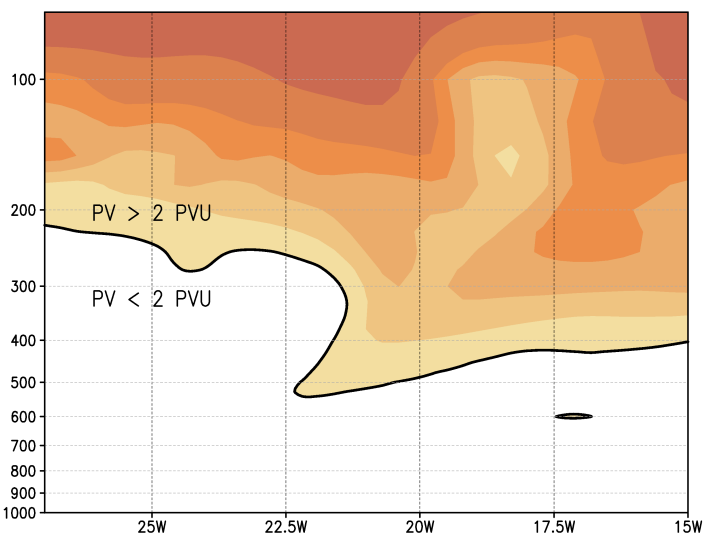

Figure 5.5: *Vertical cross section of potential vorticity (PVU) across the segment A-B from figure 5.4. WRF Simulations*

Back to figure 5.2, higher frequencies are detected in the extratropics with the Deep category compare to the Intense one. This can be easily explain as a consequence of the typical TF shapes and in the manner in which these two different parameters have been defined. The vertical profile from figure 5.5 shows a typical fold section where, along the segment AB, the totality of the intrusion (the lowest 2 PVU surface) is above the 450 hPa (deeper into the troposphere), while only a portion of it presents gap values greater than 200 hPa. In the subtropics this does not always apply. Particularly in summer, lower Deep than Intense frequencies are detected in the subtropics, where, as mentioned before, some few cases happening at higher altitudes and intruding little into the troposphere may present significant gap values. In winter, the region that expanse from the central of Algeria to the eastern Mediterranean Sea, depicts significantly higher Deep Fold frequencies than Intense Fold frequencies, as it happens in extratropical regions. The analougous GFS images (4.5(a) and 4.8(a)), show the same behaviour in that area, and also along other strong wind gradient regions just on the poleward site of the winter subtropical jet maxima (i.e. South Korea and southern Japan), which suggests those particular subtropical cases may have a similar dynamical development as the extratropical TF formation. The vertical and the horizontal TF characteristics with their geographical distributions are investigated in more detail later in the chapter (section 5.2).

5.1.2 The Annual Cycle

The monthly mean annual variability of the areal average of the total amount of fold occurrences computed within the region of the WRF model domain (22°N-66°N and 37°W-32°E) for the 10 years of data is shown in figure 5.6 (black line). The annual cycle exhibits a well-defined seasonal variability with the biggest TF activity in winter (February and March) and summer (June and July) and the lowest in spring (April and May) and autumn (November). Error bars show the standard deviation around the 10 year monthly mean and they indicate at first glance significant interannual variability during the winter months of December, January, February and March and a narrower spread otherwise.

Besides, two other annual cycles for two different collections of data sets named "Subtropical Sample" (orange line) and "Extratropical Sample" (blue line) are displayed in the same graph. To set up these two different samples, a simple latitude distinction is made according to the latitudinal distributions show in figure 5.7. It displays 12 plots, one for each month, with the 10-years monthly mean latitudinal distributions of the zonal mean number of tropopause folds within the WRF model domain longitudes from 37°W to 32°E. The distributions reveal a distinct subtropical maximum, located at around 25°N in winter and spring and clearly poleward

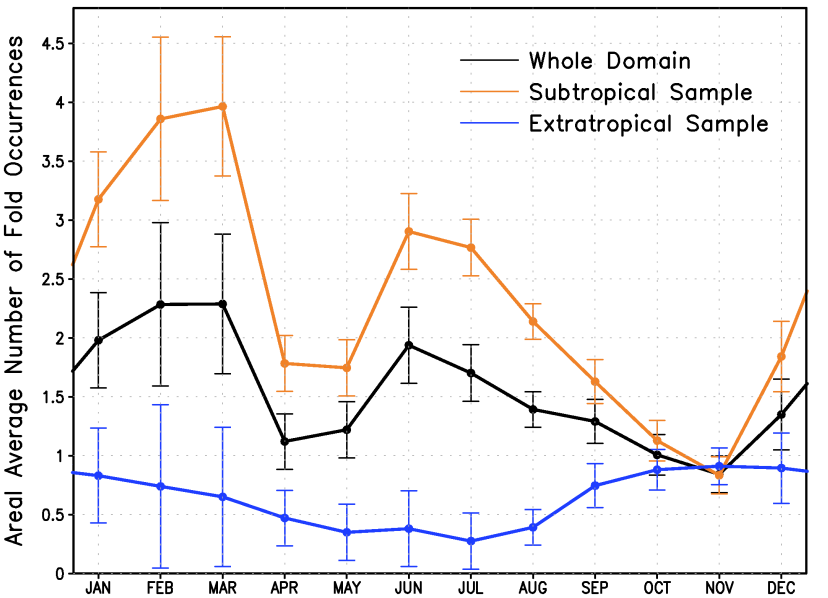

Figure 5.6: *Annual cycle of the areal average of the number of fold occurrences. Monthly mean from 10 years (1999-2008) of WRF simulations. Black solid line includes fold occurrences for the "Whole Domain" (37° W-32° E and 22° N-66° N). Two other lines for two different groups are also drawn: "Subtropical Sample" (orange) and "Extratropical Sample" (blue). The latitude interval of the areal average for each group varies depending on the month (see next figure 5.7).*

(between 30°N and 40°N) during the summer months and September. The only exceptions to that picture take place in October and November when the subtropical maximum becomes pretty smoothed and even overcomed by an extratopical maximum in November. At higher latitudes, in fact, the distributions are flatter although distinguishable shy maxima are still visible from November to March. Based upon these considerations, which suggests a distinc annual behavior between the extratropics and the subtropics, different latitudes intervals have been chosen for each specific month to build up both different "Subtropical" and "Extratropical" samples. They are indicated, respectively, by the orange and blue boxes in figure 5.7. As the area regions used are different for the different months, in order to ensure a reliable comparison between months within the annual cycle, the areal average of the number of tropopause fold ocurrences[1] has been preferred in front absolute mean values.

As suggested previously and observed in chapter 4 within the global GFS data, it can be identified two different annual behaviors of TF formation: one for the subtropical region with TF formation mainly associated to the subtropical jet stream,

[1]That is the average number of tropopause fold ocurrences per unit area.

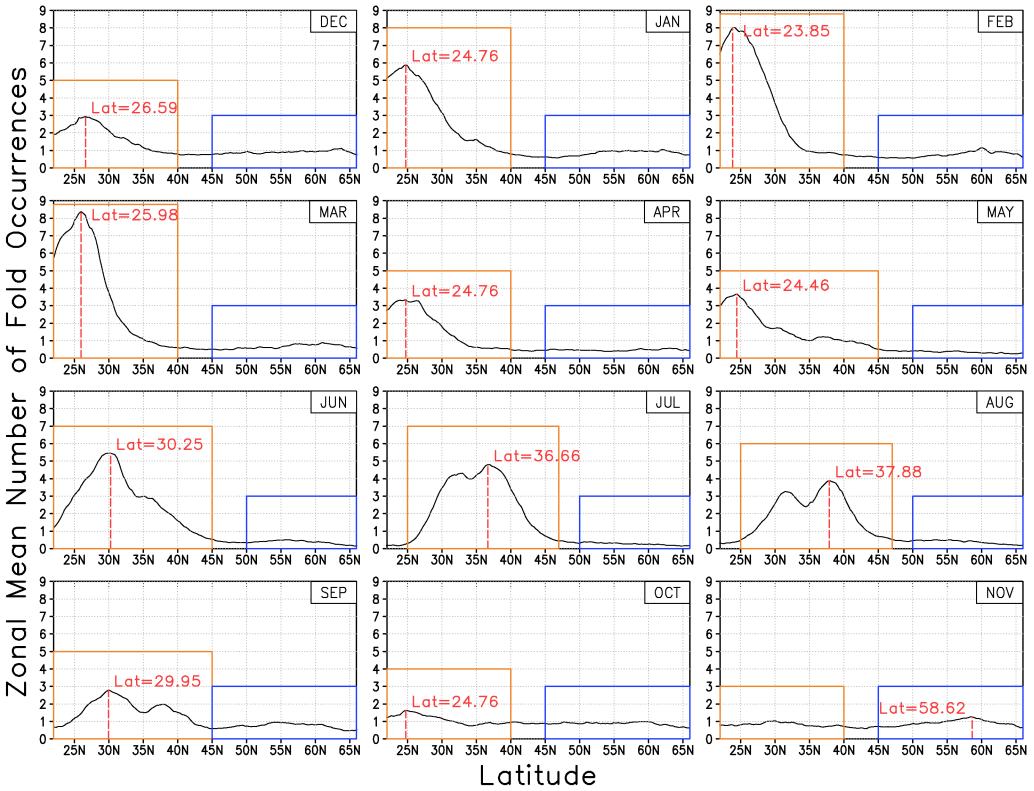

Figure 5.7: *Monthly mean latitudinal distributions of the zonal mean number of fold occurrences. Monthly mean from 10 years (1999-2008) of WRF simulations. In red is shown the latitude where the maximum is found. The orange and blue boxes show the latitude interval chosen for each month to compute the areal average of the number of fold occurrences for the two different groups, "Subtropical Sample" and "Extratropical Sample".*

and the other one for the extratropical tropopause folds associated to mid-latitude cyclone activity and upper-level fronts.

As expected, the "Subtropical Sample" shows a similar behavior to that of the whole domain since the areal mean of TF ocurrences for the whole domain is in general dominated by the high values of subtropical TF occurrences and just merely attenuated by the low extratropical values. Thus, the highest TF activity is found during the winter months of January, February and March. Besides, the distributions from figure 5.7 show a fairly localized activity in a zonal belt centered at around the 25°N. Unfortunately, this is too close to the southern limit of the model domain and thus, to the sourthern limit of the subtropical region considered for the areal average. The curves in figure 5.7 for these particular months and also the spatial fold frequency distributions in figure 5.1 (DJF and MAM) further evidence as a portion

of the winter subtropical TF activity is found outside of the domain, equatorward of 22°N, and that may sligthly overstimate the subtropical areal average between the considerate longitudes. In addition, that portion may vary depending on the year and the latitudinal position of the maximum subtropical TF activity or, in other words, on the latitude location of the subtropical jet core. Little variations on that location may lead to important interannual variability within the domain of study and it could be one of the reasons for the high stardard deviation values over January, February and March along the "Subtropical Sample".

Later in April and May, sutropical folding activity shrinks to approximately half of its winter value, and then raise again in summer to a second maximum, particularly strong during June and July. Examining the curves in figure 5.7 for these months, aside from the poleward displacement, it can be ovserved an expansion of the distribution curves and an enlargement of the latitude band of subtropical TF formation. Besides, a peculiar decrease of the zonal mean number of fold ocurrences is evident during June, July, August and September at around 35 degrees North, depicting an odd double peak in curves. It precisely coincides with the latitude where a TF frequency depression can be observed over the eastern Mediterranean Sea in summer (see figure 5.1, JJA). These kind of bites on the distributions do not resemble realistic and suggest again the WRF model is most likely not performing properly over that specific region.

Finally in autumn, subtropical tropopause fold activity decreases noteworthy until its year minimum in November where, as it has already been noted, it falls even below the extratropical activity value.

The annual cycle for the "Extratropical Sample" (blue line in fig. 5.6) shows a different scenario. Just two seasons can be identified in that case. On the one hand, a relatively busy season is observed from September to February-March with its maximum activity in November. During that period, althought the latitudinal zonal mean distributions from figure 5.7 show that tropopause fold formation occurre at somewhat uniformly along the entire mid-latitudes, yet a slight preference for a major activity is observed between 55°N and 65°N, except in September where the modest maximum is located slightly equatorward of 55°N. On the other hand, a quite inactive season is observed from April to August with its minimum activity in July.

Next figure 5.8 exhibits similar annual cycles but accounting only for the deepest instrusions. Therefore, the black line depicts the 10-year mean annual variability of the areal average of Deep tropopause folds considering the whole domain, and the orange and blue lines, the equivalent for the respective "Subtropical" and "Extratropical Samples", which have been stablished by the same monthly latitude intervals used in figure 5.6 (orange and blue latitudinal boxes from figure 5.7). Deep folds

in the extratropics are the ones that display the strongest annual cycle, with the major activity in November, December and January, and the minimum in July and August. In fact, extratropical Deep annual variations are very much alike the extratropical annual variations of total folds, except for the absolute mean values which have approximately halved. Subtropical Deep folds, as seen in section above, are less common. Their maximum activity is found in the winter months from December to February, with a peak in January. From April to October, subtropical Deep tropopause folds are almost non-existent.

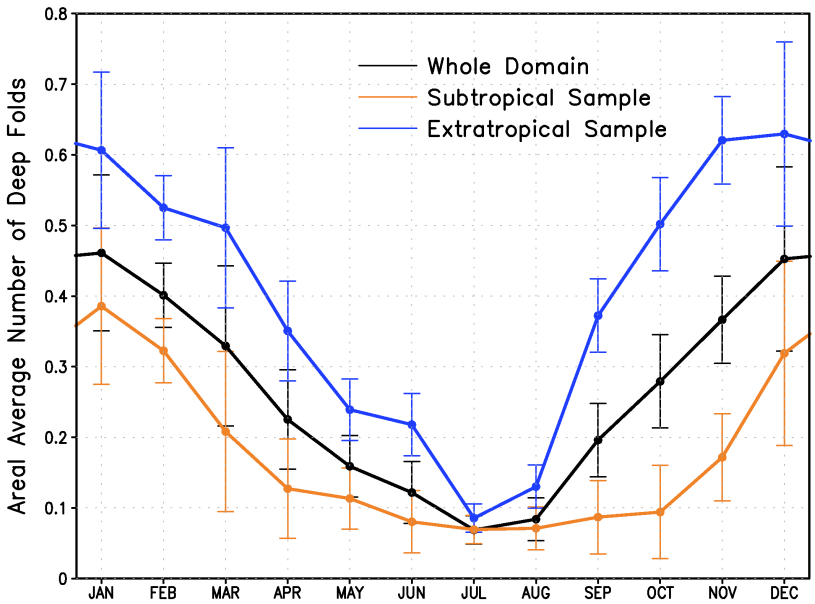

Figure 5.8: *Same as in figure 5.6 but for Deep Folds (depth ≥ 450 hPa).*

Analogously, the latitudinal zonal mean distributions of the number of Deep fold occurrences for each month are shown in figure 5.9. The dashed red lines indicate the latitude where the zonal mean maximum is detected. They highlight a completely different picture from that of the total folds (see figure 5.7). Aside of being an order of magnitude lower, the majority of Deep folds occur in the mid-latitudes, poleward of 50°N. As already mentioned, only in winter, slightly enhanced activity can be found over the lower subtropical latitudes.

These seasonal cycles are consistent with the annual variations found in chapter 4 with the GFS dataset and with those reported by Sprenger et al. (2003), using in both cases the same technique based on the 2 PVU surface geometry to identify tropopause folds over 1-year of global meteorological analyses. The main discrepancy is the summer maximum found through the "Subtropical Sample" for the total fold occurrencies, where minimum tropopause fold activity is found on an hemispherically

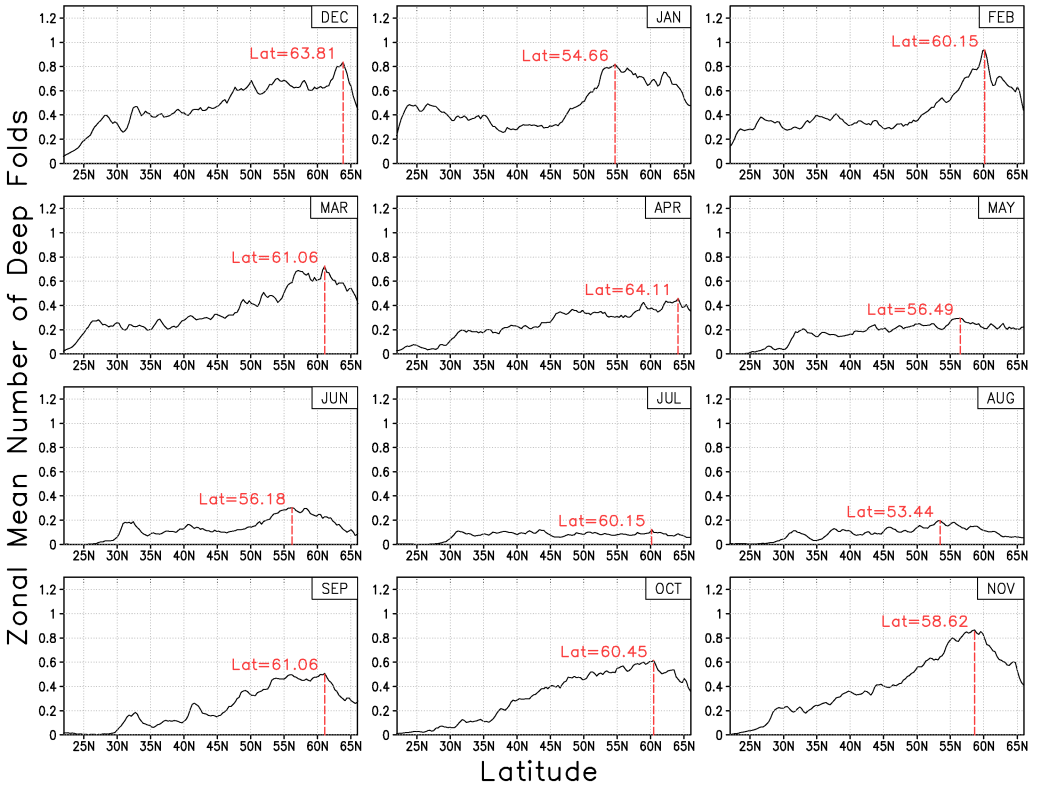

Figure 5.9: *Same as in figure 5.7 but for Deep Folds (depth ≥ 450 hPa).*

average. This can be easily explained by the observed geographical variability shown by the GFS data analysis. The domain of the present regional climatology includes a portion of the northern hemisphere where subtropical TF activity is relatively important in summer, not being like this in other areas (i.e. see and compare figures 5.1 and 4.1).

Besides, similar annual distributions in two different european local areas are found by Rao et al. (2008) and Antonescu et al. (2013), respectively an 11-year (1997-2007) and a 5-year (2006-2010) folding climatology studies, both constructed with a folding detection algorithm from VHF radar data. In the first case, the radar is located at the Artic station of Esrange (north of Scandinavia) at a latitude around 67°N. The second climatology completed by Antonescu et al. states for the region of Wales in the UK, with the radar located at Capel Dewi (52°N), a region inside our extratropical sample.

5.2 Vertical and Horizontal TF Characterization

In a similar way as for the global 1-year GFS data study in section 4.2, the geometric tropopause fold characteristics are examined in this section for the 10 years of tropopause folds simulated with the WRF model. A more detailed seasonal and regional evaluation is presented in this case. Different regions and different seasons present different fold characteristics. The five different geometric quantities that define the vertical and the horizontal extent of tropopause folds are the depth, the gap, the thickness, the zonal width and the meridional width (see subsection 3.3.2 in chapter 3). First, the vertical properties of depth, gap and thickness are analyzed. They provide information about the penetration intensity of intrusions and a qualitative estimate of the amount of mass that is likely irreversible transferred from the strastophere to the troposphere. Finally, the horizontal width distances that tropopause folds can attein and an estimation of their horizontal expanse are examined at the end of the section.

5.2.1 Vertical structure

Figure 5.10 shows the geographical distributions of the 10-year mean fold depth. Grid points with less than 5 tropopause fold cases during the ten years and the considered season have been omitted to avoid possible misleading mean values. The distributions agree well with the results in chapter 4 from the global GFS data. The deepest instrusions are found in the extratropics and during winter and spring seasons, consistent with the findings of Bush and Peltier (1994), who related a larger depth of fold penetration with a stronger main state baroclinicity. Instead, in the subtropics the penetration intensity is weaker in all four seasons, and specially in summer that exhibits the smallest mean values, which extend to the summer higher subtropical latitudes.

That way, the preferred regions for the strongest TF formation are detected over the northeastern and the northwesternmost parts of the North Atlantic Ocean, the North Sea and the eastern Russia during the winter season, where mean values higher than 600 hPa can be observed. In spring, these values are found more spread over the entire northern North Atlantic and into the Norwegian Sea, and also in the southern tip of Sweden. It is also noteworthy to mention a band that extens from the Bay of Biscay along the northern Mediterranean area to Turkey in winter which displays relatively high mean depths values ranging about 450-575 hPa, particularly over the Adriatic Sea.

The following figure 5.11 displays the same geographical distribution for the mean gap magnitude. It can be observed as both gap and depth distributions correlate

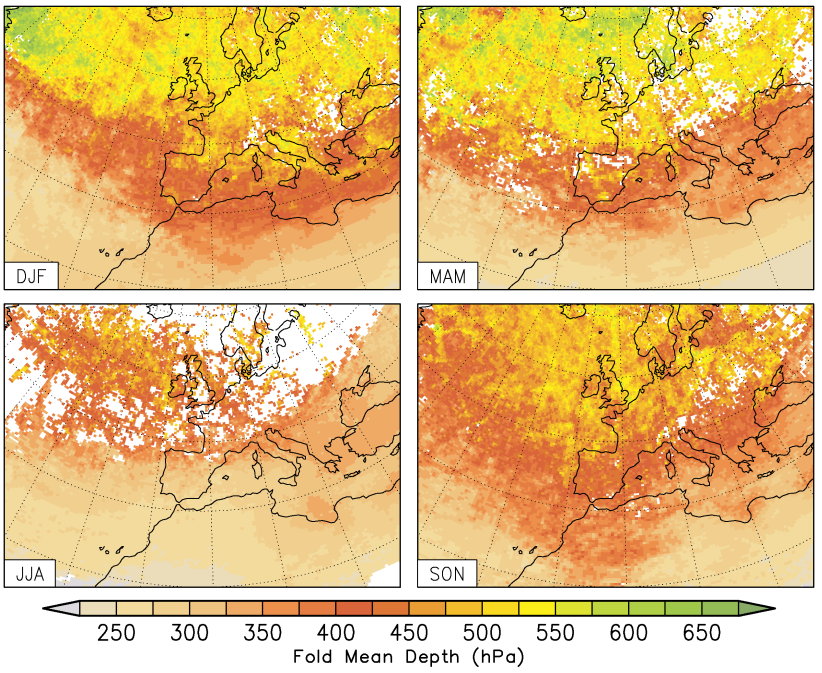

Figure 5.10: *10-year Seasonal mean spatial distribution of tropopause fold depth value (hPa) from WRF simulation data.*

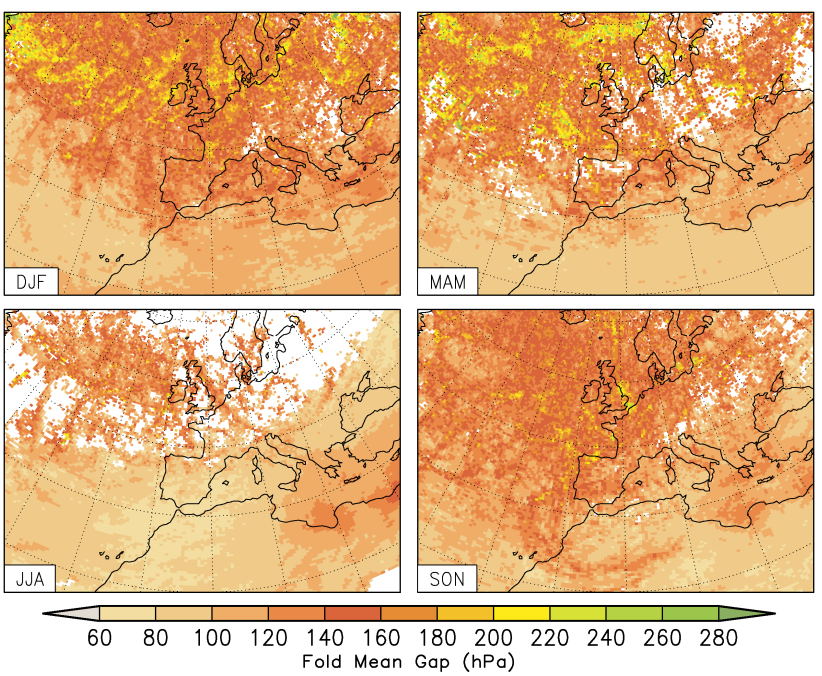

Figure 5.11: *Same as figure 5.10 but for the tropopause fold gap value (hPa).*

to a large degree, which seems a reasonable picture since a big gap implies a big depth of penetration. However, the linkage is more complex as other variables can be involved such as the thickness and the level of the upper 2 PVU boundary. A singular situation, for instance, is clearly visible over the southeastern Mediterranean area in summer where comparable extratropical mean gap values up to 140 hPa are found, whereas relatively shallower mean depths - with maxima around 325 hPa - are present. This sort of conditions were also observed in different subtropical places over the globe in chapter 4 (see figures 4.12 and 4.13 and explanations thereby). Following then that previous interpretation, accompanied with the conceptual model of figure 4.14, the combination of an intense gap and a relatively shallow depth is possible if the upper 2 PVU boundary of the fold is locally anomalously high. The only other option would be to have exclusive pretty thin folds over that region. However, the mean thickness geographical distribution of figure 5.13 discards this possibility. Instead, it highlights significant mean thickness values in summer over that region, what further reinforces the previous scheme of an anomalous high tropical tropopause.

Besides, scatter plots evaluating the gap and the depth relationship of each individual TF occurrence, and coloured by their latitude location, have been examined for the different months. Apart from the gap, depth and latitude interrelation, they offer good detail of typical gaps and depths beyond the smoothed averaged values seen so far. The 10-year Januaries and Julies, characterizing the winter and the summer situation respectively, are shown in figure 5.12. Two black lines separate each phase space in four quadrants depending on gap values lower of bigger than 200 hPa and depth values lower of bigger than 450 hPa.

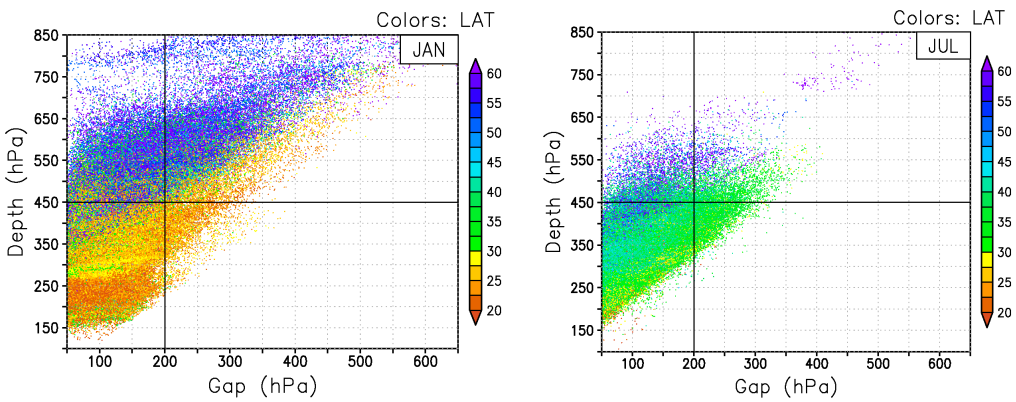

Figure 5.12: *Scatter plots of the Gap and the Depth tropopause fold features for the 10-year Januaries (left) and the 10-year Julies (right). Coulored by 2.5° latitude intervals. From WRF simulations.*

Both plots reinforce most of the characteristics observed so far, and TF differences

between both seasons are clearly visible. In July, the majority of TF cases are found below the 450 hPa line and equatorward of 40-45°N. June and August (not shown) show a pretty similar picture, although in June few intense cases are detected at higher latitudes. The strongest instrusions, with several reaching the 850 hPa, are mainly detected in the winter extratropics. Additionally, relatively deep TF are also observed among subtropical latitudes during this season. Spring and autumn months (not show) diplay a similar picture to that of the winter, although intense cases are more confined into the extratropics and they do not usually reach depths as deep.

Finally, the thickness magnitude above mentioned is the remaining variable to conclude the vertical structure characterization of TF. The geographical distribution of its seasonal mean, shown in figure 5.13, highlights that the biggest thicknesses are found during winter. During that particular season, the locations that show the larger values (about 100 hPa or even larger) are the northwestern North Atlantic Ocean, western Russia, the southern tip of Sweden and different spots around the Mediterranean area: Turky, the northernmost part of Algeria, the northeasternmost part of Spain and the area that comprises Italy, the Adriatic Sea and the western Balkan Coast. In spring, the extratropics are assorted with a great variety of mean values spread all around. South of 40°N, the mean values are a bit lower compare to the winter situation. And those are even lower in summer, except over the Gulf of Sidra in Libya and the region that comprises Turkey, the Black Sea and the Balkan Peninsula. In autoumn, the main spots identified are the Gulf of Sidra, north of Spain, northeastern Germany and Poland, and the northwesternmost part of the North Atlantic Ocean.

As explained previously (section 4.2.1), the thickness measures the vertical width of the stratrospheric tongue intruding into de troposphere, and although it can give an estimate of the amount of stratospheric air involved in a folding process (Wimmers and Moody 2004b), it is difficult to know accurately the portion of that air that will irreversible remain in the troposphere since that is strong related to diabatic processes and small-scale turbulences. However, assuming that in deep intrusions the irreversibility is more probable and the Stratrosphere-Troposphere Transport (STT) more effective (Bithell et al. 1999), a product named STT Folding Index (STTFI) has been performed, same as that used with the global GFS data in chapter 4 (see figures 4.17a to 4.17d and explanations thereby). It combines the thickness, the depth and the frequency of ocurrence to offer a qualitative notion of the regions that are more likely to be affected by the biggest amounts of irreversible stratrosphere-troposphere transport due to deep tropopause fold processes. The seasonal mean geographical distribution of the STT Folding Index, which for one year of global GFS data showed really good agreement with the different global STT climatology studies, is shown in figure 5.14 for the 10 years of WRF output data.

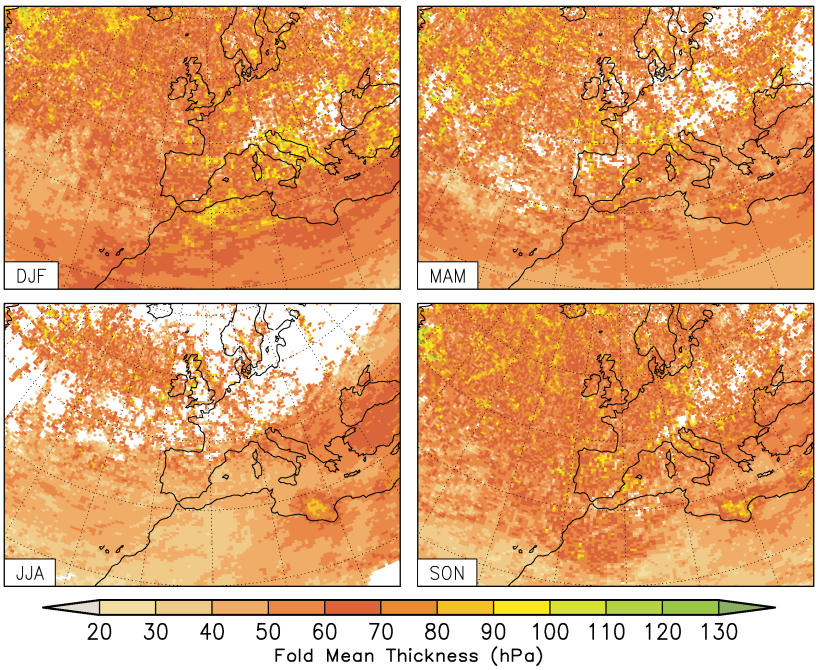

Figure 5.13: *Same as figure 5.10 but for the tropopause fold thickness value (hPa).*

It highlights that the major transferences of mass happen during winter and autumn, particularly in winter, while in summer, transport activity is in a very low level state, although the major peak of tropopause fold frequency happens in this season. During winter, the main regions that are likely to suffer the major stratospheric air intrusions are the northern North Atlantic where it highlights the region that extends from the southeast of the Greenland Sea to the British Islands Coast and the Norway Coast, the North Sea with a little tongue that lengthens south into the continent over the Netherlands, Belgium and France, the northern Africa Continent particularly over Central Algeria, and the eastern Mediterranean Sea with its maximum around 30°W. Also a little activity can be observed on the South Baltic Sea and its surrounding coast, East Ukraine and Russia, the Bay of Biscay, the southwest of the Iberian Peninsula and its surrounding ocean, and the Adriatic Sea and the eastern Mediterranean Sea. Also in autumn the distributions reveal significant transports that, in that case, are basically reduced to the northern latitudes (above 45°N) between 45°W and 10°E. Outside that area, only few little evidences are found in localized places such as over Greece and the surrounding areas or the western coast of the Iberian Peninsula. Moving into spring, the distribution shows a similar pattern as that of the winter situation although notably attenuated. And finally during summer, as mentioned above, the SST Folding Index traces are almost nonexistent among the majority of the domain, only few signs are present

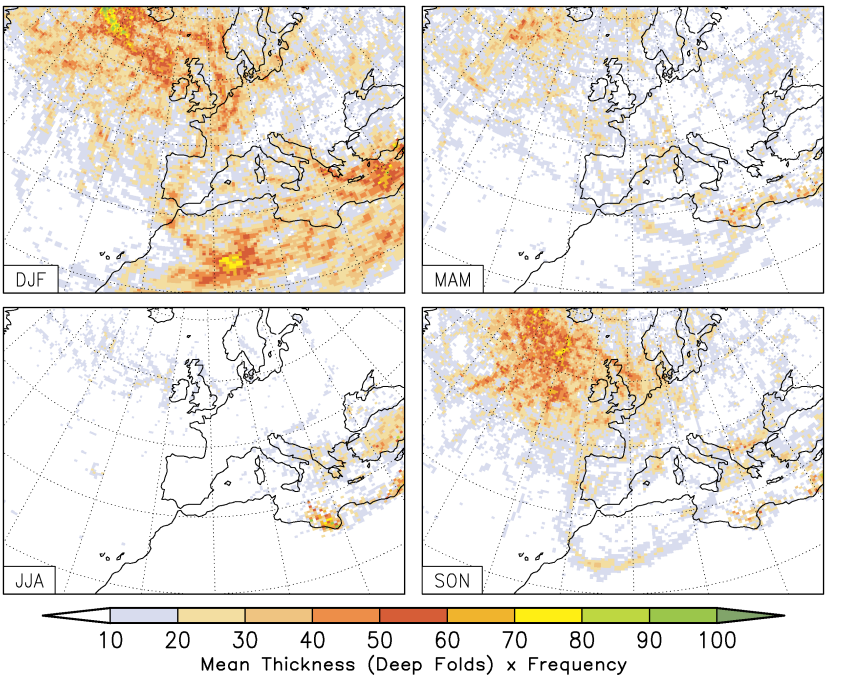

Figure 5.14: *Same as figure 5.10 but for the STT Folding Index.*

on the eastern Mediterranean area such as the eastern Gulf of Sidra or Turkey.

5.2.2 Horizontal structure

In order to examine the horizontal properties of TF, the two perpendicular distances (in km) along the x and y grid coordinates of the horizontal projection of the tongue intrusion have been computed. In a similar way as for the GFS data, the TF searching algorithm registers the zonal and the meridional widths at each grid point where a TF is identified. However, a discrepancy has to be considered herein. Due to the calculation procedure of those distances (see section 3.3.2) and because of in a LCC projection grid, which is the WRF horizontal projection used, the x and y grid coordinates may not always coincide with the longitude and latitude coordinates, the computed distances may not exactly correspond to the zonal and the meridional distances as it occurs with the GFS lat/lon grid. In the present case, the further from the center of the domain, the more the discrepancy. Nevertheless, for a general overview and in a first approach, the differences are not of great relevance and both magnitudes will be treated as the zonal and the meridional widths, although they will be mark with an asterisk to remind that singularity hereafter.

Figures 5.15 and 5.16 show respectively the distributions of the seasonal mean

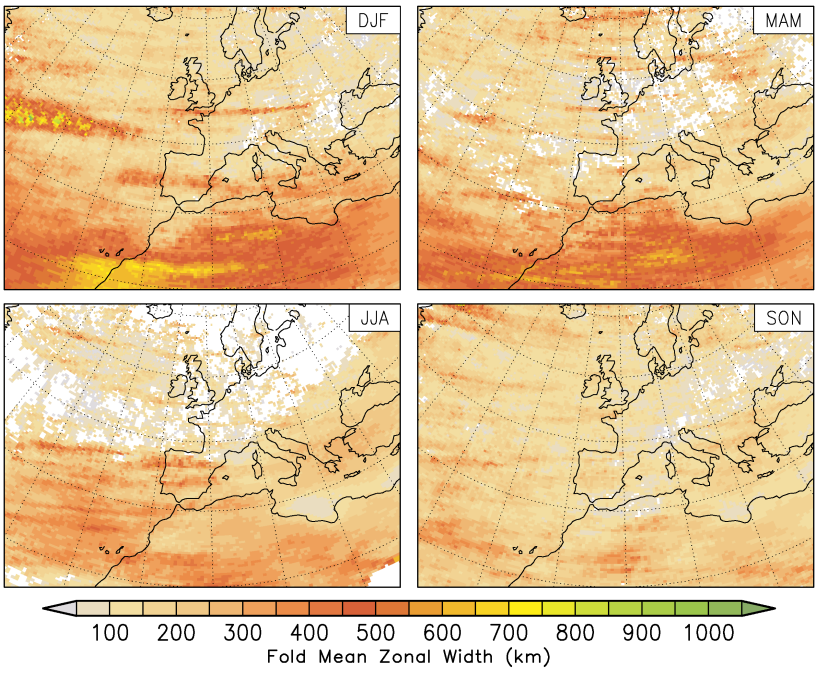

Figure 5.15: *10-year Seasonal mean spatial distribution of tropopause fold zonal* width (km) from WRF simulation data.*

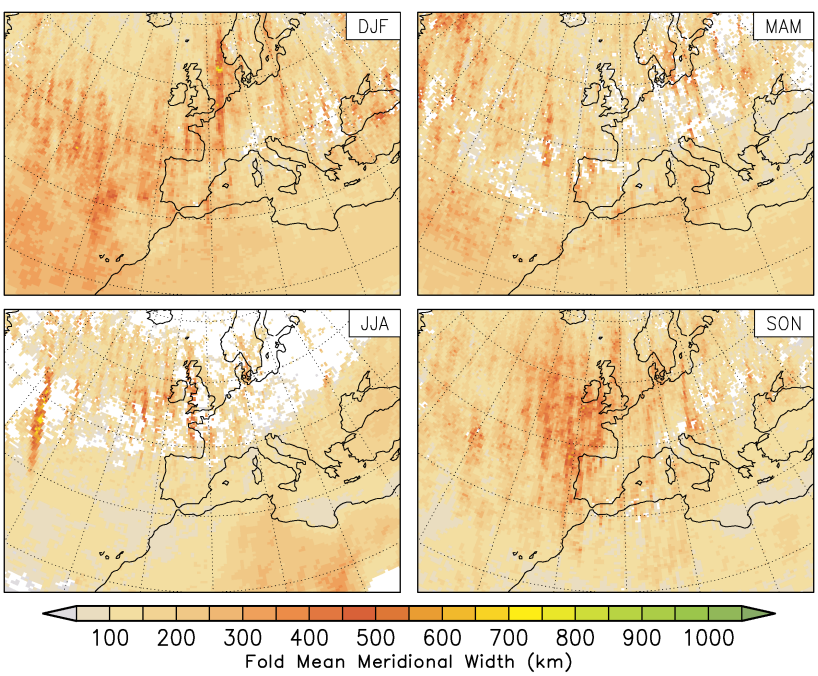

Figure 5.16: *Same as figure 5.15 but for the fold meridional* width (km).*

zonal* and meridional* width distances. As expected after the analogous GFS analysis (see section 4.2.2), the subtropics display large zonal* mean distances during winter, spring and autumn, particularly in winter where maximum values up to 750 km are observed along a region that extends from south of the Canary Islands, through Western Sahara and to Algeria. Further to the east edge of the domain, relatively lower values can be observed, probably because the limited area domain prevents the algorithm from detecting if fold structures continue farther east.

Besides, the subtropical meridional* mean distances are much lower, ranging from less than 100 km to not much than 350 km. The minimum values are registered during summer and autumn. Noteworthy is a peculiar depression observed, for both magnitudes, over the Gulf of Sidra during these two seasons and particularly in summer.

In the extratropics, in contrast, both distances are about the same dimensions, with larger of smaller mean values depending on the specific area and season. In winter, the largest zonal* mean values are found over the North Atlantic Ocean around 40°N, over a band crossing the Iberian Peninsula at about the same latitude, and over a thin belt crossing the west european continent at around 50°N. In spring, these maxima are position further poleward over the Norwegian Sea and surroundings, and in autumn, they are mainly localized over the northwesternmost part of the nortern North Atlantic area. With regard to the extratropical meridional* mean distances, the larger values are observed during winter and autumn. In the latter season, these are mainly found between longitudes 20°W and the Prime Meridian, while in winter, maxima are more extended over the central North Atlantic, the southwest of the european continent and the North Sea.

In general terms, both mean values observed and their geographical distributions agree to a high degree with those observed for a one year analysis with the GFS data over the considered region (see figures 4.18 and 4.19).

Lastly, the area projected on the horizontal plane by tropopause folds has been computed assuming that they form an ellipse with the major and the minor distances given by the zonal* and the meridional* widths, and its seasonal mean geographical distribution is shown in figure 5.17.

The most significant features of the seasonal mean horizontal area distributions clearly match the main peculiarities of figures 5.15 and 5.16, as expected. Thus, the greatest values are found in the subtropics where they range from about 20 thousend square kilometers in autumn to more than 200 thousend square kilometers in winter. In the extratropics, significant lower values are observed, ranging from less than 20 thousend to short more than 100 thousend square kilometers, with the exception of a band over the North Atlantic Ocean around 40-45°N in winter where

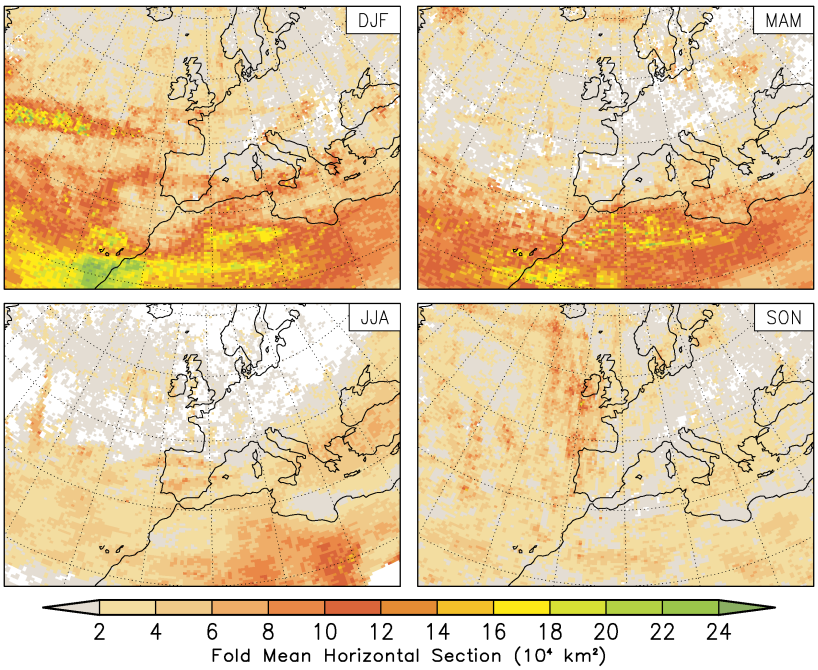

Figure 5.17: *Same as figure 5.15 but for the fold mean horizontal section ($10^4 km^2$).*

mean area values greater than 200 thousend square kilometers can be observed. These results, however, are a coarse estimation. On the one hand, the ellipse shape assumption may not always be accurate anough since TF structures can be quite complex (Bithell et al. 1999). On the other hand, if the zonal* and the meridional* width distances does not coincide with the jet-traveling and jet-transvers directions, the computed horizontal section may be quite conservative since none of the two distances is probably able to record the real jet-traveling dimension, usually the largest one (see section 4.2.2). Consequently, the TF area results are likely to be significantly understimated in the extratropics, where tropopause folds adopt quite frequently many different orientations compare to the more zonal aligment of subtropical fold structures, due to the more complexity of the synoptic extratropical flow.

Chapter 6

Capacity of the WRF model in TF performance

In this chapter, the skills of the WRF model to simulate and characterize TF are analyzed. The aim is to evaluate, from both qualitative and quantitative points of view, the model ability to develop and predict such structures and the improvement achieved by modelling the tropopause with a regional model including a generous vertical and horizontal resolution refinement. To accomplish this, meteorological variables on the dynamical tropopause (Tropopause Maps) and different tropopause fold magnitudes derived from the WRF outputs have been compared with the GFS T382 analyses and the WRF analyses, which in fact consist of the Japanese ReAnalysis (JRA) used to initialized the WRF model. Both GFS and JRA contain valuable observational and satellite data assimilations, though the former dataset has a similar horizontal and vertical resolution as that of the WRF simulations performed while the latter data grid is much coarser.

First, from a climatological point of view, the seasonal TF frequencies obtained for one year of data (December 2007 to November 2008) with the TF searching algorithm from the three different sets of data are qualitatively compared and analyzed over the WRF model domain region. Ensuing, individual TF cases are examined, and the most relevant from both winter and summer seasons are presented here. Finally, a more quantitative comparison in given at the end of the chapter.

6.1 TF climatology comparisons

In this section, a comparison between JRA, WRF simulation and GFS analysis TF frequencies is provided. To allow consistent comparisons, daily data at only 12 UTC

over the entire year December 2007 to November 2008 has been considered in all three data sets to derive the TF frequencies over the study area (the WRF model domain). The next three figures (6.1, 6.2 and 6.3) show, therefore, the seasonal geographical fold frequency distributions computed respectively from the WRF analyses (JRA interpolated to the WRF model grid), the WRF simulations and the GFS analyses. Besides, the climatological horizontal mean winds at 200 hPa are superimposed in black contours.

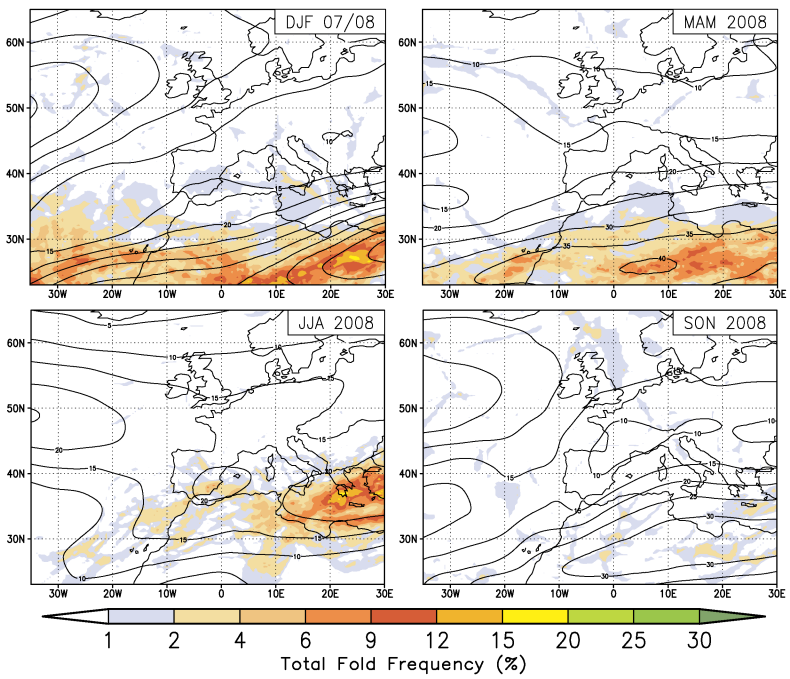

Figure 6.1: *Spatial fold frequency distribution (in %) from one year (December 2007 to November 2008) of WRF analysis data (JRA interpolated to the WRF model grid). Horizontal mean winds at 200 hPa are superimposed in black contours (5 m/s interval). All four seasons are represented: DJF (top left), MAM (top right), JJA (bottom left) and SON (bottom right), within the region of the WRF simulations domain.*

The discrepancies observed between figures 6.1 and 6.3 are expected basically from resolution considerations. Although the WRF analysis grid is the same as the 30 km model run grid, the meteorological fields are simply interpolated from the coarser 1.125° resolution JRA data. Because of a geometric definition has been used to detect TF, this spatially smoother data clearly prevent the geometric algorithm to identify a significant fraction of TF events. Both pattern distributions remarkably agree for all four seasons. However, TF frequencies found in figure 6.3 are substantially higher than in figure 6.1, to the extent that practically no cases are

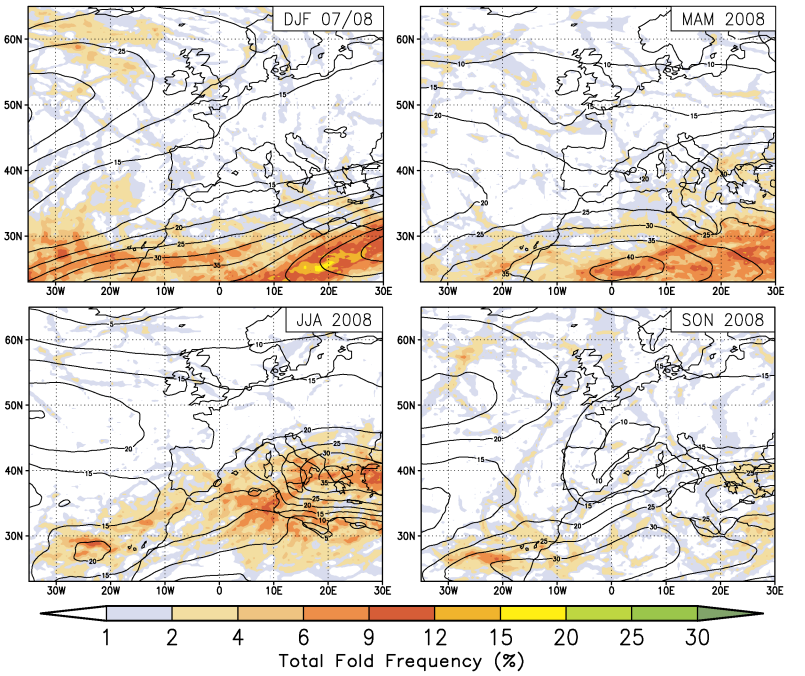

Figure 6.2: *Same as in figure 6.1 but for TF frequencies obtained from one year of WRF simulations.*

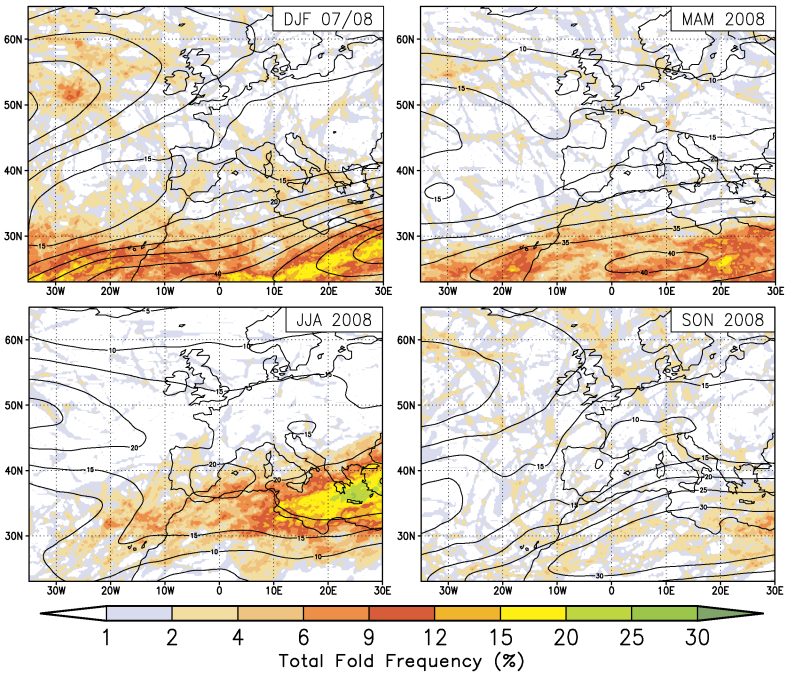

Figure 6.3: *Same as in figure 6.1 but from GFS analyses.*

observed in the extratropics in figure 6.1. As reported in chapters before, among these extratropical cases are partly found the most intense TF cases, but also the ones that present the smallest horizontal dimensions. If only along the intrusion horizontal direction (typically the smallest one), the folded region is narrower than the horizontal grid resolution, the folded information would most likely be missing and the TF neglected.

The resolution refinement is, therefore, a relevant aspect which allow to detect better the narrower structures. That is clearly visible in figure 6.3, where higher frequencies are found with the 0.3° resolution GFS data. Besides, these results suggest that the TF frequencies found by Sprenger et al. (2003), who used a similar geometric algorithm based on a global one-year examination of 1° horizontal resolution ECMWF analyses, may be underestimated, and particularly these among the deepest extratropical intrusions. Besides, the discrepancies observed between the Sprenger et al. (2003) results and the GFS 1-year analysis from chapter 4, a part from the annual variability, may include a significant fraction of resolution influence.

Observing now the results obtained with the WRF simulations in figure 6.2, on the one hand, the distribution patterns of TF frequencies show high agreement with the patterns obtained from the other two datasets, and on the other hand, the TF frequencies experience a significant increment compared to these in figure 6.1. That suggests that in a first approach, the mesoscale WRF model is able to develop and forecast TF events successfully. The only exception to this behaviour can be observed in summer over the eastern Mediterranean Sea, south of Greece, where TF frequencies are unexpectedly lower than the corresponding JRA or GFS TF frequencies found. Moreover, strong simulated wind gradients at 200 hPa are observed over that region in summer along with an odd strong divergence over Greece. WRF forcing is having some problems resulting from an unrealistic SST in summer over that particular region, which are responsible for the fold frequency summer pattern discrepancies observed. This particular concern is further address in the next section.

Besides, although several extratropical folding events may be now well detected with the model resolution refinement, TF frequencies in figure 6.2 are still far away from the values found with the GFS data in figure 6.3. Therefore, the model is still underestimating the number of TF cases or simply the entire real scope of individual TF events. In fact, the latter supposition has already been observed in chapters before, during a TF event taking place over the North Atlantic Ocean on February 3rd, 2008. It can be seen from these previous figures 4.7 and 5.4 as the area covered by the fold with the GFS and the WRF output data respectively differ considerably. Althought the TF is well located and simulated by the WRF model, it covers an insufficient area compared to the folded region shown by the GFS data.

Cross-sections also show a less prominent vertical structure developed by the model. This is also further analyzed in the next section, where different daily individual cases are examined.

6.2 TF individual case analyses

Tropopause Maps (see section 3.2), as well as different TF magnitudes, for the one-year period December 2007 to November 2008 have been studied and compared between the three different available data sets with the aim of further evaluate the ability of the WRF model to simulate these folding shape structures. In particular, the entire winter and summer seasons have been analyzed with daily images at 12 UTC. Besides, several TF cases have been examined through vertical cross-sections.

In general, the pressure field Tropopause Maps show good agreement between the three sets of data. However, as expected, the JRA field is smoother with less fine structure and flatter maximum values. From a synoptic point of view, it agrees better with the GFS field than it does the WRF simulation data. In fact, it can be observed as the pressure maxima derived from WRF outputs suffer a bit of drift and sometimes the main features do not coincide to such a high degree with the GFS. However, they show a finer structure and the maximum absolut values are closer to the GFS observations. This behaviour is generalized to nearly the entire daily images examined throughout the different seasons. On the other hand, the model is able to develop the majority of the folding intrusions while the JRA data misses a high number of them, particularly among the extratropical ones. Some illustrative examples within the winter and summer events are shown in this section.

6.2.1 Winter cases

Next figures 6.4 and 6.5 show pressure field Tropopause Maps and TF depths (in hPa) respectively, for a sequence of four consecutive winter days starting on December 17$^{\text{th}}$, 2007 at 12 UTC. Each column states for a different data set: WRF analyses (i.e. JRA) in the 1$^{\text{st}}$ column, WRF simulations after 24 hours run in 2$^{\text{nd}}$ column and GFS analyses in 3$^{\text{rd}}$ column.

The synoptic situation in figure 6.4 shows the generation of a cut-off low in the middle Atlantic Ocean between days 17$^{\text{th}}$ and 18$^{\text{th}}$. Simultaneously, a high pressure anomaly present over southern Europe reinforces to the west through the Bay of Biscay like a beginning cut-off on the 18$^{\text{th}}$. This latter anomaly, eventually evolves to the Mediterranean region later on the 19th and 20th as a narrow and elongated anomaly, strengthening on its equatorward side. Evidencing what it has

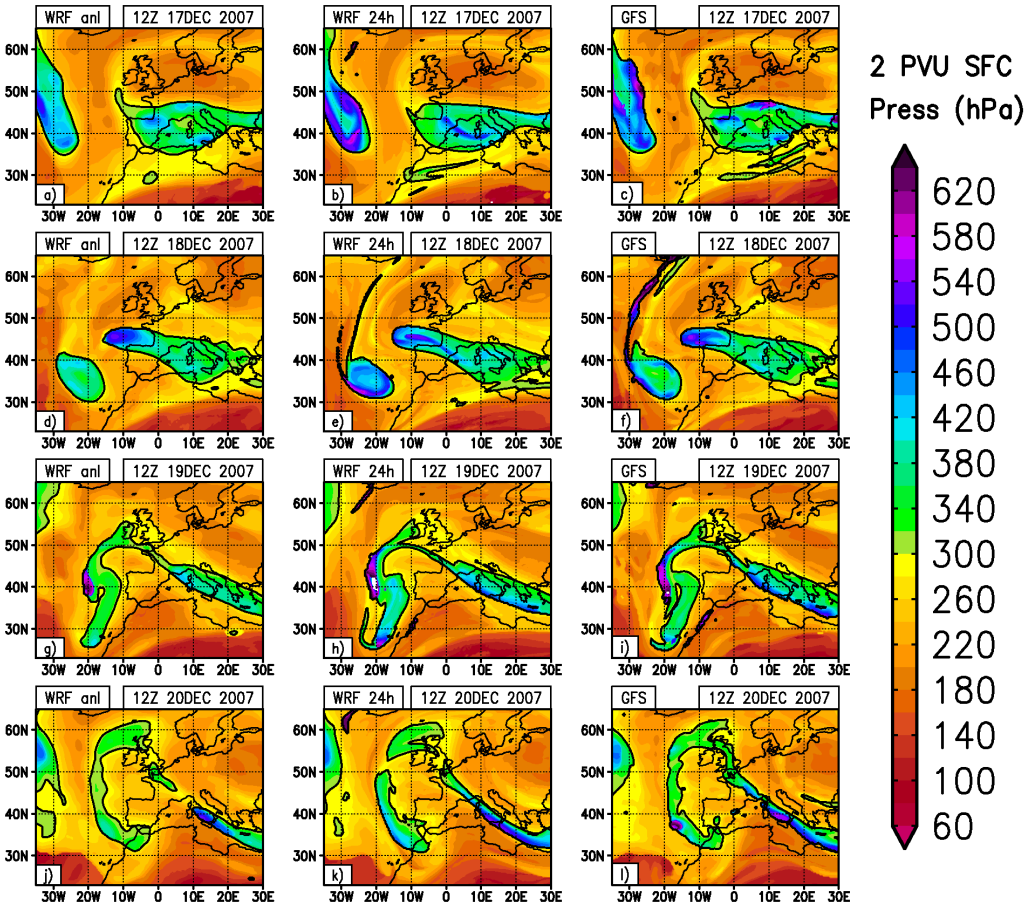

Figure 6.4: *Pressure field tropopause maps for December: a)-c) 17th, d)-f) 18th, g)-i) 19th and j)-l) 20th, 2007 at 12 UTC. Data in the first column is from WRF analyses (i.e. JRA), in the second column from WRF simulations and in the third column from GFS analyses.*

been described at the beginning of the section, the JRA images (1r column) display significantly weaker anomaly maxima while the WRF model generates stronger perturbances, closer to GFS observations. Moreover, examining in figure 6.5 the regions that show a folded structure and the depth values achives by these intrusions, these differences are even more clear. Compared to the GFS, the JRA data detects almost no folded tropopauses while the WRF model is able to develop the majority of them with depth values similar to those achieved by the GFS. However, it can be observed as the areas covered by the different instrusions displayed on the second column are in general smaller than these observed on the third column. This further supports the idea that the gap between the WRF model and the GFS TF frequencies observed, can be largely due to an insufficient extension development of

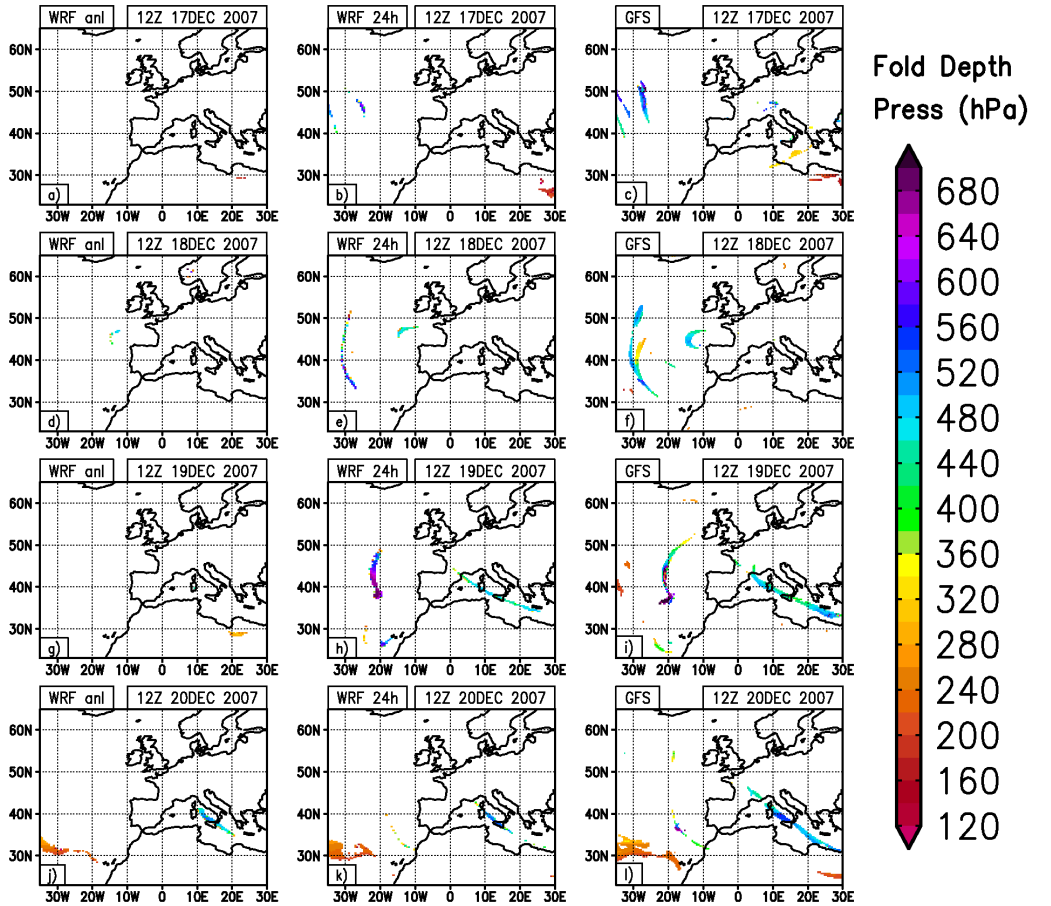

Figure 6.5: *Tropopause fold depths (in hPa) showing where the 2 PVU surface is folded in the tropopause maps from figure 6.4.*

simulated intrusions, more than to an understimation of TF cases. However, some understimation is also occurring as few cases are not detected by the model.

Vertical cross-sections throughout different transvers fold directions, such as these shown in figures 6.6 and 6.7, allow the examination and comparison between the three sets of data of the vertical structure and expansion of the above-mentioned instrusions. In both cases shown here, the JRA data is not able to detect any tropopause folding formation, to the extend that figure 6.6 (b) only depicts a rather smooth sloping dynamical tropopause. In contrast, the other two datasets (images (d) and (f) in figure 6.6) show a complex 2 PVU folding-shape structure.

Besides, the maximum winds found around the 300 hPa (white contours) reach values up to 70 m/s by the WRF model and the GFS analysis, while the JRA values

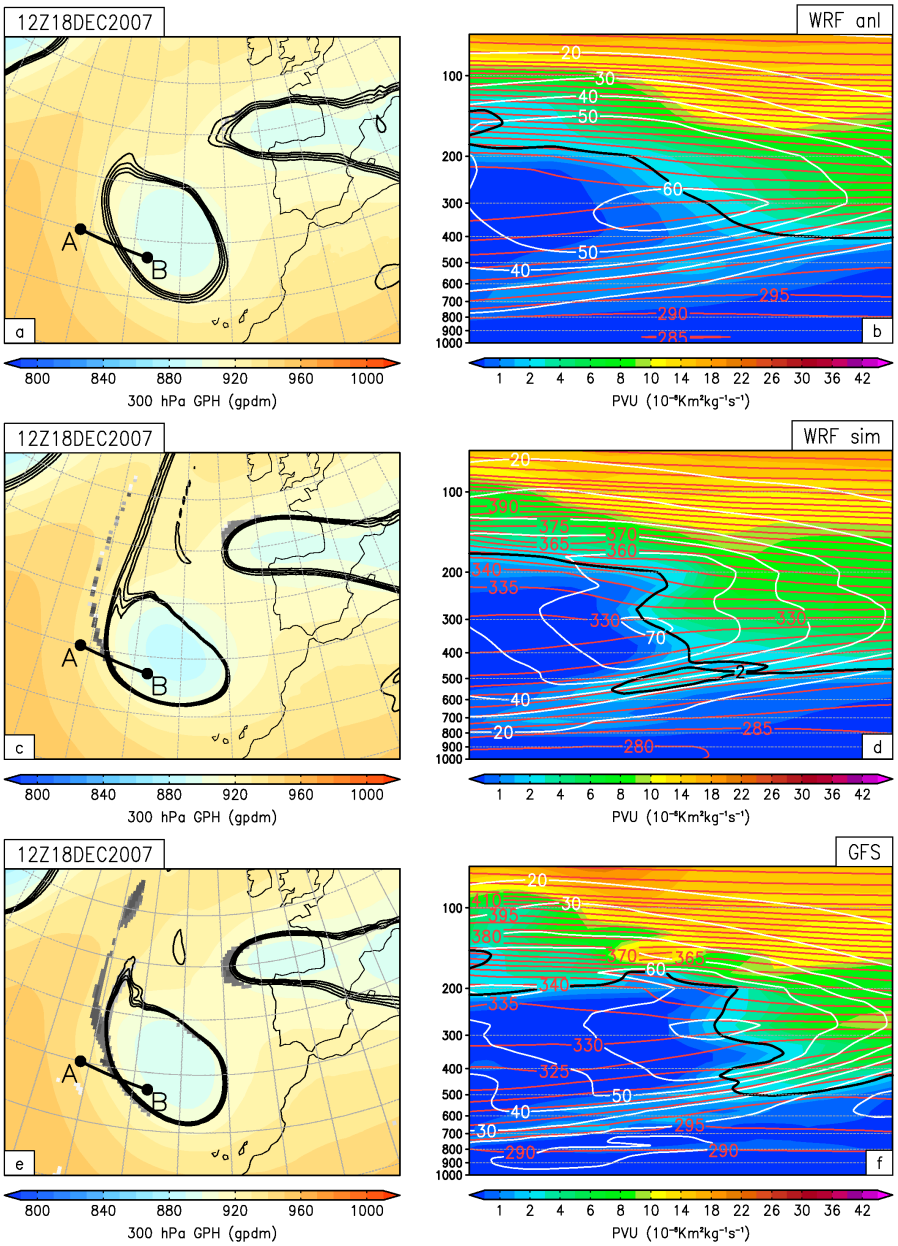

Figure 6.6: *Tropopause fold case on December 18th, 2007 at 12Z. Data from: a)-b) WRF analysis (i.e. JRA), c)-d) WRF 24 hours output and e)-f) GFS analisis. Left: 300 hPa geopotential height and folded regions (grey shaded). Superimposed in black contours the 1.5, 2, 2.5 and 3 PVU intersections with the 300 hPa surface. Right: vertical cross-section of PV through the segment A-B show in left. Superimposed, potential temperature lines in 5 K intervals (red contours) and horizontal wind magnitude in 10 m/s intervals (white contours). The black line outlines the 2 PVU surface.*

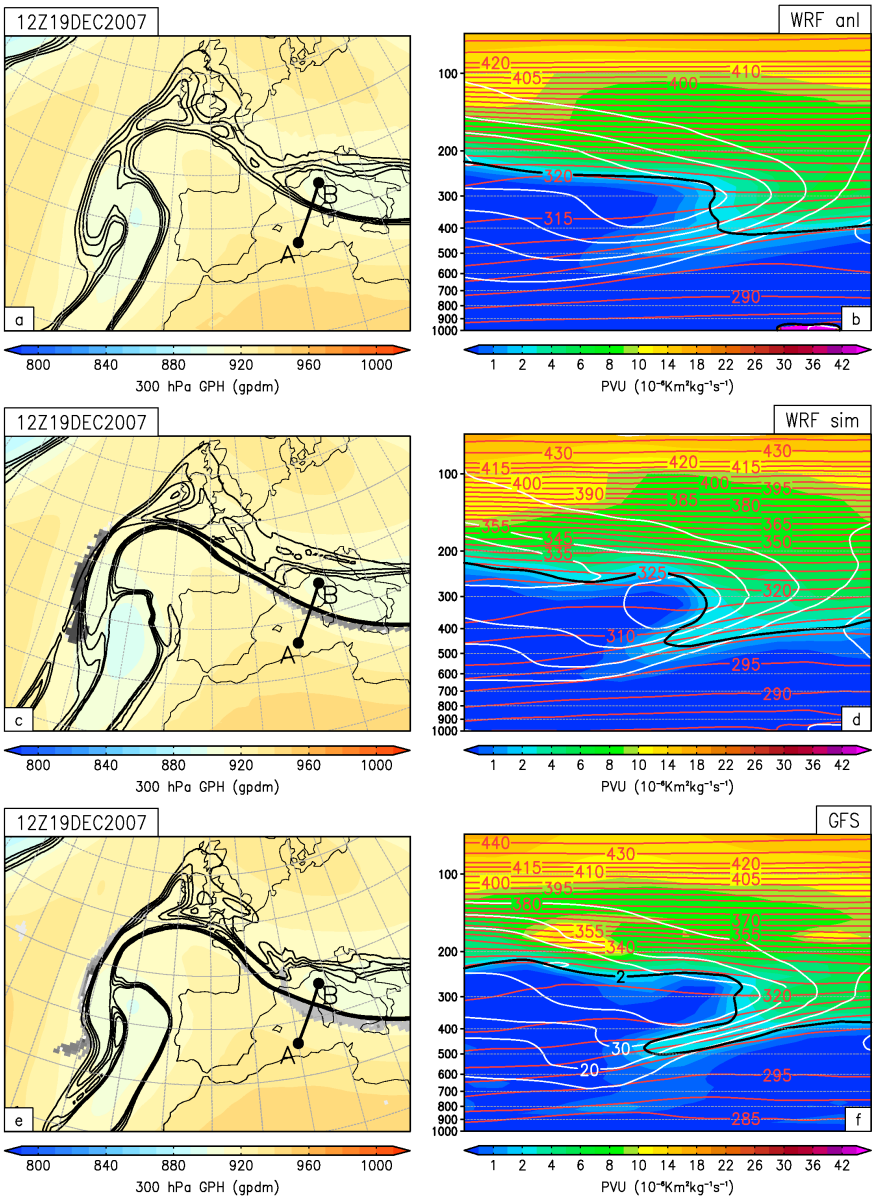

Figure 6.7: *Same as is figure 6.6 for a TF case on December 19th, 2007 at 12Z.*

are notably lower. The different vertical profiles examined across this TF generated on the west side of the cut-off low exhibit non-typical TF shapes[1]. The intrusion is most likely deformed by the strong cyclonic rotation of the cut-off. Moreover, the kind of tube-like structure which seems to be extruding from the stratospheric

[1] A typical tropopause fold shape could be the one shown in figure 6.7 by the WRF model and the GFS data (d and f plots)

tongue is visible along different certain cross-directions (by both WRF model and GFS data) as in this example is displayed by the WRF simulation (6.6 d). On the other hand, the folded area seen by the WRF model data is again significantly lower than that of the GFS folded region.

Turning now to the Mediterranean TF of the 19th December (figure 6.7), once more the WRF output intrusion is less pronounced in either the vertical and the horizontal extent than the one seen by the GFS analysis. Examining more carefully the vertical structure, it can be observed as slightly smaller wind and potential temperature gradients are present along the simulated TF tongue. Besides, the WRF analysis (JRA data) depicts an abrupt dynamical tropopause which fails to overlap. The wind and the potential temperature gradient are here noticeable less steep.

A plausible explanation for these more moderate dimensions of simulated TF, therefore, could simply be the inhability of the model, based on a lack of information from the mother JRA data at the initialization time, to fully develop a completely grown intrusion in only 24-hours run. It has actually been examined in chapter 3, subsection 3.4.1, the growth of a TF intrusion performed by different WRF simulations initialized at different times (see figure 3.7 and explanations thereby). The results show that longer forecasting times allow the WRF forcing to strengthen the folding tropopause structure, to the point of even making them grow more than the TF dimensions shown by the GFS data. However, it has also been point out as after excessive time forecast the WRF model suffers from too much drift, and particularly these strong tropopause structures which slightly misshape and displace from its supposed proper location. For that reason, the simulations were initialized every day and run for only 36-hours, accepting the possibility of an incomplete TF growth and therefore, a fraction loss on the climatological TF frequencies. In contrast, additional accuracy is obtained in the TF location and thus in the final TF frequency patterns.

In some few cases, the WRF 24-hours runs, can even miss completely the presence of a TF event. An example on February 9th can be observed in figure 6.8 where none of the two first plots in the left column (a and c for WRF analysis and WRF output respectively) show any sign of a folded tropopause as it does the third plot from GFS data (e).

Along the cross-sections A-B (right plots), the GFS shows a well-develop intrusion (f). On the contrary, the JRA data (b) detects only a mere undulation of the dynamical tropopause. Moreover, although the upper-level jet is also present in (b), the vertical wind shear above and below the cyclonic region of the jet and the upper-troposphere frontal zone (the sloping and the vertical shear of the isentropes) are significantly weaker than those observed in (f). With regard to the WRF model

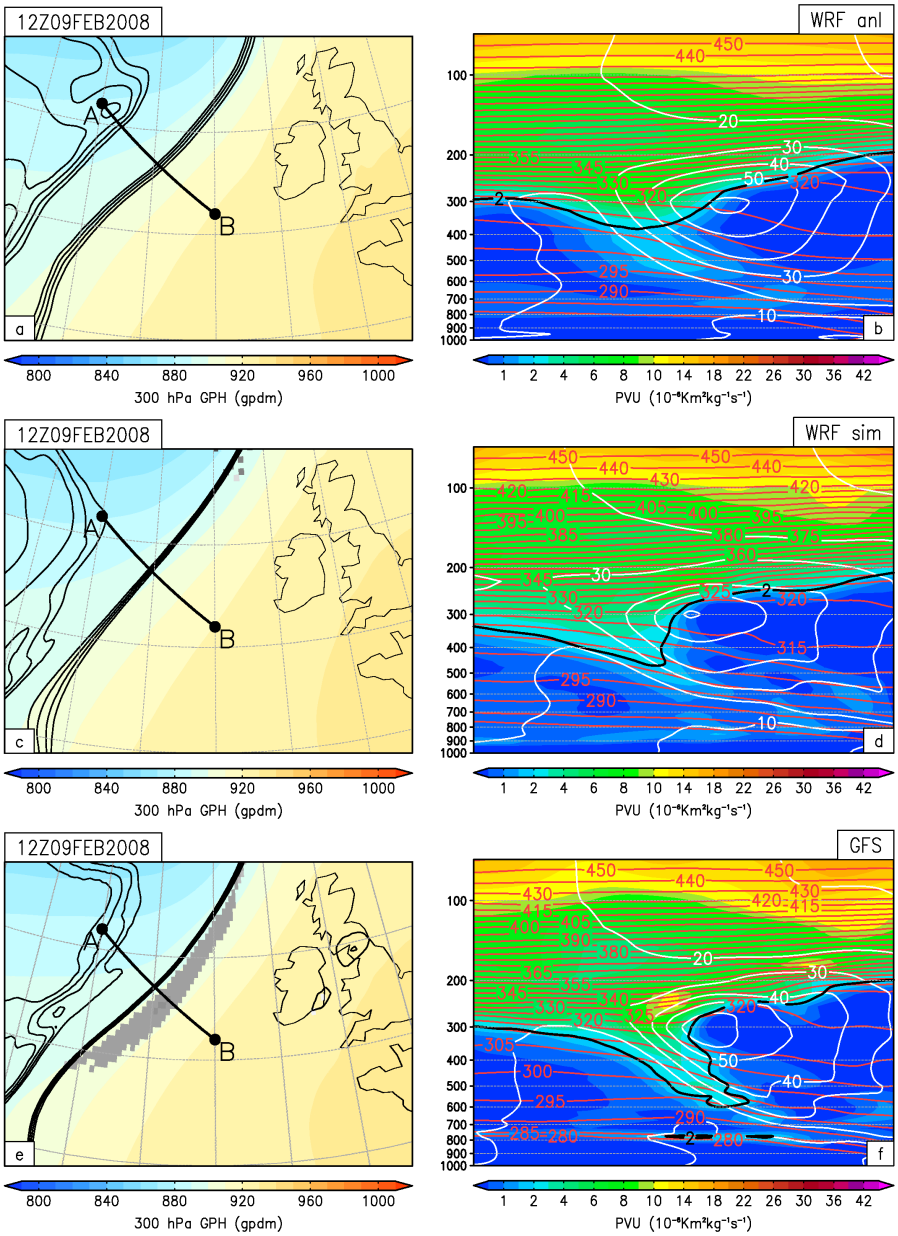

Figure 6.8: *Same as is figure 6.6 for a TF case on February 9th, 2008 at 12Z.*

(d), it can be observed as the wind shear and the tilted isentropes vertical gradient below the jet maxima slightly increase to respect the situation depicted by the JRA. However, the increment is fairly small and, although the 2 PVU line shows an abrupt jump like a kind of initial-state TF generation, the folding-shape structure is not attained.

It is diffucult to tell exactly the reasons why occasionally the model fails to originate the TF structure whereas it success in most cases. In this example, the lack of initial information and the insufficient simulation time seem to be reasonably the first causes. Pressure tropopause maps at 24-hours earlier (February 8th at 12 UTC) display this particular tropopause anomaly more to the west, short after entering the model domain (not shown). What is noticeable is that the maximum pressure achieved by the dynamical tropopause according to the JRA data is not more than 450 hPa and any sign of a TF is detected, while the GFS and the WRF simulation tropopauses reach values around the 600 hPa and the TF depth maps (not shown) reveal in both cases a fairly elongated folded-shape region, although reduced in the WRF output image. Therefore, the initialization data used in the model suffers from a significant lack of PV anomaly and tropopause structure, and although the model then slightly strengthens the upper-level frontogenesis (as observed in figure 6.8 d), it remains insufficiently develop.

The last winter case presented is an illustrative subtropical TF case, expectedly occurring in association with the subtropical jet on February 16th, 2008. Figure 6.9 highlights at first glance a quite extended TF which covers a substancial portion of square kilometers (grey shade on left plots). Along the latitudinal transvers-travelling jet direction (i.e. segment A-B), it can be broadly estimate a TF distance of about 800 km, and this width is relatively narrow compared to its zonal length. On the other hand, the intrusion is happening at significant higher altitudes than the examples before. In this case (see right plots), the upper tropopause is found at about the 100 hPa height and the intrusion (the lower 2 PVU line) deeps no further down the 300 hPa.

These observations are in accordance with the mean vertical and horizontal subtropical TF properties obtained in chapters 4 and 5 (see explanations in sections 4.2 and 5.2). The daily analysis performed here confirms that the majority of the subtropical TF structures are of this type. However, some of these TF sink at times a bit deeper, beneath the 450-500 hPa, and show more typical smaller extratropical dimensions. That basically happens when precisely an extratropical disturbance travels far equatorward to lower latitudes and interacts with the subtropical jet dynamics, or when the subtropical jet itself intensely waves and breaks off into smaller streams.

Comparing the TF event perceived by the three different sets of data, no major discrepancies are observed in this example. Observing also other cases of this type, it can be recognized as the GFS data presents often tropopause folding areas that cover slightly larger extensions and even, among the tiniest TF, some events are missed by the JRA data or the WRF simulations. However, both the JRA and the WRF model detect fairly well the majority of the subtropical winter cases and their

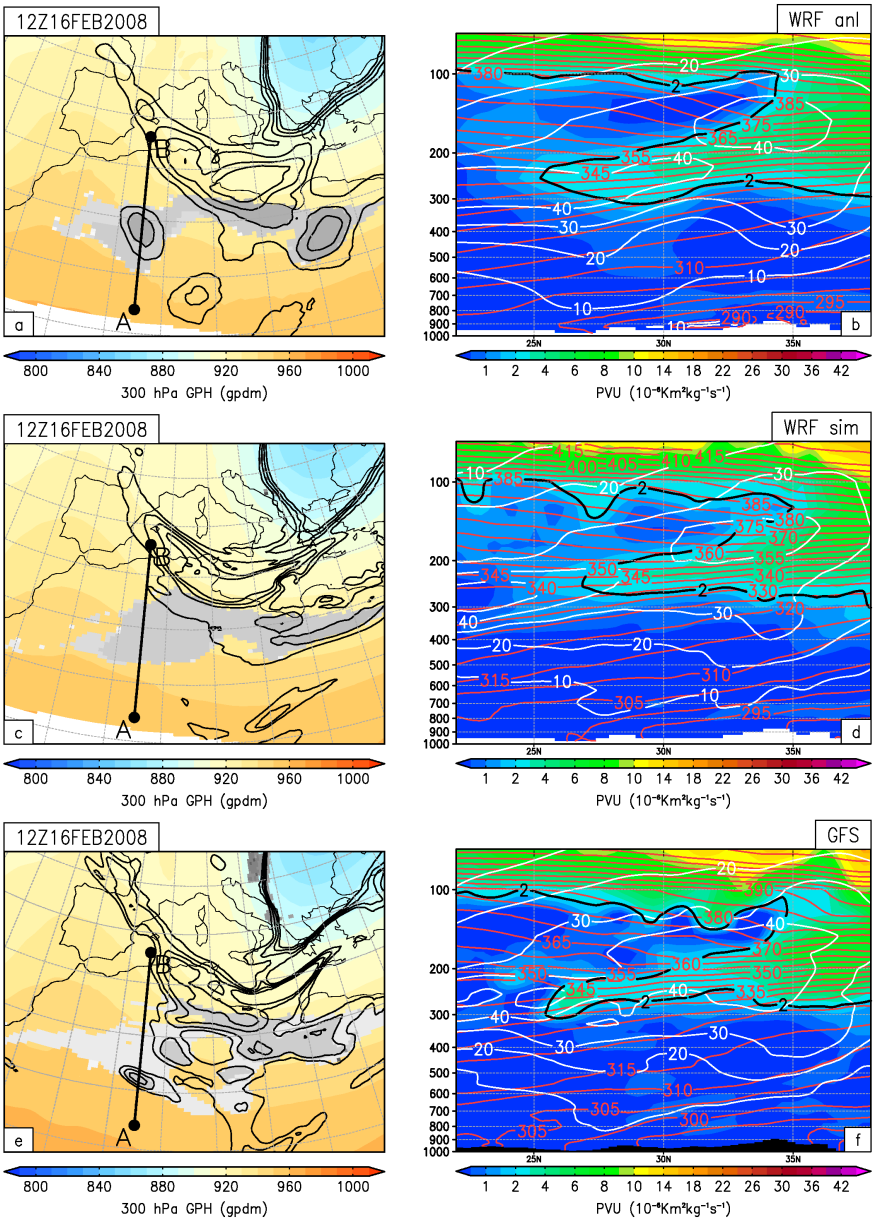

Figure 6.9: *Same as is figure 6.6 for a TF case on February 16th, 2008 at 12Z.*

average wide spread, although remaining somes a bit shorter. More similar cases are analyzed for the summer situation in the next section.

6.2.2 Summer cases. Eastern Mediterranean area

A sequence of four consecutive days from June 30th to July 3rd, 2008, of pressure Tropopause Maps and maximum pressure depths attained by the tropopause folded regions are displayed respectively in figures 6.10 and 6.11. They show, on the one hand, a couple of extratropical TF events, one on June 30th around the Faroe Islands and the other one on July 1st at around 48°N over the Atlantic Ocean. On the other hand, various subtropical TF events can be observed between 25°N and 40°N during these four days and, moreover, in almost every day throughout the entire summer season examined.

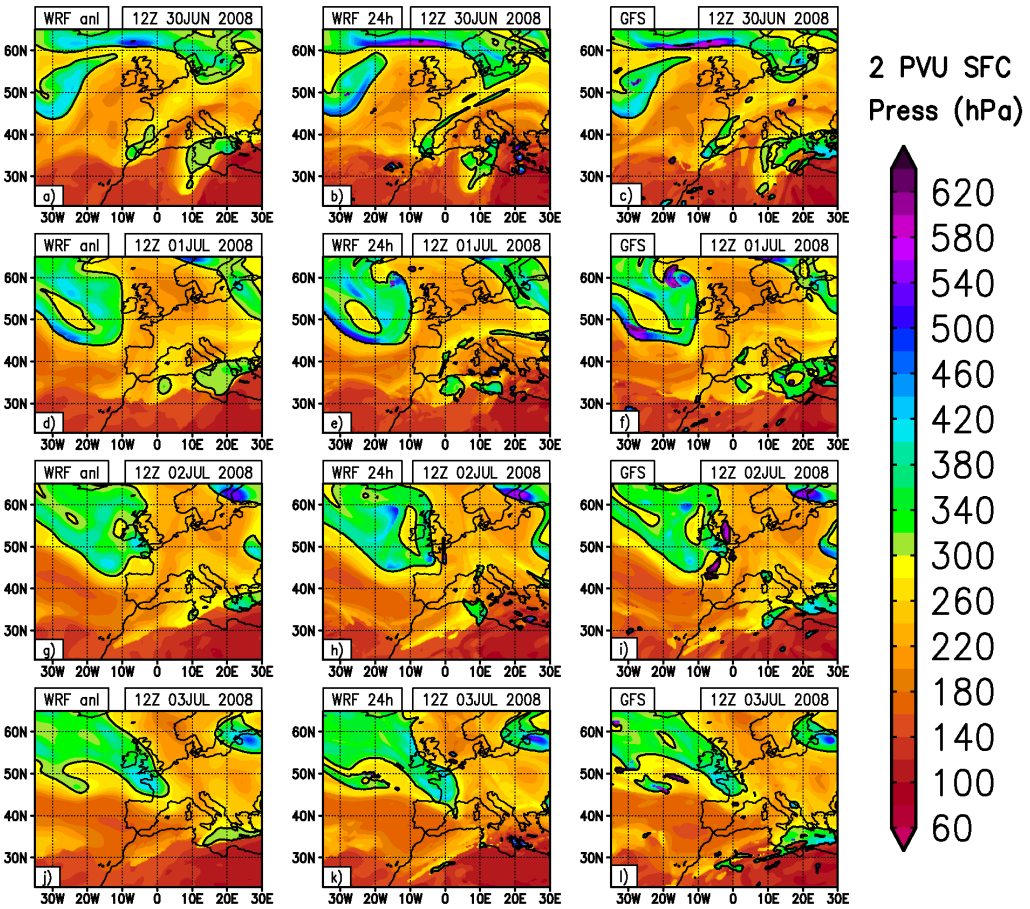

Figure 6.10: *Pressure field tropopause maps for: a)-c) June 30th, d)-f) July 1st, g)-i) July 2nd and j)-l) July 3rd, 2008 at 12 UTC. Data in the first column is from WRF analyses (i.e. JRA), in the second column from WRF simulations and in the third column from GFS analyses.*

The rare summer extratropical events show a similar performance between the

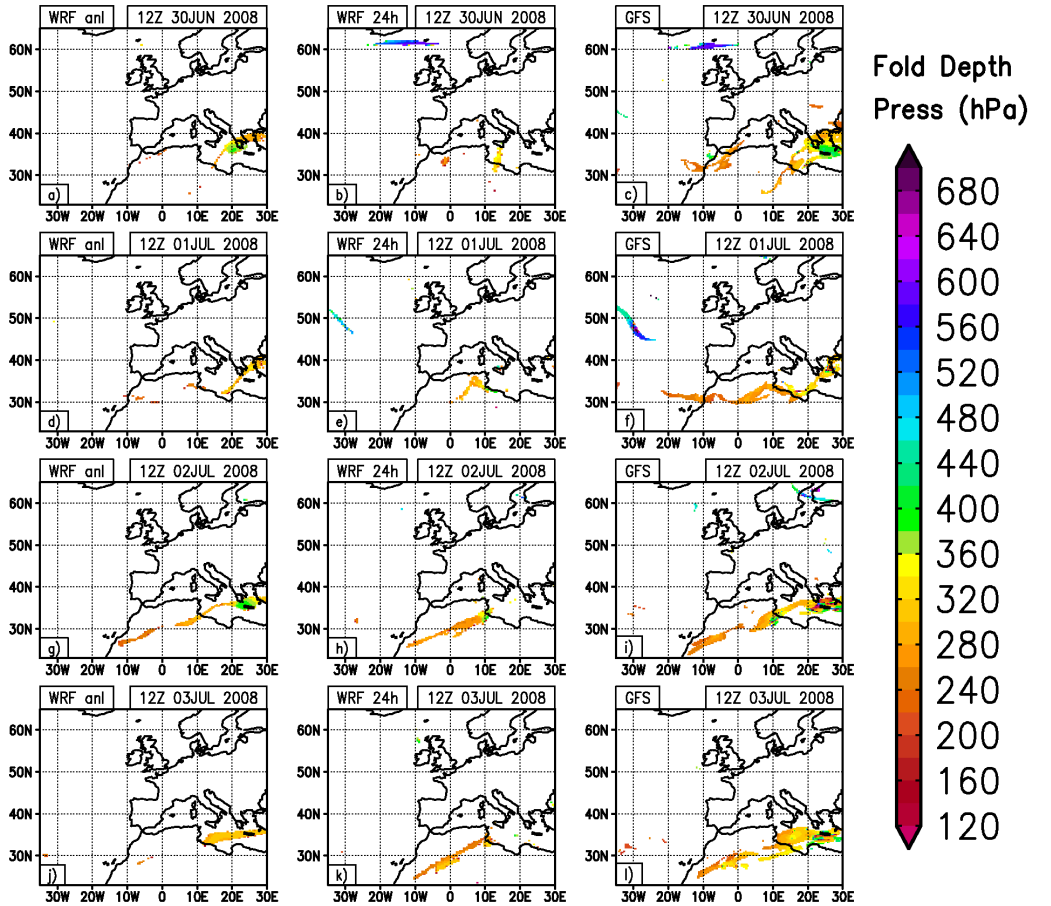

Figure 6.11: *Tropopause fold depths (in hPa) showing where the 2 PVU surface is folded in the tropopause maps from figure 6.10.*

three different sets of data than for the winter season: the JRA data shows tropopause pressure anomalies significantly smoother and misses the majority of these TF cases, while the WRF model success fairly well in its performance although sometimes it falls a bit short in the total extension covered by the fold, compared to the GFS folded-area dimensions. This can be observed, for example, in figure 6.10 where the extratropical pressure anomalies of the dynamical tropopause are notably lower in images (a) and (d) compared to those in images (b)-(c) and (e)-(f). In addition, figure 6.11 highlights as none of the two extratropical TF events that are present on June 30th and July 1st in images (b)-(c) and (e)-(f) (TF depths reaching blue colors) is perceived by the JRA data (plots a and d). Besides, the simulated folded area in (e) is significantly reduced compared to that in (f), while the folding regions are pretty much alike between images (b) and (c).

In figure 6.12 can be compared the vertical structure (right plots) displayed by the three different sets of data through the segment A-B (left plots) from the TF occurring on June 30th over the Faroe Islands. They visibly highlight the high agreement on the degree of maturity of the TF between the model and the GFS observations.

Turning now to the daily analisis of the summer subtropics, it highlights a quasi-permanent folded structure on the easternmost part of the domain. The TF cases observed have again similar characteristics to those from the winter subtropics though, as expected from previous results in chapters 4 and 5, they are found slightly poleward together with the displacement of the associated summer subtropical jet. Therefore, they cover in general big extensions, occur at higher altitudes and deep less into the troposphere. These features can be observed in figure 6.11 equatorward of 40°N.

In parallel, the similitudes and discrepancies between the JRA, the WRF model and the GFS on TF performance is again, in general, comparable to the winter subtropical TF cases. However, an exception can be observed along the entire summer. The WRF simulated data shows an odd TF performance over the western Mediterranean Sea that can be clearly noted in figure 6.11. For example, examining images on the second column, it can be observed as the folded tropopause systematically disappears when it enters the Mediterranean Sea, even though the JRA data detects folding regions (first column), as it does analogously the GFS data (third column).

In fact, on that region in summer, it has already been found regularly odd results along the entire TF analyses performed in chapter 5 and particularly, in the specific regional TF frequencies obtained. The 1-year climatology comparison of theses TF frequencies between the different datasets performed at the beggining of the ongoing chapter already anticipated an erroneous TF performance of the WRF model during summer in this region.

The next two figures 6.13 and 6.14 examine, for the three available data, the vertical profile of two different latitudinal sections through, respectively, the 25°E meridian on July 2nd and the 20°E meridian on July 3rd. Both cases show, aside from the modeled TF absence, an inconsistent troposphere structure derived from the WRF model data, compared to the other two data analyses. The WRF simulations display unexpectedly stronger upper-level divergencies with their maxima clearly displaced further poleward at about 38°N. This is exactly where figure 6.2 shows strong seasonal horizontal winds at 200 hPa in summer.

Besides, the dynamical tropopause shows strange wavy anomalies between latitudes 32°N and 35°N, precisely over the Mediterranean Sea neighboring the african coast. Moreover, intead of a tropopause fold as displayed by the other two images

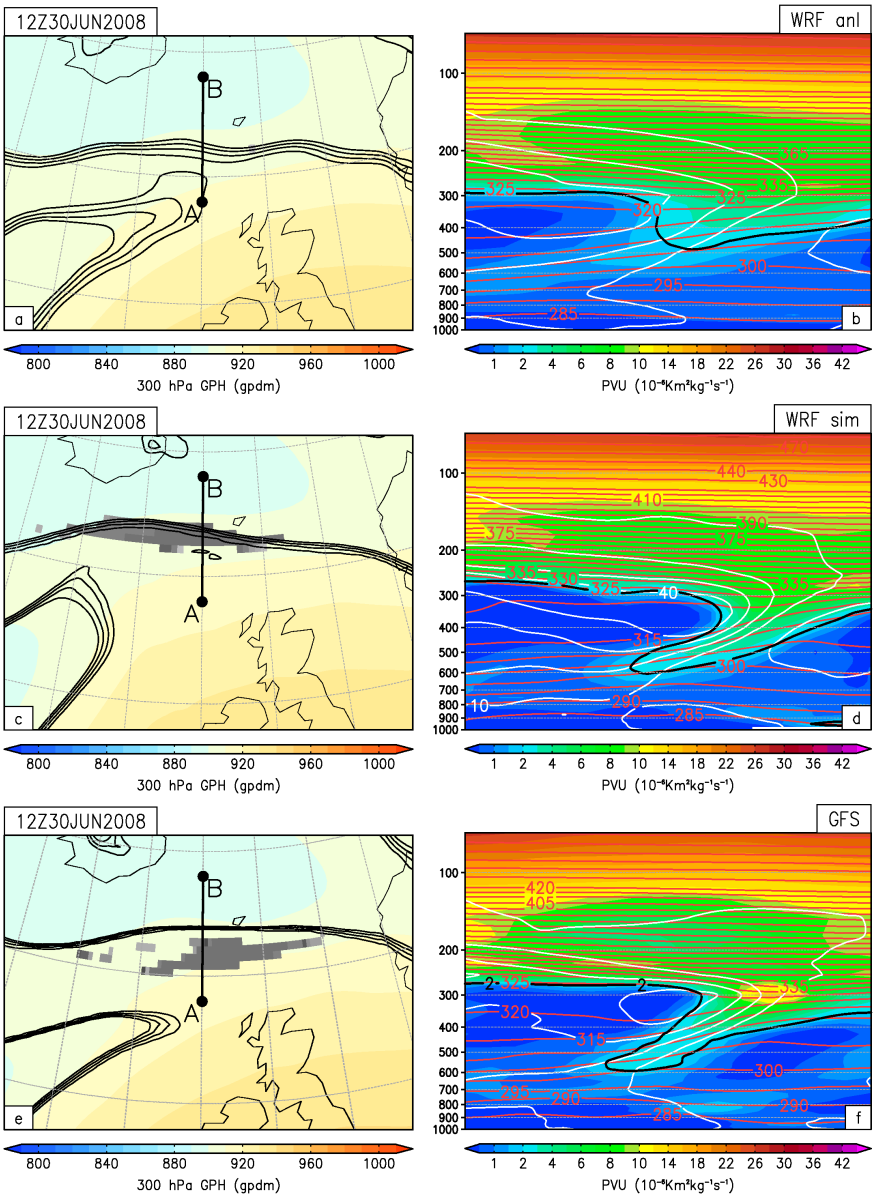

Figure 6.12: *Tropopause fold case on June 30th, 2008 at 12Z. Data from: a)-b) WRF analysis (i.e. JRA), c)-d) WRF 24 hours output and e)-f) GFS analisis. Left: 300 hPa geopotential height and folded regions (grey shaded). Superimposed in black contours the 1.5, 2, 2.5 and 3 PVU intersections with the 300 hPa surface. Right: vertical cross-section of PV through the segment A-B show in left. Superimposed, potential temperature lines in 5 K intervals (red contours) and horizontal wind magnitude in 10 m/s intervals (white contours). The black line outlines the 2 PVU surface.*

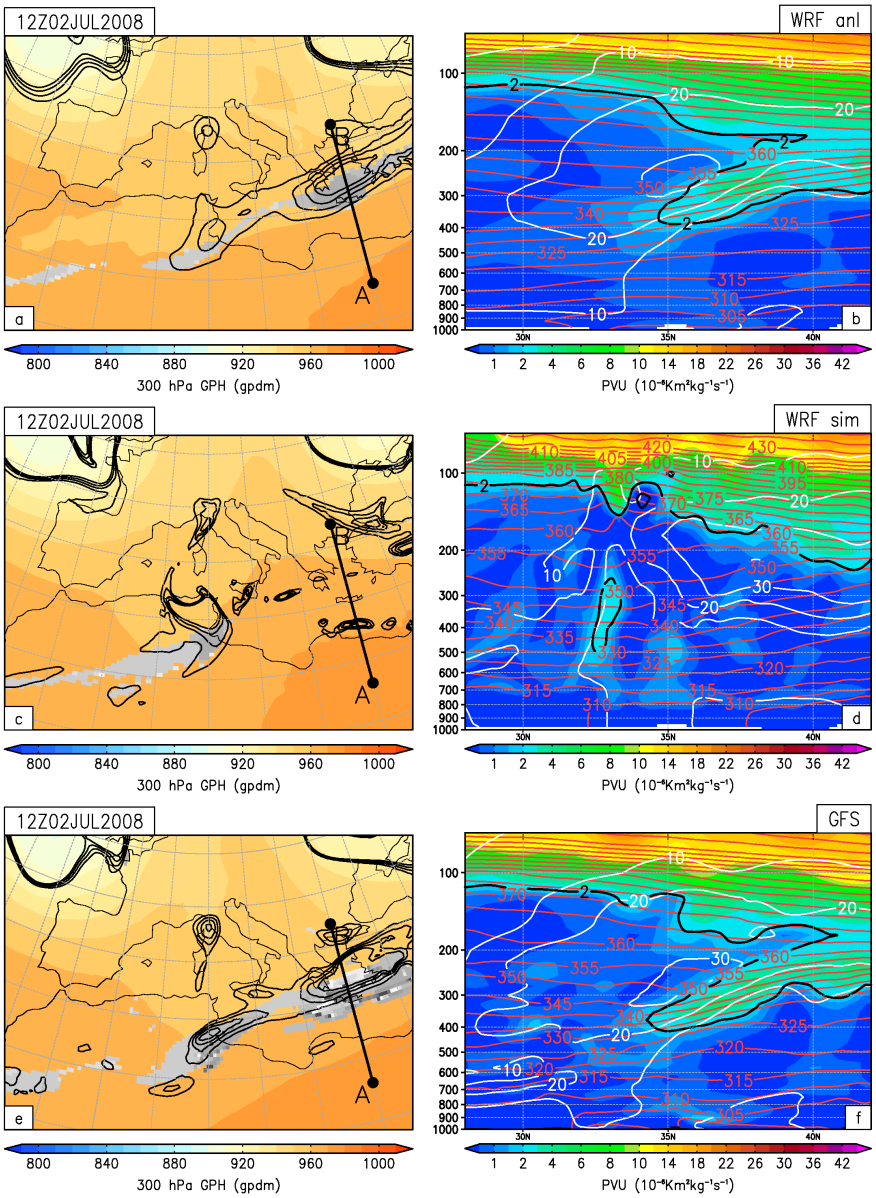

Figure 6.13: *Same as is figure 6.12 for a TF case on July 2nd, 2008 at 12Z.*

(b) and (f), a tropospheric bubble of high PV is present in the middle troposphere (images d). This tropospheric high PV anomaly, probably generated by adiabatic processes like laten heat release, together with the other discrepancies observed suggest that the model is most likely intruding, by excessive vertical motion, excessive moisture up into the middle and upper troposphere. In fact, the seasonal mean specific humidity at 200 hPa derived from the WRF simulations reveals a strong rel-

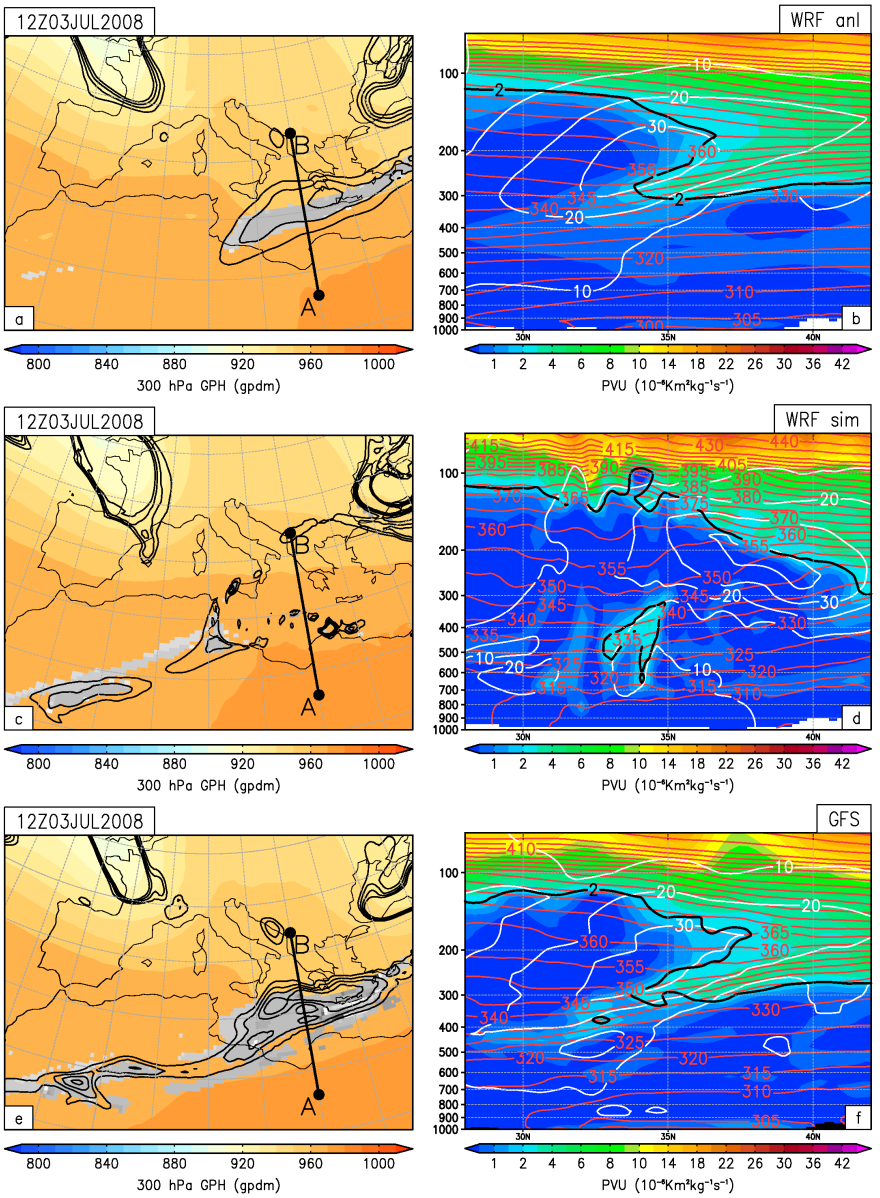

Figure 6.14: *Same as is figure 6.12 for a TF case on July 3rd, 2008 at 12Z.*

ative maximum over the entire west Mediterranean Sea, while both JRA and GFS display a relative minimum instead (not shown).

To further investigate these issues and with the aim of determining why there is so much divergence and moisture in the WRF performances, figure 6.15 shows monthly mean vertical profiles of specific humidity and winds through the 22°E

meridian between latitudes 25°N and 45°N (segment A-B in plot e) for July 2008. Plots (a) and (b) contour in black the monthly mean zonal winds in 10 m/s intervals derived from WRF analyses (JRA) and WRF simulations respectively. Analogously, plots (c) and (d) outline the monthly mean meridional winds in 5 m/s intervals, while plot (f) highlights the WRF simulated monthly mean vertical motion in 0.05 m/s intervals. The WRF analysis monthly mean vertical motion is not displayed since, as one would expect, no significant monthly mean values can be distinguished.

On the one hand, figure 6.15 evidences an important anomaly of specific humidity into the entire troposphere over the region in question for the WRF simulations (i.e. image b compare to a), most probably due to an excess of evaporation and too much convection. On the other hand, image (f) confirms this strong convection generated by the model, with a mean maximum value up to 0.2 m/s precisely located at the latitude where the maximum specific humidity anomaly is found. This vertical motion is also responsible for the strong upper-level zonal and meridional winds divergence observed in images (b) and (c).

These results explain the WRF model inconsistencies on the TF performance and the TF climatology frequencies found over that specific region of the western Mediterranean in summer. However, why is WRF producing these irregularities? The answer came after some correspondence discussion with J. Dudhia[2] through which it has been assessed this strong convection would most probably be attributable to an unrealistic Sea Surface Temperature (SST).

As the simulations performed in this study run for only 36-hours and were initilized every day, the SST data was not updated during the model runs and it was fixed by the default model settings. So as to verify and investigate the SST values used by the model, an arbitrary summer day (July 16th, 2008 at 12 UTC) has been compared with the daily average NOAA Optimum Interpolation (OI) Sea Surface Temperature (SST) V2 data (Reynolds et al. 2002) in figure 6.16. The above image visualizes the SST variable from the WRF input file provided by the WRF Preprocessing System after the entire input variables have been properly horizontally interpolated so as to serve as initialization data for the real simulation. Below, it has been plot for the same specific day the OI SST analysis, which uses in situ and satellite SST data to derive daily average SST.

Figure 6.16 highlights large SST deviations between both data over the western Mediterranean Sea for even more than 10°C. The WRF model SST input data is clearly unrealistic with values of more than 40°C, particularly over the Gulf of Sidra and all along the southwestern Mediterranean area, precisely where the strongest erroneous convection is generated by the model.

[2]Project Scientist III at the Mesoscale Prediction Group in the Mesoscale and Microscale Meteorology Laboratory, National Center for Atmospheric Research (NCAR), Boulder, Colorado.

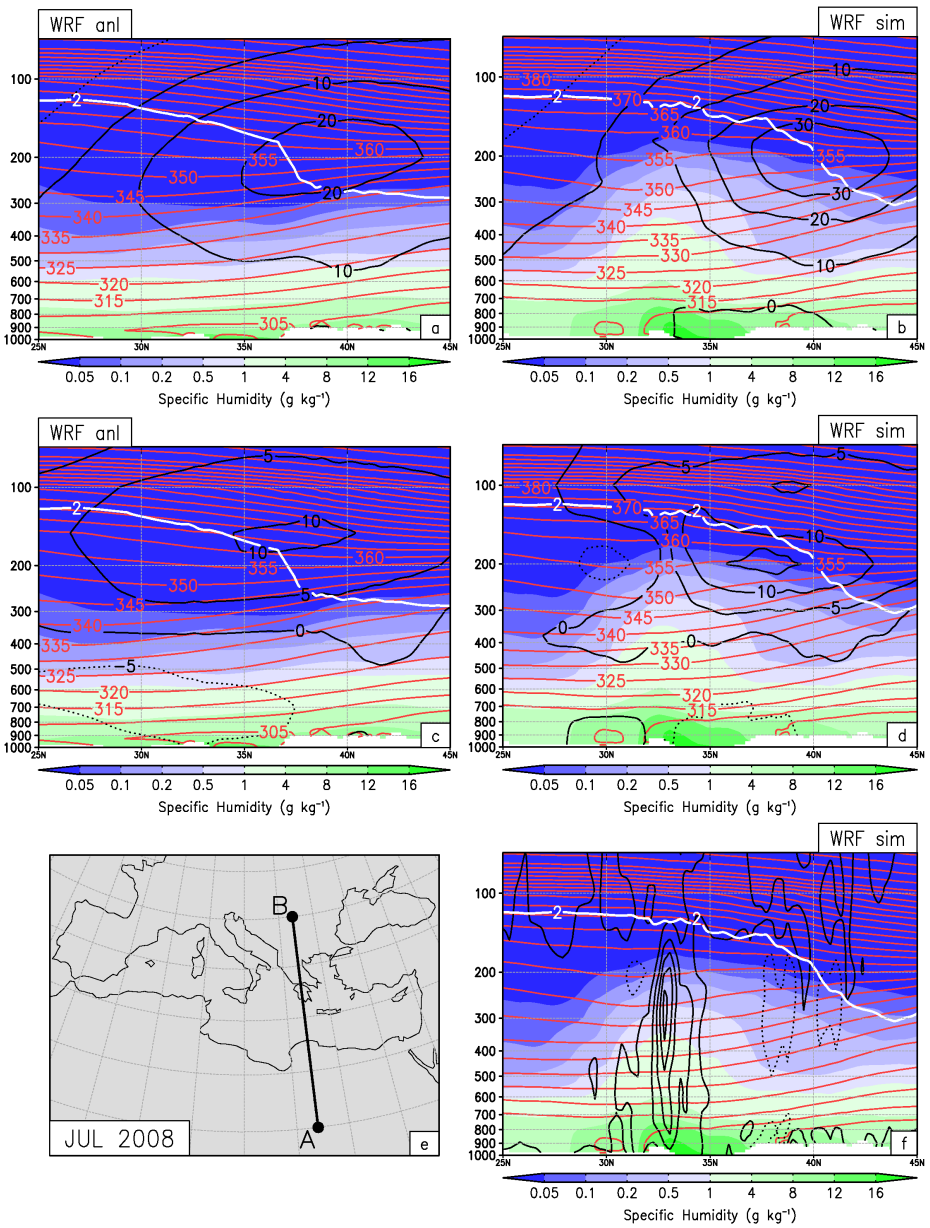

Figure 6.15: *July 2008 monthly mean vertical profiles of specific humidity and winds through the segment A-B in (e) for WRF analyses (left) and WRF 24-hours simulations (right). Shaded colors show specific humidity values in g kg^{-1}. Noticed the scale change between the blue and the green colors. Black contours depict in a)-b) the mean zonal winds in 10 m/s intervals, in c)-d) the mean meridional winds in 5 m/s intervals and in f) the mean vertical motion in 0.05 m/s intervals. Dotted contours for negative values. Red contours: potential temperature lines in 5 K intervals. The white line outlines the 2 PVU surface.*

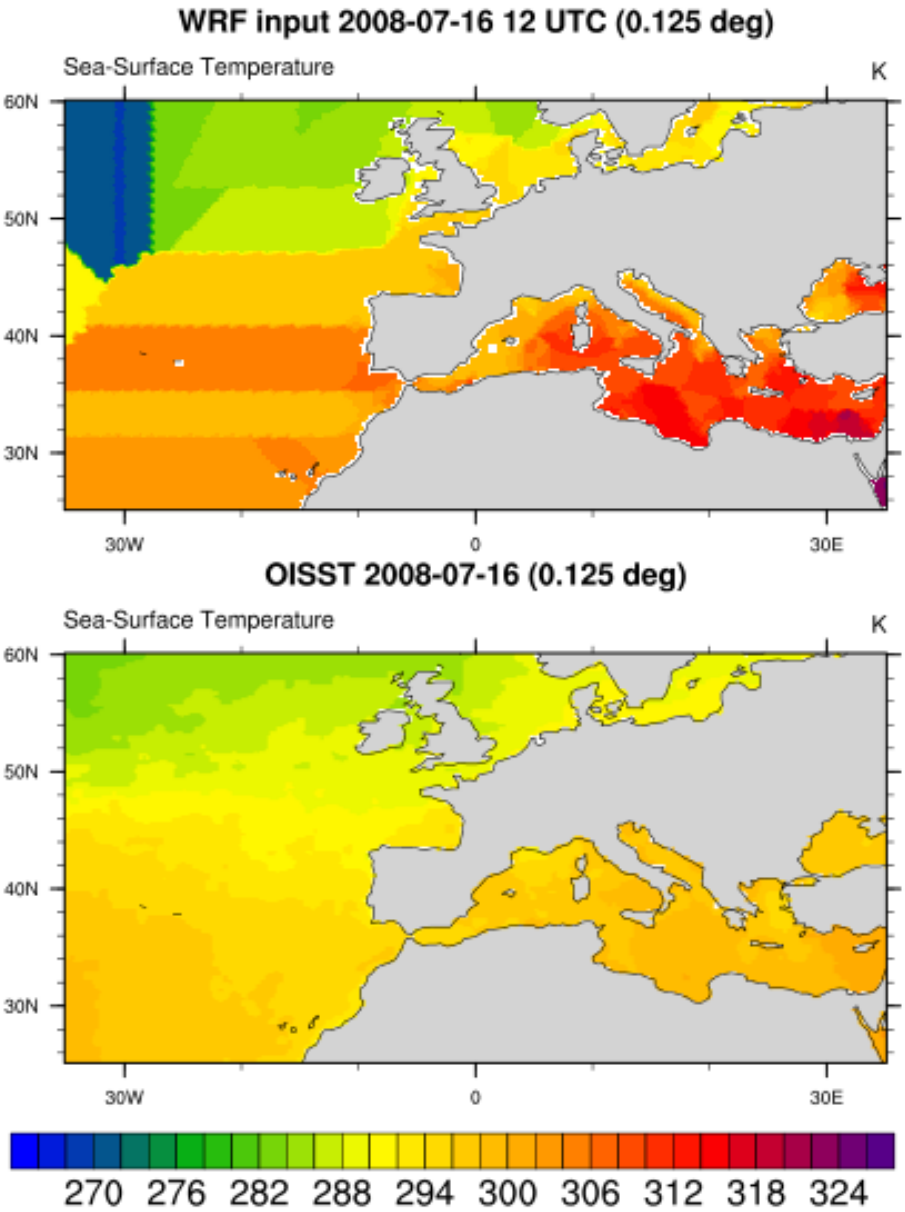

Figure 6.16: *Sea Surface Temperature on July 16th, 2008 at 12 UTC seen by the WRF model input data (above) and by OISST (below). Both data has been interpolated to a 0.125° grid for a better comparison. Courtesy of A. Montornès*[3]

This excessive convection, therefore, acts, on the one hand, as an inhibiter of TF intrusions. The pushing up winds vanish the upper-level frontal zones and displace further equatorward the lower-level dynamical tropopause as it can be observed from

[3]PhD student at the Department of Astronomy and Meteorology, University of Barcelona.

the tropospheric vertical structures shown by figures 6.13 and 6.14 (image d) or the monthly mean vertical profile in figure 6.15 (right images). Langford and Reid (1998) showed from water vapor images, ground-based lidar (ozone and aerosol) and radiosonde measurements as a stratrospheric intrusion abruptly disappeared by localized convective activity.

On the other hand, the high specific humidity brought up into the middle and upper troposphere generates adiabatical high PV bubbles which could at some point merge with any possible generated TF. If that was the case, then, these intrusions would most likely be ignored by the folding searching algorithm through the specific humidity threshold that discriminates the high PV air between being or not stratrospheric.

6.3 WRF TF quantitative validation

In order to get a more quantitative evaluation of the WRF model skills in TF performance, different statistical verification techniques have been used over a one year analysis (December 2007 - November 2008). On the one hand, following the commonly used point-to-point correspondance evaluation of regional gridded models againts observations, the WRF simulated 2 PVU dynamical tropopause pressure has been compared with the GFS T382 analysis and the WRF analysis (JRA) data. In parallel, also the WRF analyses have been compared with the GFS analyses for an overview of the differences between both tropopause representations, which a substantial portion may come from a resolution perspective. To facilitate point-to-point arithmetics, the WRF grid data (WRF simulations and WRF analyses) has been interpolated to the same GFS 0.3° regular grid.

Based on the statistic techniques used by Keyser and Anthes (1977), a quantitative test of model skill is the *Root Mean Square Error* (RMSE), defined as

$$RMSE = \left[\frac{1}{N} \sum_{i=1}^{N} (f_i - o_i)^2 \right]^{1/2} \tag{6.1}$$

where N is the total number of verification grid points and f_i and o_i are the considered forecast and observed values among the two compared dataset at the same grid point. Otherwise, a constant bias can be removed from the RSME by the *Standard Deviation of Error* (STDE)

$$STDE = \left[\frac{1}{N} \sum_{i=1}^{N} [(f_i - \bar{f}) - (o_i - \bar{o})]^2 \right]^{1/2} \tag{6.2}$$

where $\bar{f}$ and $\bar{o}$ are use to denote the considered variable means over the domain (arithmetic areal average), and their *Standard Deviations* (σ) are

$$\sigma_f = \left[\frac{1}{N} \sum_{i=1}^{N} (f_i - \bar{f})^2 \right]^{1/2} \tag{6.3}$$

$$\sigma_o = \left[\frac{1}{N} \sum_{i=1}^{N} (o_i - \bar{o})^2 \right]^{1/2} \tag{6.4}$$

A summary with the seasonal mean comparison results is given in table 6.1. The RMSEs obtain are quite similar to the STDEs (not shown), thus, no significant constant biases are present. The maximum bias is found in summer (JJA) between the WRF analyses and the GFS analyses where the RMSE is reduced by 3.2% from 21.6 hPa to the 20.9 hPa of the STDE value. The other RMSEs show a reduction of less than a 2%, and therefore the STDEs have not been considered in the summary table (6.1) and the following discussion.

Table 6.1: *Seasonal comparison analysis of the 2 PVU dynamical tropopause pressure (hPa) using Eq. 6.1-6.4 for three different pair of datasets.*

Season	RMSE			σ_{JRA}	σ_{WRF}	σ_{GFS}	$RMSE_{(i)}/\sigma_{GFS}$
	(i)	(ii)	(iii)				
DJF	34.3	27.4	27.2	66.6	71.1	70.8	0.48
MAM	35.7	30.3	23.9	69.6	74.7	72.7	0.49
JJA	32.8	28.4	21.6	67.9	72.4	67.7	0.48
SON	32.0	27.7	21.1	65.8	71.4	67.8	0.47

(i) WRF simulations vs. GFS analyses
(ii) WRF simulations vs. JRA (WRF analyses)
(iii) JRA (WRF analyses) vs. GFS analyses

As described by Keyser and Anthes (1977), skill is demonstrated when $\sigma_f \simeq \sigma_o$ and $RMSE < \sigma_o$. It can be observed as all the standard deviations are very close and the RMSEs values are about the half of the respective standard deviations, which gives, in a first approach, a good performing of the pressure field over the dynamical tropoause. In particular, the seasonal ratios of the RMSEs to the standard deviations for the comparison between the WRF simulation data and the GFS analyses are shown in the last column. A detailed examination evidences as the stardard deviation values for the JRA data are in general smaller, which is consistent with the lower variability of a smoother field from a coarser resolution grid. However, an exception can be observed in summer when JRA and GFS standard deviations are very close, precisely when the extratropical TF activity is in its minimum. Besides,

comparing the WRF simulations and the GFS analyses, the closer standard deviation is that from the winter (DJF), while the maximum discrepancy is observed in summer (JJA), possibily due to the effect of the unrealistic convection over the weastern Mediterranean Sea, as mentioned earlier in the chapter.

On the other hand, concepts of set theory can be used to determined the level of agreement of TF occurrences between the different datasets, similar to the techniques used to mesure the accuracy of simulated precipitation. The first quantity evaluated is the *Bias Score* (BS), which compares the fractional areas covered by a folded dynamical tropopause. Thus, if the area covered by tropopause folds for the first data set is FA_1, and the analogous area for the second data set is FA_2, then the BS is defined as

$$BS = \frac{FA_1}{FA_2} \tag{6.5}$$

Secondly, to evaluate the degree of coincidence between the two folded areas, the *Threat Score* (TS) parameter has been measured, define as

$$TS = \frac{(FA_1 \cap FA_2)}{FA_1 + FA_2 - (FA_1 \cap FA_2)} \tag{6.6}$$

where the symbol $\cap$ indicates the intersection area between the folded areas of the two sets. Therefore, the TS measures the fraction of the coinciding TF area with respect to the union of both total TF areas. An schematic illustration can be viewed in figure 6.17 for an idealized scenario.

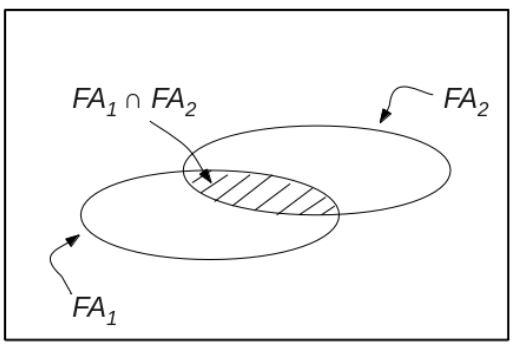

Figure 6.17: *Schematic illustration of an idealized TF case where the two folded areas seen by the two different datasets and their intersection area are represented.*

Table 6.2 shows the seasonal mean values from the above two additional evaluations between the same pair of datasets analyzed in table 6.1. In terms of the fractional area coverage (BS, perfect=1), the results reinforce in a quantitative way the observations from the two previous sections of the chapter. The biases obtained in column (iii) show as TFs from the JRA dataset are quite underestimated while

the WRF model simulations significally improve the TF area fractions with respect to the GFS observations. The highest fraction achived by the JRA is given in winter (DJF) with a half of the total TF area detected by the GFS, most probably on account of the subtropical TFs. Instead, the biases in column (i) are significantly smaller, although still an area fraction is lost with respect to the GFS TF areas. As observed previously in the individual fold case studies, the WRF model is in most cases not able to completely develop the TF structure in all its extension, which may be the major responsible for this fraction area underestimation. The highest TF fraction is given in autumn (SON), while the lowest is found in summer, probably related to the modeling TF inconsistencies over the eastern Mediterranean region, as mentioned earlier. In column (ii), noticed that the comparison has been performed with the JRA (WRF analyses) against the WRF simulations, particularly important for the BS results since it was expected that the area covered by TFs in the JRA dataset was smaller than that obtained with the WRF simulations. To put this another way, the smaller the BS, the smaller the JRA TF area fraction with respect to the WRF simulation TF area.

Table 6.2: *Seasonal comparison analysis of TF occurrence using Eq. 6.1-6.4 for the three different pair of datasets.*

Season	BS			TS		
	(i)	(ii)	(iii)	(i)	(ii)	(iii)
DJF	0.657	0.774	0.504	0.242	0.263	0.252
MAM	0.713	0.690	0.445	0.159	0.210	0.212
JJA	0.647	0.587	0.379	0.112	0.094	0.223
SON	0.854	0.301	0.256	0.090	0.062	0.120

(i) WRF simulations vs. GFS analyses
(ii) JRA (WRF analyses) vs. WRF simulations
(iii) JRA (WRF analyses) vs. GFS analyses

Examining now the mean Threat Score (TS) values obtained, it can be observed as the WRF model, with respect both the GFS and the JRA, localized better the TFs in winter and spring, particularly in winter, while in summer and autumn it shows relatively lower TS values. Noteworthy is the relatively good agreement between the JRA and GFS TF location. It can also be computed, the ratio of the intersection area of TFs to the total area covered by TF from one of the datasets (i.e. $FA_1 \cap FA_2$ to FA_1). These measures confirm (not shown) that more than half of the JRA folded-area is covered by GFS folded area, which confirms the high degree of coincidence over the spatial grid.

Chapter 7

Summary and Conclusions

Daily mesoscale WRF model simulations at 30 km resolution over a region centered in southwestern Europe and initialized with the Japanese ReAnalysis (JRA) dataset (with 1.125° resolution) have been performed covering a time period of 10 years (1999-2008). Special attention has been paid to the refinement of the vertical and horizontal resolution in order to achieve a detailed mesoscale characterization of the dynamical tropopause and, in particular, of the folding processes.

Based on a geometric definition of tropopause folds, a novel objective algorithm has been developed and applied over the 6-hour meteorological fields to unambiguously detect the folded 2 PVU tropopause, rich in stratospheric high PV, intruding into the troposphere. In addition, the algorithm is able to register the main geometric features of each individual folded grid structure such as the gap, the thickness, the depth of penetration or the horizontal dimensions, allowing different classifications and a complete characterization. A product that uses a combination of these geometric TF parameters has been created: Stratosphere-Troposphere Transport Folding Index, (STTFI). It provides a simple method to estimate the regions of the globe where the largest amounts of stratospheric air are most likely to be transferred irreversibly into the troposphere due to deep TF intrusions.

In parallel, the same algorithm has been applied to one year of global GFS analysis data (at 0.3° resolution), which contain valuable observational and satellite data assimilations, and a similar vertical and horizontal resolution to that of the WRF mesoscale simulations. This has served, firstly, to validate the algorithm after comparing the resulting global GFS fold frequencies with other existing global TF climatologies and, subsequently, to validate the regional WRF simulation climatology.

Finally, a detailed investigation on the WRF model ability to represent TFs

over southwestern Europe has been evaluated for an entire year (December 2007 - November 2008). This analysis has focussed on the ability of the model to simulate TF processes, with an eye at establishing the role of refinements in resolution at improving their representation. Comparisons with both the initial JRA data and the GFS analyses have provided, on the one hand, a qualitative validation of the TF climatology along with a comparative study of individual TF cases, and on the other hand, a more quantitative evaluation accomplished through different statistical techniques.

The geographical distribution and annual variability of stratospheric intrusions detected with the GFS analyses around the globe are in line with existing climatologies (e.g. Sprenger et al. 2003), which supports the competence of the fold searching algorithm. The higher data resolution afforded by the GFS data set relative to that of the existing TF climatologies offers a more detailed portrait and a slight increment of TF frequencies over certain areas. The analysis has served to corroborate the differences between the extratropics and the subtropics in TF characteristics and formation, and to identify the main synoptic upper-level scenarios that drive the intensification of these structures:

1. TF frequencies are highest in the subtropics associated with the subtropical jet, with stronger and more extended activity in the winter hemispheres, and with a preference to form on the west side of jet maxima and over typical RWB regions. The summer subtropics can also present locally high TF frequencies, mainly associated with upper-level monsoon circulations. In fact, it has been observed that the onset and decay phases of monsoon circulations in spring and autumn are also accompanied by important TF formation.

2. Extratropical TFs are significantly less frequent, although they are more intense and intrude deeper into the troposphere. That can make them very efficient on STT. They are mainly associated with the polar jet and midlatitude cyclone activity. Hence, they are more frequent and stronger in the winter hemispheres, particularly along the Southern Ocean latitudes and the North Pacific and North Atlantic storm-track regions. Extratropical fold activity in summer is almost nonexistent.

3. The STT Folding Index (SSTFI) reproduces the most important regional features portrayed in existing STT climatologies based on Lagrangian trajectory techniques (e.g. Wernli and Bourqui (2002), James et al. 2003, Sprenger and Wernli 2003, Škerlak et al. 2014). Despite its simplicity it provides an estimate for evaluating the main contributions of STT due to deep TFs. The highest values are observed in the winter extratropics, extending from the east coast of North America to the south of Iceland, all along the North Pacific Ocean

from Japan to Alaska and Canada, and in the Southern Ocean along the East Antarctica coast, where high activity can also be observed during austral autumn (MAM) and spring (SON), particularly around 140°E longitude in this latter season.

4. Subtropical TFs are in general shallower structures that occur at higher altitudes and sink little into the troposphere, which explains in broad terms why the STTFI shows little signs of transport over these latitudes despite the high TF frequencies observed. Besides, as it is known, the strong PV gradient in the vicinities of the subtropical tropopause break act as a dynamical barrier to meridional movements, thus the irreversible subtropical exchange should be less efficient. However, in summer, when the jet is relatively weaker and the PV gradient smaller, two-way insentropic and irreversible mixing is likely to occur during TF processes associated with monsoon circulations, particularly when midlatitude synoptic-scale disturbances interact with the main subtropical flow and TF extend for large areas in a more north-to-south direction.

The 10-years WRF TF evaluation provides a more robust climatology centered on the regional particularities of southwestern Europe, which show in general a good agreement with the one-year GFS observations:

5. The geographical distribution of TF frequencies for the WRF 10-year analysis is in good agreement with that observed for one year of GFS data, although WRF frequencies are in general much lower. That can be largely explained by interannual variability reasons.

6. The subtropical annual variability shows a bimodal distribution with one maximum in February-March and the other in June-July. This maximum in summer is not observed in hemispherically averaged global climatologies, but the specific WRF domain of study comprises a region influenced by the westernmost part of the Asian Monsoon Anticyclon, which is associated with enhanced TF formation, particularly over Turkey. The year minimum is attained in November, when subtropical TF activity falls below the extratropical activity value.

7. The extratropical annual cycle, in contrast, identifies only a unimodal distribution with a maximum in November and a minimum in July, with a preference for TF formation between latitudes 55°N and 65°N.

8. The extratropical Deep intrusions show a similiar annual behavior to that of the total extratropical TF formation with intense activity from October to March. In the subtropics, Deep intrusions are strongly reduced in number and limited from December to February, and mainly occurring in the regions with the strongest subtropical wind gradients. From April to October, subtropical Deep

TFs are almost nonexistent.

9. The TF characteristics of depth, gap and horizontal dimensions show clear seasonal and geographical differences that support distinct dynamical TF formation in different regions and seasons.

10. The highest depths of penetration can reach the 850 hPa, particularly in the winter extratropics in association with the strongest baroclinic atmosphere.

11. Although in general large TF depths occur with large TF gaps, relatively shallow depths in combination with big gaps can be observed in some subtropical regions. This is basically observed in association with anomalously high tropical tropopauses, suggesting a two-way intrusion conceptual model: stratospheric air on the cyclonic side of the jet core intruding below it and into the troposphere along with tropical upper-tropospheric air from the anticyclonic side of the jet intruding above it and into the stratosphere.

12. TFs in the subtropics present large zonal dimensions, particularly in winter, as they can fold extensively all along the jet-traveling direction for more than one or two thousand kilometers. In the transvers jet-traveling direction, which is usually the "fold intrusion direction", mean distances range roughly between 50 to 400 km, with the biggest mean values found precisely in the preferred regions of RWB or subtropical jet discontinuities. In the extratropics, both mean distances are about the same order and strongly varying between different regions, evidencing the larger complexity of the synoptic flow.

13. The biggest values of the STT Folding Index for a 10-years evaluation over the WRF study domain are found in winter from the northern North Atlantic to the North Sea and west European coast, the northern African continent particularly over central Algeria, and the eastern Mediterranean Sea. A similiar distribution can be found in spring and autumn though with significant lower values, except over an extended area of the northern North Atlantic region in autumn where strong TF transport is also likely to occur.

The qualitative and quantitative WRF modeled TF validation demonstrates that the WRF forcing, starting from the JRA coarse description of the initial state, is in general able to forecast the main mesoscale TF features. However, it has been observed that the poor definition of the initial conditions can be an important obstacle in TF performance, particularly under certain circumstances in some specific areas:

14. The coarse JRA dataset misses an important fraction of TF structures, particularly among the deeper extratropical TF cases which present in general smaller horizontal dimensions. In particular, the seasonal mean TF area ratios of JRA

to GFS range from a maximum of 50% in winter to a minimum of 25% in autumn. These discrepancies are basically due to resolution considerations and they demonstrate that the resolution refinement is of crucial importance, particularly when TFs are based on a geometric definition.

15. The WRF model resolution refinement significantly improves these area ratios to equal or more than a 65% in all four seasons. The model is able to develop the majority of TF events successfully and it is particularly improving the extratropical TF representation, precisely where a significant increment of TF frequencies can be observed. However, WRF simulations are still underestimating the mean TF area ratios relative to GFS. Most individual TF events are detected by WRF (only a few remain undefined), although the WRF TF representations tends to depict smaller folded areas, which results in a notable TF frequency underestimation with respect to the observed GFS frequencies.

16. Besides, although the WRF model shows reasonably good skills on TF forecasting, it has still room for improvement, for example using a better resolution of the initial data, a more realistic SST prescription or using a more realistic shortwave radiation parameterization that considers the ozone distribution in the atmosphere (e.g. the New Goddard scheme).

Bibliography

Añel, J. A., J. C. Antuña, L. de la Torre, J. M. Castanheira, and L. Gimeno, 2008: Climatological features of global multiple tropopause events. *Journal of Geophysical Research: Atmospheres (1984–2012)*, **113**.

Añel, J. A., L. de la Torre, and L. Gimeno, 2012: On the origin of the air between multiple tropopauses at midlatitudes. *The Scientific World Journal*, **2012**.

Antonescu, B., G. Vaughan, and D. M. Schultz, 2013: A five-year radar-based climatology of tropopause folds and deep convection over Wales, United Kingdom. *Monthly Weather Review*, **141**, 1693–1707.

Baray, J.-L., V. Daniel, G. Ancellet, and B. Legras, 2000: Planetary-scale tropopause folds in the southern subtropics. *Geophysical research letters*, **27**, 353–356.

Beekmann, M., G. Ancellet, S. Blonsky, D. De Muer, A. Ebel, H. Elbern, J. Hendricks, J. Kowol, C. Mancier, R. Sladkovic, et al., 1997: Regional and global tropopause fold occurrence and related ozone flux across the tropopause. *Journal of Atmospheric Chemistry*, **28**, 29–44.

Beekmann, M., G. Ancellet, and G. Mégie, 1994: Climatology of tropospheric ozone in southern Europe and its relation to potential vorticity. *Journal of Geophysical Research: Atmospheres (1984–2012)*, **99**, 12841–12853.

Bethan, S., G. Vaughan, and S. Reid, 1996: A comparison of ozone and thermal tropopause heights and the impact of tropopause definition on quantifying the ozone content of the troposphere. *Quarterly Journal of the Royal Meteorological Society*, **122**, 929–944.

Bian, J., L. L. Pan, L. Paulik, H. Vömel, H. Chen, and D. Lu, 2012: In situ water vapor and ozone measurements in Lhasa and Kunming during the Asian summer monsoon. *Geophysical Research Letters*, **39**.

Bithell, M., L. Gray, and B. Cox, 1999: A three-dimensional view of the evolution of midlatitude stratospheric intrusions. *Journal of the atmospheric sciences*, **56**, 673–688.

Blonsky, S. and P. Speth, 1998: An algorithm to detect tropopause folds from ozone soundings. *Meteorologische Zeitschrift*, **7**, 153–162.

Browning, K. and R. Reynolds, 1994: Diagnostic study of a narrow cold-frontal rainband and severe winds associated with a stratospheric intrusion. *Quarterly Journal of the Royal Meteorological Society*, **120**, 235–257.

Bush, A. B. and W. Peltier, 1994: Tropopause folds and synoptic-scale baroclinic wave life cycles. *Journal of the atmospheric sciences*, **51**, 1581–1604.

Campana, K., P. Caplan, K. Campana, and P. Caplan, 2005: Technical Procedure Bulletin for T382 Global Forecast System. *NWS EMC. [Available online at http://www. emc. ncep. noaa. gov/gc_wmb/Documentation/TPBoct05/T382. TPB. FINAL. htm.]*.

Castanheira, J. and L. Gimeno, 2011: Association of double tropopause events with baroclinic waves. *Journal of Geophysical Research: Atmospheres (1984–2012)*, **116**.

Chen, P., 1995: Isentropic cross-tropopause mass exchange in the extratropics. *Journal of Geophysical Research: Atmospheres (1984–2012)*, **100**, 16661–16673.

Chen, X., J. A. Anel, Z. Su, L. de la Torre, H. Kelder, J. van Peet, and Y. Ma, 2013: The deep atmospheric boundary layer and its significance to the stratosphere and troposphere exchange over the Tibetan Plateau. *PloS one*, **8**, e56909.

Chou, M.-D. and M. J. Suarez, 1999: A solar radiation parameterization for atmospheric studies. *NASA Tech. Memo*, **104606**, 40.

Chou, M.-D., M. J. Suarez, X.-Z. Liang, M. M.-H. Yan, and C. Cote, 2001: A thermal infrared radiation parameterization for atmospheric studies. *2001.*.

Croci-Maspoli, M., 2002: *Eine neue Methode zur Erkennung von Tropopausenfalten*. Diploma thesis, IACETH, Swiss Federal Institute of Technology Zurich, Switzerland.

Danielsen, E. F., 1968: Stratospheric-tropospheric exchange based on radioactivity, ozone and potential vorticity. *Journal of the Atmospheric Sciences*, **25**, 502–518.

— 1985: Ozone transport. *Ozone in the free Atmosphere*, 123–159.

Dethof, A., A. O'Neill, J. Slingo, and H. Smit, 1999: A mechanism for moistening the lower stratosphere involving the Asian summer monsoon. *Quarterly Journal of the Royal Meteorological Society*, **125**, 1079–1106.

Dudhia, J., 1989: Numerical study of convection observed during the winter monsoon experiment using a mesoscale two-dimensional model. *Journal of the Atmospheric Sciences*, **46**, 3077–3107.

Dunkerton, T. J., 1995: Evidence of meridional motion in the summer lower stratosphere adjacent to monsoon regions. *Journal of Geophysical Research: Atmospheres (1984–2012)*, **100**, 16675–16688.

Elbern, H., J. Hendricks, and A. Ebel, 1998: A climatology of tropopause folds by global analyses. *Theoretical and applied climatology*, **59**, 181–200.

Ertel, H., 1942: Ein neuer hydrodynamischer wirbelsatz. *Meteorol. Z.*, **59**, 277–281.

Gettelman, A., P. Hoor, L. Pan, W. Randel, M. Hegglin, and T. Birner, 2011: The extratropical upper troposphere and lower stratosphere. *Reviews of Geophysics*, **49**, RG3003.

Gettelman, A., D. E. Kinnison, T. J. Dunkerton, and G. P. Brasseur, 2004: Impact of monsoon circulations on the upper troposphere and lower stratosphere. *Journal of Geophysical Research: Atmospheres (1984–2012)*, **109**.

Gill, A., 1980: Some simple solutions for heat-induced tropical circulation. *Quarterly Journal of the Royal Meteorological Society*, **106**, 447–462.

Goering, M. A., W. A. Gallus, M. A. Olsen, and J. L. Stanford, 2001: Role of stratospheric air in a severe weather event: Analysis of potential vorticity and total ozone. *Journal of Geophysical Research: Atmospheres (1984–2012)*, **106**, 11813–11823.

Griffiths, M., A. J. Thorpe, and K. A. Browning, 2000: Convective destabilization by a tropopause fold diagnosed using potential-vorticity inversion. *Quarterly Journal of the Royal Meteorological Society*, **126**, 125–144.

Haqq-Misra, J., S. Lee, and D. M. Frierson, 2011: Tropopause structure and the role of eddies. *Journal of the Atmospheric Sciences*, **68**, 2930–2944.

Haynes, P., J. Scinocca, and M. Greenslade, 2001: Formation and maintenance of the extratropical tropopause by baroclinic eddies. *Geophysical research letters*, **28**, 4179–4182.

Held, I. M., 1982: On the height of the tropopause and the static stability of the troposphere. *Journal of the Atmospheric Sciences*, **39**, 412–417.

Highwood, E. and B. Hoskins, 1998: The tropical tropopause. *Quarterly Journal of the Royal Meteorological Society*, **124**, 1579–1604.

Hoerling, M. P., T. K. Schaack, and A. J. Lenzen, 1991: Global objective tropopause analysis. *Monthly Weather Review*, **119**, 1816–1831.

Hoinka, K., 1997: The tropopause: Discovery, definition and demarcation. *Meteorologische Zeitschrift*, **6**, 281–303.

Hoinka, K., H. Claude, and U. Köhler, 1996: On the correlation between tropopause pressure and ozone above central Europe. *Geophysical research letters*, **23**, 1753–1756.

Hoinka, K. P., 1998: Statistics of the global tropopause pressure. *Monthly Weather Review*, **126**, 3303–3325.

Holton, J. R., P. H. Haynes, M. E. McIntyre, A. R. Douglass, R. B. Rood, and L. Pfister, 1995: Stratosphere-troposphere exchange. *Reviews of Geophysics*, **33**, 403–439.

Hong, S.-Y., J. Dudhia, and S.-H. Chen, 2004: A revised approach to ice microphysical processes for the bulk parameterization of clouds and precipitation. *Monthly Weather Review*, **132**, 103–120.

Hoskins, B. and P. Berrisford, 1988: A potential vorticity perspective of the storm of 15-16 October 1987. *Weather*, **43**, 122–129.

Hoskins, B., M. McIntyre, and A. W. Robertson, 1985: On the use and significance of isentropic potential vorticity maps. *Quarterly Journal of the Royal Meteorological Society*, **111**, 877–946.

Hoskins, B. J. and M. J. Rodwell, 1995: A model of the Asian summer monsoon. Part i: The global scale. *Journal of the atmospheric sciences*, **52**, 1329–1340.

James, P., A. Stohl, C. Forster, S. Eckhardt, P. Seibert, and A. Frank, 2003: A 15-year climatology of stratosphere-troposphere exchange with a Lagrangian particle dispersion model 2. Mean climate and seasonal variability. *Journal of Geophysical Research: Atmospheres (1984–2012)*, **108**.

Juckes, M. and M. McIntyre, 1987: A high-resolution one-layer model of breaking planetary waves in the stratosphere. *Nature*, **328**, 590–596.

Kain, J. S., 2004: The Kain-Fritsch convective parameterization: an update. *Journal of Applied Meteorology*, **43**, 170–181.

Keyser, D. and R. A. Anthes, 1977: The applicability of a mixed-layer model of the planetary boundary layer to real-data forecasting. *Monthly Weather Review*, **105**, 1351–1371.

Keyser, D. and M. Shapiro, 1986: A review of the structure and dynamics of upper-level frontal zones. *Monthly Weather Review*, **114**, 452–499.

Koch, S. E., B. D. Jamison, C. Lu, T. L. Smith, E. I. Tollerud, C. Girz, N. Wang, T. P. Lane, M. A. Shapiro, D. D. Parrish, et al., 2005: Turbulence and gravity waves within an upper-level front. *Journal of the atmospheric sciences*, **62**, 3885–3908.

König, W., R. Sausen, and F. Sielmann, 1993: Objective identification of cyclones in GCM simulations. *Journal of Climate*, **6**, 2217–2231.

Konopka, P., J.-U. Grooß, G. Günther, F. Ploeger, R. Pommrich, R. Müller, and N. Livesey, 2010: Annual cycle of ozone at and above the tropical tropopause: observations versus simulations with the Chemical Lagrangian Model of the Stratosphere (CLaMS). *Atmospheric Chemistry and Physics*, **10**, 121–132.

Kunz, A., P. Konopka, R. Müller, and L. Pan, 2011: Dynamical tropopause based on isentropic potential vorticity gradients. *Journal of Geophysical Research: Atmospheres (1984-2012)*, **116**.

Lamarque, J.-F. and P. G. Hess, 1994: Cross-tropopause mass exchange and potential vorticity budget in a simulated tropopause folding. *Journal of the atmospheric sciences*, **51**, 2246–2269.

Langford, A. and S. Reid, 1998: Dissipation and mixing of a small-scale stratospheric intrusion in the upper troposphere. *Journal of Geophysical Research: Atmospheres (1984–2012)*, **103**, 31265–31276.

Manabe, S. and R. F. Strickler, 1964: Thermal equilibrium of the atmosphere with a convective adjustment. *Journal of the Atmospheric Sciences*, **21**, 361–385.

Mlawer, E. J., S. J. Taubman, P. D. Brown, M. J. Iacono, and S. A. Clough, 1997: Radiative transfer for inhomogeneous atmospheres: RRTM, a validated correlated-k model for the longwave. *Journal of geophysical research*, **102**, 16663–16.

Montornès, A., B. Codina, and J. Zack, 2014: Analysis of the ozone profile specifications in the WRF-ARW model and their impact on the simulation of direct solar radiation. *Atmospheric Chemistry and Physics Discussions*, **14**, 20231–20257.

Morgan, M. C. and J. W. Nielsen-Gammon, 1998: Using tropopause maps to diagnose midlatitude weather systems. *Monthly weather review*, **126**, 2555–2579.

Nielsen-Gammon, J. W., 2001: A visualization of the global dynamic tropopause. *Bulletin of the American Meteorological Society*, **82**, 1151–1167.

Noh, Y., W. Cheon, S. Hong, and S. Raasch, 2003: Improvement of the K-profile model for the planetary boundary layer based on large eddy simulation data. *Boundary-layer meteorology*, **107**, 401–427.

Ohkawara, N., 2006: Japanese 25-year reanalysis (JRA-25). *Proc. of SPIE Vol*, volume 6404, 640409–1.

Olsen, M. A., A. R. Douglass, P. A. Newman, J. C. Gille, B. Nardi, V. A. Yudin, D. E. Kinnison, and R. Khosravi, 2008: HIRDLS observations and simulation of a lower stratospheric intrusion of tropical air to high latitudes. *Geophysical Research Letters*, **35**.

Olsen, M. A., M. R. Schoeberl, and A. R. Douglass, 2004: Stratosphere-troposphere exchange of mass and ozone. *Journal of Geophysical Research: Atmospheres (1984–2012)*, **109**.

Onogi, K., J. Tsutsui, H. Koide, M. Sakamoto, S. Kobayashi, H. Hatsushika, T. Matsumoto, N. Yamazaki, H. KAMAHORI, K. Takahashi, et al., 2007: The JRA-25 reanalysis. *Journal of the Meteorological Society of Japan*, **85**, 369–432.

Pan, L., W. Randel, B. Gary, M. Mahoney, and E. J. Hintsa, 2004: Definitions and sharpness of the extratropical tropopause: A trace gas perspective. *Journal of Geophysical Research: Atmospheres (1984–2012)*, **109**.

Pan, L., W. Randel, J. Gille, W. Hall, B. Nardi, S. Massie, V. Yudin, R. Khosravi, P. Konopka, and D. Tarasick, 2009: Tropospheric intrusions associated with the secondary tropopause. *Journal of Geophysical Research: Atmospheres (1984-2012)*, **114**.

Park, M., W. J. Randel, A. Gettelman, S. T. Massie, and J. H. Jiang, 2007: Transport above the Asian summer monsoon anticyclone inferred from Aura Microwave Limb Sounder tracers. *Journal of Geophysical Research: Atmospheres (1984–2012)*, **112**.

Parracho, A., C. Marques, and J. Castanheira, 2014: Where do the air masses between double tropopauses come from? *Atmospheric Chemistry and Physics Discussions*, **14**, 1349–1374.

Peevey, T. R., J. C. Gille, C. E. Randall, and A. Kunz, 2012: Investigation of double tropopause spatial and temporal global variability utilizing High Resolution Dynamics Limb Sounder temperature observations. *Journal of Geophysical Research: Atmospheres (1984-2012)*, **117**.

Randel, W. J. and M. Park, 2006: Deep convective influence on the asian summer monsoon anticyclone and associated tracer variability observed with atmospheric

infrared sounder (airs). *Journal of Geophysical Research: Atmospheres (1984–2012)*, **111**.

Randel, W. J., M. Park, L. Emmons, D. Kinnison, P. Bernath, K. A. Walker, C. Boone, and H. Pumphrey, 2010: Asian monsoon transport of pollution to the stratosphere. *Science*, **328**, 611–613.

Randel, W. J., D. J. Seidel, and L. L. Pan, 2007: Observational characteristics of double tropopauses. *Journal of Geophysical Research: Atmospheres (1984-2012)*, **112**.

Rao, T. N., J. Arvelius, and S. Kirkwood, 2008: Climatology of tropopause folds over a european arctic station (esrange). *Journal of Geophysical Research: Atmospheres (1984-2012)*, **113**.

Reed, R. J., 1955: A study of a characteristic tpye of upper-level frontogenesis. *Journal of Meteorology*, **12**, 226–237.

Reed, R. J. and E. F. Danielsen, 1959: Fronts in the vicinity of the tropopause. *Archiv für Meteorologie, Geophysik und Bioklimatologie, Serie A*, **11**, 1–17.

Reynolds, R. W., N. A. Rayner, T. M. Smith, D. C. Stokes, and W. Wang, 2002: An improved in situ and satellite sst analysis for climate. *Journal of climate*, **15**, 1609–1625.

Rossby, C. G., 1940: Planetary flow patterns in the atmosphere. *Quarterly Journal of the Royal Meteorological Society*, **66**, 68–87.

Santer, B. D., M. F. Wehner, T. Wigley, R. Sausen, G. Meehl, K. Taylor, C. Ammann, J. Arblaster, W. Washington, J. Boyle, et al., 2003: Contributions of anthropogenic and natural forcing to recent tropopause height changes. *Science*, **301**, 479–483.

Schmidt, T., G. Beyerle, S. Heise, J. Wickert, and M. Rothacher, 2006: A climatology of multiple tropopauses derived from gps radio occultations with champ and sac-c. *Geophysical research letters*, **33**, L04808.

Seidel, D. J., R. J. Ross, J. K. Angell, and G. C. Reid, 2001: Climatological characteristics of the tropical tropopause as revealed by radiosondes. *Journal of Geophysical Research: Atmospheres (1984–2012)*, **106**, 7857–7878.

Shapiro, M., 1976: The role of turbulent heat flux in the generation of potential vorticity in the vicinity of upper-level jet stream systems. *Monthly Weather Review*, **104**, 892–906.

— 1978: Further evidence of the mesoscale and turbulent structure of upper level jet stream-frontal zone systems. *Monthly Weather Review*, **106**, 1100–1111.

— 1980: Turbulent mixing within tropopause folds as a mechanism for the exchange of chemical constituents between the stratosphere and troposphere. *Journal of the Atmospheric Sciences*, **37**, 994–1004.

Shapiro, M. A. and D. A. Keyser, 1990: *Fronts, jet streams, and the tropopause*. US Department of Commerce, National Oceanic and Atmospheric Administration, Environmental Research Laboratories, Wave Propagation Laboratory.

Silva, V. and V. E. Kousky, 2012: The south american monsoon system: Climatology and variability. *Modern Climatology*, D. S.-Y. Wang, ed., InTech, 123–152.

Škerlak, B., M. Sprenger, and H. Wernli, 2014: A global climatology of stratosphere–troposphere exchange using the era-interim data set from 1979 to 2011. *Atmospheric Chemistry and Physics*, **14**, 913–937.

Speth, P., S. Blonsky, and H. Kunz, 1996: Bestimmung des anthropogenen und natürlichen anteils am ozon im mitteleuropäischen raum aus meteorologischer sicht. abschlussbericht und wissenschaftliche ergebnisse. Technical Report 07EU777A0, BMFT Forschungsvorhaben.

Sprenger, M., M. C. Maspoli, and H. Wernli, 2003: Tropopause folds and cross-tropopause exchange: A global investigation based upon ecmwf analyses for the time period march 2000 to february 2001. *Journal of geophysical research*, **108**, 8518.

Sprenger, M. and H. Wernli, 2003: A northern hemispheric climatology of cross-tropopause exchange for the era15 time period (1979-1993). *Journal of geophysical research*, **108**, 8521.

Stohl, A., P. Bonasoni, P. Cristofanelli, W. Collins, J. Feichter, A. Frank, C. Forster, E. Gerasopoulos, H. Gäggeler, P. James, et al., 2003: Stratosphere-troposphere exchange: A review, and what we have learned from staccato. *Journal of Geophysical Research: Atmospheres (1984–2012)*, **108**.

Thorpe, A., 1985: Diagnosis of balanced vortex structure using potential vorticity. *Journal of the atmospheric sciences*, **42**, 397–406.

— 1997: Attribution and its application to mesoscale structure associated with tropopause folds. *Quarterly Journal of the Royal Meteorological Society*, **123**, 2377–2399.

Thorpe, A. J., 1986: Synoptic scale disturbances with circular symmetry. *Monthly weather review*, **114**, 1384–1389.

Uccellini, L. W., 1990: Processes contributing to the rapid development of extratropical cyclones. *Extratropical Cyclones: The Erik Palmén Memorial Volume*, 81–105.

Van Haver, P., D. De Muer, M. Beekmann, and C. Mancier, 1996: Climatology of tropopause folds at midlatitudes. *Geophysical research letters*, **23**, 1033–1036.

Vaughan, G., J. Price, and A. Howells, 1994: Transport into the troposphere in a tropopause fold. *Quarterly Journal of the Royal Meteorological Society*, **120**, 1085–1103.

Wang, S. and L. Polvani, 2011: Double tropopause formation in idealized baroclinic life cycles: The key role of an initial tropopause inversion layer. *Journal of Geophysical Research: Atmospheres (1984-2012)*, **116**.

Warner, T. T., R. A. Peterson, and R. E. Treadon, 1997: A tutorial on lateral boundary conditions as a basic and potentially serious limitation to regional numerical weather prediction. *Bulletin of the American Meteorological Society*, **78**, 2599–2617.

Wernli, H. and M. Bourqui, 2002: A lagrangian "1-year climatology" of (deep) cross-tropopause exchange in the extratropical northern hemisphere. *Journal of geophysical research*, **107**, 4021.

Wimmers, A. and J. Moody, 2004a: Tropopause folding at satellite-observed spatial gradients: 1. Verification of an empirical relationship. *Journal of Geophysical Research: Atmospheres (1984-2012)*, **109**.

— 2004b: Tropopause folding at satellite-observed spatial gradients: 2. Development of an empirical model. *Journal of Geophysical Research: Atmospheres (1984-2012)*, **109**.

WMO, 1957: Meteorology - A three-dimensional science. *WMO Bull.*, **6**, 134–138.

— 1986: Atmospheric ozone. *WMO Report*, **16**.

Wu, G. and Y. Zhang, 1998: Tibetan plateau forcing and the timing of the monsoon onset over south asia and the south china sea. *Monthly Weather Review*, **126**, 913–927.

Zahn, A., C. Brenninkmeijer, and P. Van Velthoven, 2004: Passenger aircraft project CARIBIC 1997–2002, Part I: The extratropical chemical tropopause. *Atmospheric Chemistry and Physics Discussions*, **4**, 1091–1117.

List of Figures

List of Tables